Electronic Excitations in Semiconductors and Insulators Using the Sternheimer-GW Method

Henry Lambert

Wolfson College, University of Oxford

A thesis submitted for the Degree of
Doctor of Philosophy in Materials

Trinity Term 2014

Contents

Contents i

Abstract v

1 Introduction 1
1 Motivation . . . 1
2 The many-body wavefunction . . . 1
3 Materials and methods . . . 4
4 A theory for excited states . . . 5
5 Structure of the thesis . . . 7

2 Density Functional Theory and the *GW* approximation 11
1 Density Functional Theory . . . 12
1.1 Hohenberg-Kohn theorem . . . 12
1.2 Kohn-Sham theory . . . 13
1.3 The Local Density Approximation . . . 15
2 The Green's function . . . 17
2.1 Definition of the Green's function . . . 17
2.2 Analytic structure of the Green's function . . . 19
3 Green's function methods . . . 22
3.1 Equation of motion . . . 22
3.2 Functional derivative of the Green's function . . . 24
4 Hedin's equations . . . 27
4.1 Dielectric function . . . 27
4.2 Hedin's equations . . . 29
5 Conclusion . . . 30

3 Practical Calculations 33
1 Single iteration of Hedin's equations: G_0W_0 . . . 33
1.1 Calculating the polarizability . . . 34
1.2 The Screened Coulomb interaction . . . 35
1.3 Plasmon-pole model . . . 36
1.4 The Green's function and the self-energy . . . 37
2 Planewaves and pseudopotentials . . . 38
2.1 Planewave basis set . . . 38
2.2 Pseudopotentials . . . 40
2.3 Kohn-Sham equation with planewaves . . . 42
2.4 Truncation of the Coulomb interaction . . . 43
3 G_0W_0 self-energy and corrections to LDA eigenvalues . . . 45
4 The Spectral function . . . 46
4.1 The *GW* spectral function . . . 46

4.2 Contact with experiment 48
4.3 Bardyszewski-Hedin theory of photoemission 48
5 Conclusion 50

4 Alternative Approaches to Performing *GW* Calculations 51
1 *GW* with optimal polarizability basis and Lanczos recursion . . . 52
2 The *GW* with Spectral Decomposition Method 55
3 Effective Energy Technique 58
4 Self-Consistency and the *GW* approximation 58
5 Scaling considerations 60
6 Conclusion 61

5 Theory and Implementation of the Sternheimer-*GW* Approach 63
1 The Sternheimer equation 63
2 Real-space formulation 64
2.1 Screened Coulomb interaction 65
2.2 Green's function 70
3 Reciprocal-space formulation 72
3.1 Screened Coulomb interaction 72
3.2 Green's function 74
3.3 The self-energy 74
4 Crystal symmetry 75
5 Frequency dependence 79
5.1 Multishift solver 80
5.2 Analytic continuation 83
6 Conclusion 85

6 Tests and Validation of the Sternheimer-*GW* Method 87
1 Polarizability calculations 87
2 Quasiparticle corrections 90
2.1 Quasiparticle eigenvalues 90
2.2 Convergence of quasiparticle eigenvalues 94
3 Quasiparticle spectral function 97
3.1 Plasmaronic band structure 99
4 Scaling performance 101
5 Spatial structure of the self-energy 104
6 Approximate Vertex Correction: RPA+V^{xc} 105
7 Conclusion 106

7 Quasiparticle Excitations in MoS_2 107
1 Structure of MoS_2 108
2 MoS_2 ground state electronic structure 109
2.1 LDA calculations 110
3 Dielectric properties of MoS_2 112
4 Quasiparticle eigenvalues 116
5 Spectral Functions 121

6 Conclusion 124

8 Conclusion **127**
1 Summary of work to date 127
2 Future work 128

A Functional Derivatives **131**

B Rational Interpolation **133**

C Algorithms **135**
1 cBiCG 135
2 cBiCG Multishift 135
2.1 Solution of seed system 136
2.2 Shifted systems 136

Bibliography **139**

Acknowledgements **I**

Papers and Presentations **II**

Abstract

Electronic Excitations in Semiconductors and Insulators Using the Sternheimer-*GW* Method

Henry Lambert, Wolfson College

A thesis submitted for the Degree of
Doctor of Philosophy in Materials Science, Trinity Term 2014

In this thesis we describe the extension and implementation of the Sternheimer-*GW* method to a first-principles pseudopotential framework based on a planewaves basis. The Sternheimer-GW method consists of calculating the *GW* self-energy operator without resorting to the standard expansion over unoccupied Kohn-Sham electronic states. The Green's function is calculated by solving linear systems for frequencies along the real axis. The screened Coulomb interaction is calculated for frequencies along the imaginary axis using the Sternheimer equation, and analytically continued to the real axis. We exploit novel techniques for generating the frequency dependence of these operators, and discuss the implementation and efficiency of the methodology.

We benchmark our implementation by performing quasiparticle calculations on common insulators and semiconductors, including Si, diamond, LiCl, and SiC. Our calculated quasiparticle energies are in good agreement with the results of fully-converged calculations based on the standard sum-over-states approach and experimental data. We exploit the methodology to calculate the spectral functions for silicon and diamond and discuss quasiparticle lifetimes and plasmaronic features in these materials.

We also exploit the methodology to perform quasiparticle calculations on the 2-dimensional transition metal dichalcogenide system molybdenum disulfide (MoS_2). We compare the quasiparticle properties for bulk and monolayer MoS_2, and identify significant corrections at the *GW* level to the LDA bandstructure of these materials. We also discuss changes in the frequency dependence of the electronic screening in the bulk and monolayer systems and relate these changes to the quasiparticle lifetimes and spectral functions in the two limits.

1 Introduction

1 Motivation

It is desirable to have a physical theory which describes the processes occurring in nature and accounts for some of the diversity of natural phenomenon we observe. Given the vast range of experience we must seek to limit the scope of our inquiry. In this thesis we restrict our interest to the fundamental electronic properties of materials.

By the electronic structure and properties of a material we mean the arrangement of electrons and nuclei in a material, their mutual interactions, and the resulting physical observables. We study this subject with the object of understanding the simplest, most direct route, to obtaining an accurate description of a materials electronic structure. The extent to which we can consider ourselves successful in this task is determined by comparison to experiment, our ability to meaningfully predict material properties, and the simplicity and practical utility of our approach.

In this introduction we provide a qualitative picture of the physics that we will be considering, the systems and processes in nature to which they apply, and the techniques that we will be developing to study these aspects. We also give an overview of the structure of this thesis.

2 The many-body wavefunction

In classical physics we are able to specify the positions and momenta of a collection of particles with simultaneous and arbitrary precision. Given an exact specification of position and momenta, classical mechanics allows us to describe the subsequent evolution in time of this collection of particles according to certain equations of motion. This program was successfully pursued into the beginning

of the 20th century [1].

When it comes to describing the motion of electrons and nuclei classical mechanics breaks down. The appropriate description of atomic phenomenon is given by quantum mechanics [1]. In quantum mechanics Heisenberg's uncertainty principle means that the exact, simultaneous, specification of the momentum and position of a particle, or collection of particles, is not possible: the position and momenta are conjugate variables. The conjugate nature of these variables means that the physical system is fully specified with reference to either the momentum or the position of the particles alone. The evolution of the many particle system is described by wave mechanics and the many particle system is represented by a wave function.

The central equation describing the evolution of the wave function is the Schrödinger equation [2]:

$$\hat{H}\Psi(\mathbf{R}_j, \mathbf{r}_i, t) = i\frac{\partial}{\partial t}\Psi(\mathbf{R}_j, \mathbf{r}_i, t). \tag{1.1}$$

Where $\hat{H}$ is the Hamiltonian operator describing the energy of the interactions, and $\Psi(\mathbf{R}_j, \mathbf{r}_i, t)$ is the wave function of the interacting system. The variables of the wavefunction are: the nuclear coordinates $\mathbf{R}_j$, the electronic coordinates $\mathbf{r}_i$, and the time t. Eq. 1.1 describes the non-relativistic evolution of the wavefunction with time.

A natural place to begin our study of the properties of materials is by specifying all the possible interactions that appear in the Hamiltonian [2]:

$$H = -\frac{1}{2}\sum_i \nabla_i^2 - \sum_j \frac{1}{2m_j}\nabla_j^2 - \sum_{i,j}\frac{Z_j}{|\mathbf{r}_i - \mathbf{R}_j|} + \frac{1}{2}\sum_{i,k\neq i}\frac{1}{|\mathbf{r}_i - \mathbf{r}_k|} + \frac{1}{2}\sum_{j,k\neq j}\frac{Z_j Z_k}{|\mathbf{R}_j - \mathbf{R}_k|}. \tag{1.2}$$

Eq. 1.2 is the Hamiltonian for a system of electrons and nuclei in Hartree atomic units. The first two terms describe the kinetic energy of the electrons and nuclei respectively. Subsequent terms describe the electron-electron, electron-nuclear,

and nuclear-nuclear, Coulombic interaction. Analytic solutions to Eq. 1.1 for system involving more than one nucleus and one electron do not exist and Eq. 1.1 must be solved numerically.

The difficulty of producing numerical solutions is a byproduct of the many particle nature of the problem. This can be readily appreciated. If one considers a small piece of solid crystal the number of electrons and nuclei would be on the order of 10^{23}. If we exploit the crystalline nature of the sample under consideration we could map the problem down to the fundamental unit cell of the crystal and describe only the electrons and nuclei present in that region. Further approximations might allow us to decouple nuclear and electronic motion, and the interaction of the valence electrons with the electrons tightly bound to the nuclei in the material. Even after all these approximation we are still left with a demanding problem.

For a definite example we might consider a diamond crystal. With two carbon atoms in the crystal unit cell and four electrons in the valence of each carbon atom, the wavefunction is a function of eight spatial coordinates and a time coordinate. For definiteness we might seek to describe our crystal wavefunction using a $10 \times 10 \times 10$ real space grid. Electronic storage of Ψ would now require 116 Gigabytes. This memory requirement is just to store the wavefunction: the operations involved in applying the Hamiltonian and solving Eq. 1.1 make investigations based on the wavefunction numerically intensive. Though by no means impossible using modern computers the numerical enterprise remains formidable. There are other objections to approaches based on the direct manipulation of the many-body wavefunction. Physical intuition for such a high dimensional quantity is severely restricted, and the potential to apply the methods to larger physical systems are negatively impacted by the scaling of wave functions methods.

These difficulties motivate an alternative approach with more favourable scaling properties and which appeal to physical intuition. In this thesis we employ

Density Functional Theory (DFT) to side step the difficulties associated with methods based directly on the many-body wavefunction. DFT is a Hamiltonian based, mean field theory, which allows us to circumvent the difficulties of working directly with the many-body wavefunction, and provides scope for applying physical intuition. The theory will be introduced and discussed in Chapter 2. Using DFT we can obtain a description of the ground state electronic structure of a material.

3 Materials and methods

Throughout this thesis we will have occasion to compare the results of our calculations to a number of experimentally measured electronic properties in a variety of materials. Fig. 1.1 illustrates one of the most relevant experimental probes for connecting the theory described later in this thesis and experiment. Fig. 1.1 schematically depicts the essential process behind a photoemission experiment. A light source with a well characterized beam of photons strikes the surface of a material. An electron can be ejected from the material via the photoelectric effect. The electron can then propagate to a detector which measures its energy and momentum. Knowledge of the energy and momentum of the original photon and the measured electron can be used to determine the original state of the electron in the material. Further detail about the use of photoelectron spectroscopy can be found in Ref. [3].

The entire range of energy and momentum space can be probed to obtain information about the electronic states in a material. These can then be compared to theoretical calculations of the electronic structure. The interpretation of photoemission experiments and their connection to theory will be discussed in Chapter. 3.

The techniques developed in this thesis will largely be used to determine the theoretical electronic structure for different materials. These will include small organic molecules, semiconductors, insulating systems. Where possible we will

compare with experimental photoemission data.

4 A theory for excited states

As was mentioned, the many-body wave function based on the full interacting Hamiltonian, Eq. 1.2, is an unwieldy object. Furthermore, its connection to the simple experimental picture in Fig. 1.1, of ejecting individual electrons from a material and inferring their initial energy and momentum, is unclear.

DFT provides a means of directly obtaining information about the electronic structure of materials in a practical manner. It allows us to map the many-body wavefunction to an equivalent problem involving non-interacting electrons, and allows us to perform calculations on realistic material systems with many

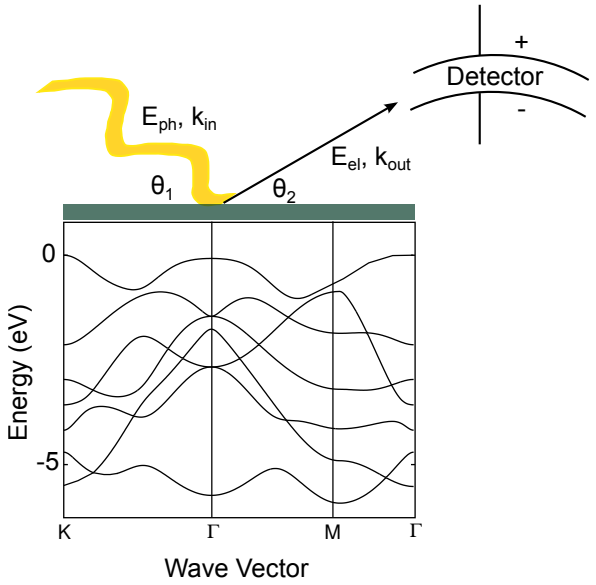


Figure 1.1: One of the most direct probes of the electronic structure of a material comes from photoemission spectroscopy. An incoming photon with energy, E_{ph}, and wave vector, $\mathbf{k}_{in}$, strikes the surface of a material. This photon can eject an electron with energy, E_{el}, and wave vector $\mathbf{k}_{out}$ from a particular electronic state in a material. This ejected electron can be captured in a detector. Knowledge of the momentum and energy of the scattering beam, the conservation of momentum parallel to the surface and the total energy of the captured electron allows one to infer the energy and wave vector of the initial electronic state. This data can then be compared to a theoretical model of the electronic structure of the material.

electrons.

While DFT provides a starting point for obtaining a description of the electronic properties of materials we require a further level of theory to describe more advanced processes. For instance the physical process illustrated in Fig. 1.1 requires a description of excited state properties.

To accurately describe these excitation processes we make use of Green's function theory and what is known as the *GW* approximation. This will be discussed in Chapter 2. We can here describe the qualitative change we make when moving from a DFT description of the ground state electronic properties to the Green's function-based description. By treating the Green's function of the system directly we can formally define a shift from a *single particle* picture to a *quasiparticle* picture, and uncover additional information about collective excitations in an interacting electronic system.

The physics of this change in viewpoint comes from the many-body nature of the problem. An experimental probe of a materials electronic structure involves either the addition or removal of an electron to or from the system. In the single particle picture these processes would correspond to a single definite energy. In a many-body system their will be a characteristic response time to an addition or removal process before the electron or hole decays in to a lower energy state. In addition the impact of a photon or electron could set up a collective excitation. These changes are illustrated qualitatively in Fig. 1.2. It is the features of Fig. 1.2 that we will try to calculate in the course of this work: accurate energy levels for electrons in a material, the time an electron might spend in a particular energetic state, and types of collective excitations involving many electrons which may be present.

The direct and rapid execution of *GW* calculations, which give us access to all these quasi-particle features, is the main focus of this thesis. We assess and develop techniques which allow for the direct construction of the key quantities

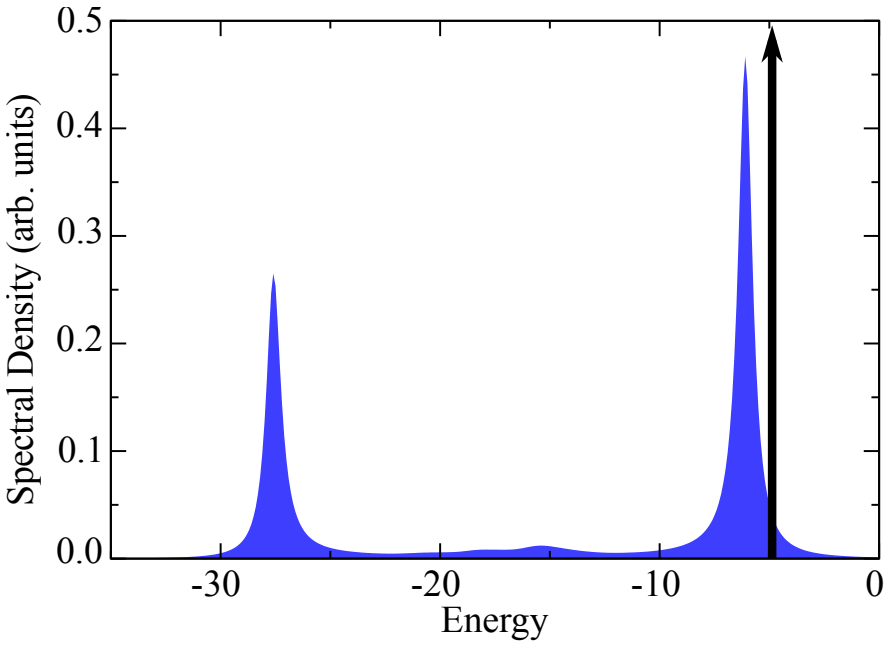


Figure 1.2: The quasiparticle picture contains a great deal of physical information. We move from the single particle description, black arrow, to the quasiparticle picture, shaded blue region. The energy of the QP excitation is renormalized by its interaction with the other electrons in the system. The width of the peak can be related to the lifetime of the excitation. Finally new features are observed in the form of satellite structures corresponding to collective excitations in the material in the lower energy range.

required to perform *GW* calculations. We term the overall methodology presented here for performing *GW* calculations the Sternheimer-*GW* approach. The specifics of the Sternheimer-*GW* approach and how it relates to contemporary work are discussed in Chapters 4-6.

5 Structure of the thesis

In Chapter 2 we discuss the application of density functional theory to the electron many-body problem. We also introduce the Green's function theory and present the full derivation of Hedin's equations and the *GW* method.

In Chapter 3 we discuss the practicalities of performing DFT and *GW* calculations. These practicalities include a discussion of the planewaves pseudopotential formalism and the numerical construction of the key operators required to

perform a standard *GW* calculation. While discussing these issues we highlight some of the numerical difficulties which prevent rapid *GW* calculations from being performed using standard approaches, and how these are alleviated by the work presented in this thesis. We also formally introduce the quasiparticle picture and spectral function which we have discussed on a qualitative level in the present chapter.

In Chapter 4 we present a literature survey of contemporary work in this active field. We highlight the similarities and differences with other approaches that are being developed to make *GW* calculations more efficient, and to extend the applicability of the method.

In Chapter 5 we discuss the Sternheimer approach to performing *GW* calculations. We provide proofs justifying the methods used to construct the relevant quantities in a *GW* calculation. We discuss the numerical details of the approach and the novel application of recently developed approaches for solving linear systems of equations. We discuss the use of symmetry relations which allow us to perform calculations in crystalline environments efficiently. We also discuss certain computational considerations like parallelism and the intrinsic scaling of the method.

In Chapter 6 we discuss the tests and validation of the Sternheimer-*GW* method. We benchmark the method against previous calculations for small molecules, semiconductors and insulators. We discuss in detail the numerical convergence of calculations performed using standard approaches and the present Sternheimer approach. We also present the full spectral functions for silicon and diamond calculated using the present methodology, and highlight features which merit further investigation.

In Chapter 7 we apply the methodology to MoS_2 , a material with an intrinsically 2-dimensional nature. We exploit the present methodology to demonstrate the difficulties of performing fully converged calculations. We also exploit the

methodology to demonstrate the differences in electronic screening in the bulk and the monolayer conformations of MoS_2 , and the different quasiparticle properties observed in the two regimes.

Finally, in Chapter 8, we summarize our results to date and discuss potential future applications of the Sternheimer-*GW* methodology.

2 Density Functional Theory and the GW approximation

In this chapter we discuss the theory underlying the fundamental techniques used in this thesis, specifically the use of Density Functional Theory (DFT) and the GW approximation to obtain a quantitative *ab initio* description of electronic excitations.

DFT has its foundations in the papers of Hohenberg and Kohn [4], and Kohn and Sham, [5]. DFT provides a means for obtaining the ground-state energy of an interacting system of electrons, and provides a formal route to the solution of the many electron Schrödinger equation. In this chapter we discuss the theory of obtaining ground-state properties for an interacting electronic system using DFT, and some of the fundamental limitations of the method. In particular we highlight the success of DFT for treating structural properties and its limited success for describing the excited state properties of an electronic system [2].

Since standard DFT was designed specifically to obtain the ground-state energy of an interacting system of electrons it is not expected to yield information about excited state properties. To extend the theory to treat excited states we make use of Hedin's GW approximation [6]. The GW formalism takes its name from the the Green's function, denoted G, and the screened Coulomb interaction, W. Hedin's GW approximation allows us to extend the standard DFT formalism to obtain information about the excited state properties of materials. We begin by discussing the analytic properties of the interacting and non-interacting Green's function and how the Green's function encodes information about the many-body excited electronic states. To derive Hedin's equations, from which the GW approximation follows, we examine the equation of motion for the Green's

function and construct a closed loop of equations which contain all the effects of the electron-electron interaction.

1 Density Functional Theory

1.1 Hohenberg-Kohn theorem

In Ref. [4] a proof is presented that the ground-state energy of a system of interacting electrons in a fixed external potential is a unique functional of the electronic density $n(\mathbf{r})$, with $\mathbf{r}$ being the position vector. According to Hohenberg and Kohn the ground-state energy as a functional of the density can be written:

$$E[n] = \int v(\mathbf{r})n(\mathbf{r})d\mathbf{r} + \frac{1}{2}\int \frac{n(\mathbf{r})n(\mathbf{r}')}{|\mathbf{r}-\mathbf{r}'|}d\mathbf{r}d\mathbf{r}' + G[n]. \tag{2.1}$$

Eq. 2.1 divides the total energy functional $E[n]$ into different contributions. $\int v(\mathbf{r})n(\mathbf{r})d\mathbf{r}$ is the energy contribution from the external potential $v(\mathbf{r})$. The term $\frac{1}{2}\int \frac{n(\mathbf{r})n(\mathbf{r}')}{|\mathbf{r}-\mathbf{r}'|}d\mathbf{r}d\mathbf{r}'$ is the Hartree energy, i.e. the classical Coulomb repulsion energy associated with the electron density. $G[n]$ is a universal functional of the density accounting for all the remaining electron-electron interaction effects. If an explicit expression for $G[n]$ is provided, then Eq. 2.1 can be minimized with respect to variations of the density δn.

Hohenberg and Kohn begin from a Hamiltonian for the interacting electronic system of the form:

$$\hat{H} = \hat{H}_0 + \hat{H}_{\text{int}} + v(\mathbf{r}), \tag{2.2}$$

where $\hat{H}_0$ is the kinetic energy, $\hat{H}_{\text{int}}$ is the electron-electron Coulomb repulsion and $v(\mathbf{r})$ is a local external potential. Given the particular Hamiltonian $\hat{H}$, and its associated ground-state electronic wave function Ψ, the ground-state energy of the system is:

$$E = \langle\Psi|\hat{H}|\Psi\rangle. \tag{2.3}$$

The proof of the Hohenberg-Kohn Theorem is carried out using a *reductio ad*

absurdum argument. Initially it is assumed that two external potentials, which differ by more than a constant, can give rise to the same ground-state electron densities. The two potentials give rise to two different Hamiltonians, with different ground-state wave functions. It can then be demonstrated that this gives rise to a contradiction in the ground-state energies for the two different external potentials. The only way to resolve the contradiction is to accept that the external potential is uniquely determined by the ground-state density to within a constant. The corollary of this is also true and the Hamiltonian is uniquely determined as a functional of the ground-state density [2]. The original proof is only valid for non-degenerate grounds states the use of constrained searches generalizes the proof to arbitrary ground-states [7–9].

While the Hohenberg-Kohn theorem provides a formal route to obtaining the ground-state energy of an interacting system, the exchange correlation functional $G[n]$ remains unspecified. Practical solutions require explicit approximations to the functional which we will discuss in the subsequent sections.

1.2 Kohn-Sham theory

Building on the work of Hohenberg and Kohn in Ref. [4], Kohn and Sham reformulated the problem of finding the ground-state density of a system of interacting electrons by considering an auxiliary set of non-interacting electrons in Ref. [5].

In the approach of Ref. [5] an electronic density is generated from a fictitious set of non-interacting electronic states:

$$n(\mathbf{r}) = 2\sum_{i=1}^{\mathrm{n_{occ}}} \psi_i^*(\mathbf{r})\psi_i(\mathbf{r}). \tag{2.4}$$

Where $\mathrm{n_{occ}}$ is the number of occupied electronic states in the system and the factor of 2 accounts for spin degeneracy. Eq. 2.4 implies that the many-electron wave function is a Slater determinant. The Hamiltonian for the non-interacting electronic states is chosen such that it is composed of the kinetic energy operator

for non-interacting electrons, and a potential that is purely local:

$$\hat{H}^{\mathrm{ks}} = -\frac{1}{2}\nabla^2 + \sum_j V^{\mathrm{e-n}}(\mathbf{r} - \mathbf{R}_j) + V^{\mathrm{H}}(\mathbf{r}) + V^{\mathrm{xc}}(\mathbf{r}). \tag{2.5}$$

Here $V^{\mathrm{e-n}}(\mathbf{r} - \mathbf{R}_j)$ is the Coulomb potential felt by an electron at point $\mathbf{r}$ from a nucleus at point $\mathbf{R}_j$. The term $V^{\mathrm{H}}(\mathbf{r})$ is the Hartree potential:

$$V^{\mathrm{H}}(\mathbf{r}) = \int \frac{n(\mathbf{r}')}{|\mathbf{r} - \mathbf{r}'|} d\mathbf{r}', \tag{2.6}$$

and gives rise to the third term on the right hand side of Eq. 2.1

The remaining term is the exchange and correlation potential V^{xc}. If an explicit functional dependence on $n(\mathbf{r})$ for V^{xc} is provided one can then seek an energy minimum for the fictitious non-interacting system by minimizing the variation in the total energy with respect to the density:

$$\frac{\delta E^{\mathrm{KS}}[n]}{\delta \psi_i^*} = 0, \tag{2.7}$$

and ensuring that the orthogonality constraints between the wavefunctions:

$$\langle \psi_i | \psi_j \rangle = \delta_{i,j}, \tag{2.8}$$

are satisfied. The Kohn-Sham Hamiltonian is determined by the electronic density $n(\mathbf{r})$; the electronic density is defined by the single-particle wavefunctions, $\psi_n(\mathbf{r})$ in Eq. 2.4; and, finally, the single particle wavefunction are defined by the solutions of the equation:

$$\hat{H}^{\mathrm{KS}} \psi_n(\mathbf{r}) = \epsilon_n \psi_n(\mathbf{r}). \tag{2.9}$$

The dependency of the Hamiltonian on the density means obtaining the Kohn-Sham wavefunctions and eigenvalues requires a self-consistent procedure. In or-

der to proceed some definite form for $V^{\rm xc}(\mathbf{r})$ is required. We discuss this in the next section.

1.3 The Local Density Approximation

The practical success of DFT is largely determined by one's ability to find an adequate approximation to the exchange and correlation functional. For many ground-state properties the Local Density Approximation (LDA) has proven to be very accurate. In this scheme the exchange and correlation energy is written:

$$E_{\rm xc}[n(\mathbf{r})] = \int \epsilon_{\rm xc}(\mathbf{r}) n(\mathbf{r}) d\mathbf{r}, \tag{2.10}$$

where $\epsilon_{\rm xc}$ is the energy per electron at point $\mathbf{r}$ depending only upon the density $n(\mathbf{r})$ in an homogeneous electron gas[2]. The exchange and correlation potential can be obtained from the exchange correlation energy via:

$$V^{\rm xc}(\mathbf{r}) = \frac{\delta E_{\rm xc}[n(\mathbf{r})]}{\delta n(\mathbf{r})}. \tag{2.11}$$

A number of parametrizations for the function $\epsilon_{xc}(\mathbf{r})$ exist. The first parameterizations of the correlation energy were based on polynomial fitting to Monte Carlo calculations of the correlation energy of the homogeneous electron gas performed in Ref. [10]. These parameterizations include Refs. [11–13].

Using the LDA means each term appearing in the Hamiltonian, Eq. 2.9, is local and Hermitian. In addition the exchange and correlation functional is easily calculated using the aforementioned parameterizations.

The success of the LDA has motivated the search for improvemed functionals which better account for the variation in the ground-state charge density or incorporate exact exchange contributions to the ground-state densities [14–17].

The generalization of the exchange and correlation operator beyond the LDA in order to allow for non-locality and the energy dependence of the exchange

and correlation potential is discussed in Refs. [18]. In this work Kohn and Sham rewrite Eq. 2.9 so that it mirrors the form of the quasiparticle equation presented in Refs. [6, 19]:

$$\left[-\frac{1}{2}\nabla^2 + V^{\text{ion}}(\mathbf{r}) + V^{\text{H}}(\mathbf{r})\right]\psi_n(\mathbf{r}) + \int \Sigma(\mathbf{r},\mathbf{r}';E_n)\psi_n(\mathbf{r}')d\mathbf{r}' = E_n\psi_n(\mathbf{r}). \quad (2.12)$$

Here the quantity $\Sigma(\mathbf{r},\mathbf{r}';\omega)$ is a non-local and energy dependent, operator which encodes all the electronic correlations present in the system. Calculating this quantity is a formidable challenge. We have introduced this quantity here because it will arise again in the discussion of the *GW* approximation, and provides a natural connection between DFT and the Green's functions methods. A formal connection between DFT and many body perturbation theory is provided in Ref. [20].

The Kohn-Sham theory provides a set of eigenvalues and eigenvectors for an auxiliary non-interacting electronic system. While it is tempting to use the unoccupied electronic states resulting from a Kohn-Sham DFT/LDA calculation to represent the conduction states of real materials, this leads to a number of problems.

As we have mentioned DFT at the LDA level is a theory built to describe the ground-state of an electronic system. An LDA bandstructure systematically underestimates the magnitude of the band gaps in real materials, resulting in quantitative and qualitative errors when it comes to describing the electronic excitations of a many electron system [2]. This is partly due to deficiencies inherent in the approximations to the exchange correlation potential, and to the inherent discontinuity upon the addition or removal of an electron present in the exact functional [21–23]. There are a number of possible approaches for extending the DFT formalism to access excited state properties. Hybrid functionals [24, 25] and Δ SCF methods [26, 27] go someway towards providing a formalism for accurately calculating excitation energies. However, in the case of hybrid

functionals, the choice of functional remains somewhat arbitrary, and for Δ SCF, the method is inapplicable in the case of bulk systems.

In addition the DFT formalism cannot account for dynamical effects, such as electron lifetimes. This failure requires the introduction of a more sophisticated approach for an accurate description of excited-state properties. In the remainder of this chapter we introduce the concepts required to treat excited states quantitatively using the *GW* approximation.

2 The Green's function

2.1 Definition of the Green's function

To begin the discussion of the *GW* approximation we introduce the Green's function. The Green's function is defined as:

$$G(\mathbf{r}, t, \mathbf{r}', t') = \langle N|\hat{T}\left[\hat{\psi}(\mathbf{r}, t)\hat{\psi}^{\dagger}(\mathbf{r}', t')\right]|N\rangle, \tag{2.13}$$

$\hat{T}$ is the time ordering operator ensuring events at time t occur after event t'. $\hat{\psi}^{\dagger}$ and $\hat{\psi}$ are the fermion creation and annihilation field operators:

$$\hat{\psi}(\mathbf{r}, t) = \sum_{n} \phi_n(\mathbf{r})c_n(t), \tag{2.14}$$

and

$$\hat{\psi}^{\dagger}(\mathbf{r}, t) = \sum_{n} \phi_n^{\star}(\mathbf{r})c_n^{\dagger}(t), \tag{2.15}$$

where $c_n^{\dagger}(t)$ and $c_n(t)$ are creation and annihilation operators, and $\phi_n(\mathbf{r})$ are the single particle wave functions, these could be Kohn-Sham wavefunctions. The ground-state wave functions can be obtained from a DFT calculation. Note the time dependence is included in the creation and annihilation operator rather than the wave function. $|N\rangle$ represents the electronic ground-state wave function for a system of N electrons.

The time ordering operator can be expanded for the single particle Green's function to provide:

$$\begin{aligned} G(\mathbf{r},t,\mathbf{r}',t') &= -i\Theta(t-t')\langle N|\hat{\psi}(\mathbf{r},t)\hat{\psi}^{\dagger}(\mathbf{r}',t')|N\rangle \\ &\quad +i\Theta(t'-t)\langle N|\hat{\psi}^{\dagger}(\mathbf{r}',t')\hat{\psi}(\mathbf{r},t)|N\rangle. \end{aligned} \tag{2.16}$$

In Eq. 2.16 Θ is the Heaviside step function. This ensures the causality of the Green's function. Physically we can interpret the role of the Heaviside step function as differentiating between two scenarios. When $(t-t') > 0$ the situation corresponds to the matrix element with the many-body wavefunction of an electron added to the system at the time t' in position $\mathbf{r}'$, and subsequently removed from the system at $\mathbf{r}, t$. For the case $(t'-t) > 0$ the Green's function describes the propagation of a hole.

To get a physical idea of what Eq. 2.16 represents we consider the following expression:

$$P(\mathbf{r},t,\mathbf{r}',t') = |\langle N|\hat{\psi}^{\dagger}(\mathbf{r}',t')\hat{\psi}(\mathbf{r},t)|N\rangle|^2 \qquad t' > t. \tag{2.17}$$

The above expression gives the probability amplitude that if we remove an electron from the position eigenstate $\mathbf{r}$ at time t it will propagate to the point $\mathbf{r}', t'$. Reversing the time arguments and field operators would correspond to the addition of an electron at point $\mathbf{r}'$ and removing it at point $\mathbf{r}$. If we let $\mathbf{r}' \to \mathbf{r}$, $t' \to t^+$ the Green's function reduces to the charge density of the system.[1]

In the case of a non-interacting single-particle Hamiltonian the time-dependence of the field operators can be expressed in terms of the single-particle eigenvalues, ϵ_n, as:

$$\hat{\psi}^{\dagger}(\mathbf{r},t) = \sum_n \phi_n^*(\mathbf{r})e^{-i\epsilon_n t}c_n^{\dagger}. \tag{2.18}$$

[1] $t^+ = t + \delta$, the current time plus an infinitesimal; this is to avoid confusion with the definition of the Heaviside step function

By replacing Eq. 2.18 inside Eq. 2.16 we find:

$$G(\mathbf{r},t,\mathbf{r}',t') = -i\Theta(t-t')\sum_{\epsilon_n>\epsilon_f}\phi_n(\mathbf{r})\phi_n^*(\mathbf{r}')e^{-i\epsilon_n(t-t')} + i\Theta(t'-t)\sum_{\epsilon_n<\epsilon_f}\phi_n(\mathbf{r})\phi_n^*(\mathbf{r}')e^{-i\epsilon_n(t-t')}. \quad (2.19)$$

Therefore in this case the Green's function separates naturally into two contributions, the first term in Eq. 2.19 coming from the non-interacting unoccupied electronic states of the system, the second term coming from the non-interacting occupied electronic states of the system (ϵ_f denotes the energy of the highest occupied state). A Fourier transform of Eq. 2.19 then yields the pole structure in Fig. 2.1 as will be discussed in the next section for the interacting Green's function.

2.2 Analytic structure of the Green's function

The Green's function has two particularly useful properties. The first is it effectively encodes all the response properties of the system to an external perturbation. The second is that the poles of the Green's function in the frequency domain, are equal to the energies required to excite the N electron system to a particular state of the $N+1$ or $N-1$ electron system. To demonstrate this it is necessary to Fourier transform the Green's from the time domain to the frequency domain. This can be accomplished by rewriting the field operators in the Heisenberg representation:

$$\hat{\psi}^\dagger(\mathbf{r},t) = e^{i\hat{H}t}\hat{\psi}^\dagger(\mathbf{r})e^{-i\hat{H}t}. \quad (2.20)$$

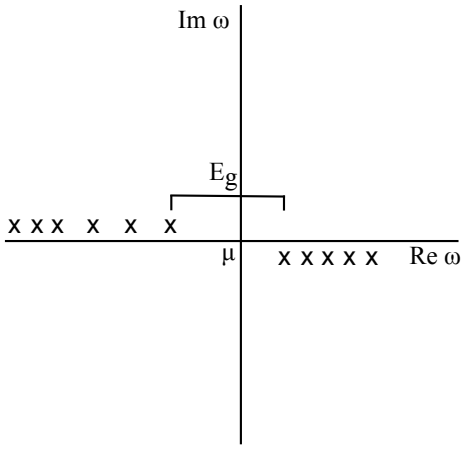


Figure 2.1: Pole structure of the Green's function. The occupied electronic states are slightly above the real frequency axis and below the chemical potential μ, the unoccupied states are located above the Fermi level and slightly below the real axis. The poles of the Green's function correspond to the addition/removal energies in the system. This example is for a system with a discrete series of excitation and a gap between occupied and unoccupied states of E_g.

We then introduce a complete set of states which describe all the possible intermediate excitations of the system to N' particles and their s excited states, $|N', s\rangle$:

$$\sum_s |N', s\rangle\langle N', s| = \hat{I}, \tag{2.21}$$

where $\hat{I}$ is the identity matrix. We also note that:

$$H|N, s\rangle = E_N^s|N, s\rangle. \tag{2.22}$$

If one inserts Eqs. 2.20 and 2.21 into Eq. 2.16 it is possible to write the Green's function in the time domain as:

$$\begin{aligned} G(\mathbf{r}, t, \mathbf{r}', t') = & \sum_s -i\Theta(t-t')e^{i(E_N^0 - E_{N'}^s)(t-t')}\langle N|\hat{\psi}(\mathbf{r})|N', s\rangle\langle N', s|\hat{\psi}^\dagger(\mathbf{r}')|N\rangle \\ + & \sum_s i\Theta(t'-t)e^{-i(E_N^0 - E_{N'}^s)(t-t')}\langle N|\hat{\psi}^\dagger(\mathbf{r}')|N', s\rangle\langle N', s|\hat{\psi}(\mathbf{r})|N\rangle. \end{aligned} \tag{2.23}$$

Now Eq. 2.23 gives the Green's function in the time domain and the arguments depend only on differences in time $t-t'$. By introducing the time variable $\tau = t-t'$ it is straightforward to define a Fourier transform:

$$G(\mathbf{r},\mathbf{r}';\omega) = \frac{1}{2\pi}\int_{-\infty}^{\infty} G(\mathbf{r},\mathbf{r},\tau)e^{i\omega\tau}d\tau, \tag{2.24}$$

and represent the Green's function in the frequency domain:

$$\begin{aligned} G(\mathbf{r},\mathbf{r}';\omega) &= \sum_s \frac{\langle N|\hat{\psi}(\mathbf{r})|N',s\rangle\langle N',s|\hat{\psi}^\dagger(\mathbf{r}')|N\rangle}{\omega-(E^s_{N'}-E^0_N)+i\delta} \\ &- \sum_s \frac{\langle N|\hat{\psi}^\dagger(\mathbf{r}')|N',s\rangle\langle N',s|\hat{\psi}(\mathbf{r})|N\rangle}{\omega+(E^s_{N'}-E^0_N)-i\delta}. \end{aligned} \tag{2.25}$$

The infinitesimal factors of $i\delta$ ensure that the Fourier transform converges at infinite time arguments. The presence of the field operators implies that the only non-zero contributions to Eq. 2.25 are between the ground and excited states of the $N' = N+1$ and the $N' = N-1$ systems. Therefore it is convenient to make the follow substitution [28]:

$$(E^s_{N+1} - E^0_N) = \epsilon^s_{N+1}, \tag{2.26}$$

with a similar expression for the $N-1$ system. The variable $\epsilon^s_{N\pm1}$ is the energy difference of an excited state in the $N\pm1$ many body system and the ground state of the $N\pm1$ system. This leads us to:

$$\begin{aligned} G(\mathbf{r},\mathbf{r}';\omega) = &\sum_s \frac{\langle N|\hat{\psi}(\mathbf{r})|N+1,s\rangle\langle N+1,s|\hat{\psi}^\dagger(\mathbf{r}')|N\rangle}{\omega-\epsilon^s_{N+1}+i\delta} \\ &-\sum_s \frac{\langle N|\hat{\psi}^\dagger(\mathbf{r}')|N-1,s\rangle\langle N-1,s|\hat{\psi}(\mathbf{r})|N\rangle}{\omega+\epsilon^s_{N-1}-i\delta}. \end{aligned} \tag{2.27}$$

The poles of Eq. 2.27 are represented schematically in Fig. 2.1 and correspond to the energies of the excitations from N to $N\pm1$ electrons in an interacting many body system. Having discussed the pole structure of the Green's function

we now proceed to define the equation of motion.

3 Green's function methods

Lars Hedin first developed the *GW* approximation with his publication "New Method for Calculating the One-Particle Green's Function with Application to the Electron-Gas Problem." [6]. In this work Hedin developed a self-consistent system of equations for including all the interaction effects in a many electron system. Hedin describes the connection between his work and the development of Green's functions methods by Schwinger in Ref. [19] working in the field of quantum electrodynamics. An early review of the applications of Green's function methods and Feynman diagrams to the many electron problem was given in Ref. [29]. The procedure has been extensively studied in the intervening thirty years and Refs. [30–32] provide a review of the contemporary state of the field.

3.1 Equation of motion

To derive the equation of motion for the Green's function we need the time derivative of Eq. 2.16. This derivative in turn requires working out the time dependence of the field operators appearing in Eq. 2.16:

$$\frac{\partial\hat{\psi}(\mathbf{r},t)}{\partial t} = i[\hat{H},\hat{\psi}(\mathbf{r},t)]. \tag{2.28}$$

The time dependence of the field operator is determined by the commutator between the Hamiltonian and the field operator. The general Hamiltonian we will consider can be separated into two parts:

$$\hat{H} = \hat{H}_0 + v(\mathbf{r},\mathbf{r}')\delta(t-t'), \tag{2.29}$$

where the $\hat{H}_0$ term describes the kinetic energy of the electron and the interaction of the electron with an ionic lattice. The $v(\mathbf{r},\mathbf{r}')\delta(t-t')$ term represents the inter-electron Coulomb repulsion. We differentiate Eq. 2.16 with respect to time to

arrive at the following result:

$$\left[i\frac{\partial}{\partial t} - \hat{H}_0\right] G(\mathbf{r},\mathbf{r}',t,t') +$$
$$i\int v(\mathbf{r},\mathbf{r}'')\langle N|T[\hat{\psi}^\dagger(\mathbf{r}'',t)\hat{\psi}(\mathbf{r}'',t)\hat{\psi}(\mathbf{r},t)\hat{\psi}^\dagger(\mathbf{r}',t')]|N\rangle d\mathbf{r}'' = \quad \delta(\mathbf{r}-\mathbf{r}')\delta(t-t'). \tag{2.30}$$

The right hand side of Eq. 2.30 comes immediately from the fact that $\frac{\partial}{\partial t}\Theta(t - t') = \delta(t - t')$, and the anti-commutator identity for fermionic field operators. The commutator for the single particle operator, $\hat{H}_0$, and the field operator can be separated directly. The final term under the integral sign results from the commutator involving the field operators and the Coulomb interaction.

The number of indices that we require to keep track of everything when describing multi-particle propagators, and, in the next section, when taking functional derivatives, can be very large. Therefore, in order to proceed, we will employ the compressed notation for space, time, and spin: $1 = (\mathbf{r}, t, \sigma)$, $2 = (\mathbf{r}', t', \sigma')$, and so on.

The quantity under the integral sign in Eq. 2.30 is a two particle Green's function:

$$G_2(1,2,3,4) = \frac{1}{i^2}\langle N|T[\hat{\psi}^\dagger(4)\hat{\psi}^\dagger(3)\hat{\psi}(2)\hat{\psi}(1)]|N\rangle. \tag{2.31}$$

Eq. 2.30 therefore expresses the single particle Green's function now defined implicitly in terms of the two particle Green's function. The two particles Green's function is defined in terms of four field operators. The equation of motion for the two particle Green's function would then involve terms with an increasing number of field operators due to the coupling via the Coulomb interaction. This is the heart of the many body problem: an infinite expansion of interaction terms, all of comparable magnitude, due to the strength of the Coulomb coupling.

When trying to solve equations of the form Eq. 2.30 it is convenient to replace the function appearing under the integral sign with a new function, termed a

kernel, and then attempt to solve the system of equations in terms of this kernel. In order to solve Eq. 2.30 and derive the *GW* approximation, we will introduce three new quantities: Σ, P and Γ. Respectively these are named the self-energy, the polarization propagator, and the vertex function. At this stage we introduce the self-energy Σ, by rewriting the integrand in Eq. 2.30 as:

$$\left[i\frac{\partial}{\partial t} - \hat{H}_0\right] G(\mathbf{r},\mathbf{r}',t,t') - \int \Sigma(\mathbf{r},\mathbf{r}'',t,t'')G(\mathbf{r}'',\mathbf{r}',t'',t')d\mathbf{r}''dt'' = \delta(\mathbf{r}-\mathbf{r}')\delta(t-t'). \tag{2.32}$$

The equation now has the shape that we discussed in Sec. 1.3 when discussing the generalized Kohn-Sham exchange correlation potential. The Green's function evolves under the single particle interactions included in $\hat{H}_0$ and according to some non-local, energy dependent potential, Σ. What remains to be done is to show how we can calculate Σ efficiently, and remove the implicit definition of the Green's function in terms of multi-particle propagators.

3.2 Functional derivative of the Green's function

Eq. 2.30 defines the equation of motion for the one particle Green's function by making reference to the two particle Green's function. In the following we will rewrite the equation of motion so that it is entirely defined in terms of the single particle Green's function. This can be accomplished by relating the single particle Green's function to the two particle Green's function via a functional derivative.

To derive Hedin's equation we make some formal modifications. The following derivation follows closely that presented in Appendix A of Ref. [6], the review article of [33] and the textbook of Inkson [28]. A few important functional identities are reproduced in Appendix A. These are required to manipulate the equations and obtain their final closed form.

First Eq. 2.30 is rewritten to include a perturbing potential $\phi(1)$:[2]

$$\left[i\frac{\partial}{\partial t} - \hat{H}_0 - \phi(1)\right] G(1,2) +$$
$$i\int v(1,3)\delta(t_3 - t_1)\langle N|T[\hat{\psi}^\dagger(3)\hat{\psi}(3)\hat{\psi}(1)\hat{\psi}^\dagger(2)]|N\rangle d3 = \delta(1,2). \tag{2.33}$$

The perturbing potential will be set to zero at the end of the derivation.

Eq. 2.33 allows us to separate motion generated by the original Hamiltonian, which is composed of the single electron and electron-electron interaction terms, from the time development due to the perturbation $\phi(1)$. The perturbing potential allows us to define the functional derivative of the system's Green's function, and hence relate the propagation of a single particle to the propagation of multiple particles. The introduction of $\phi(1)$ allows us to generate an infinite series of terms describing the electron-electron interactions in terms of functional derivatives.

Eq. 2.33 is rewritten so that the field operators refer to the ground-state field operators, denoted $\hat{\psi}_0$, and their time development due to $\phi(1)$ is made explicit:

$$G(1,2) = \frac{\langle N|\hat{T}[\hat{S}\hat{\psi}_0(1)\hat{\psi}_0^\dagger(2)]|N\rangle}{\langle N|\hat{S}|N\rangle}. \tag{2.34}$$

The $\hat{S}$ operator propagates the ground-state field operators according to:

$$\hat{S} = T\exp\left[-\mathrm{i}\int_{\mathrm{t_1}}^{\mathrm{t_2}} \phi(2)\hat{\psi}_0(2)\hat{\psi}_0^\dagger(2)\mathrm{d}2\right]. \tag{2.35}$$

This separation ensures the time development of the field operators due to ϕ is made explicit and the field operators have no implicit dependence on the perturbation. In this way the field operators reflect only the dynamics of the underlying electron system interacting via the Coulomb interaction.

By functional differentiation of Eq. 2.34 with respect to the perturbing po-

[2]For our purposes a local scalar potential $\phi(1)$ is sufficient to derive the *GW* approximation. More general perturbations, i.e. coupling to non-local vector potentials is considered in Ref. [33].

tential ϕ the two particle Green's function can be written:

$$G(1,3,2,3^+) = G(1,2)G(3,3^+) - \frac{\delta G(1,2)}{\delta\phi(3)}. \tag{2.36}$$

To arrive at Eq. 2.36 we used the quotient rule as it applies to functional derivatives, and that the variation in S is:

$$\frac{\delta\hat{S}}{\delta\phi(3)} = i\hat{S}\hat{\psi}(3)\hat{\psi}^\dagger(3). \tag{2.37}$$

We can now use Eq. 2.36 to replace the two particle propagator in Eq. 2.30:

$$\left[i\frac{\partial}{\partial t} - \hat{H}_0(1) - V(1)\right] G(1,2) - i\int v(1,3)\frac{\delta G(1,2)}{\phi(3)}d3 \qquad = \delta(1,2), \tag{2.38}$$

where:

$$V(1) = \phi(1) - i\int v(1,3)G(3,3^+)d3. \tag{2.39}$$

Eq. 2.38 has now separated into two terms. The first term contains the single electron components of the Hamiltonian, the perturbing potential, and what can now be identified as the Hartree potential, i.e. the mean field felt by an electron due to the classical potential generated from the electron cloud discussed in Section 1.1. The connection can be seen directly by noting that the quantity $G(3,3^+)$ is the electronic density.

The second term contains the *bare* Coulomb interaction multiplied by the functional derivative of the one particle Green's function. Upon comparison of Eq. 2.38 with Eq. 2.32 we can rearrange terms by observing:

$$\int \Sigma(1,3)G(3,2)d3 = -i\int v(1,3)\frac{\delta G(1,2)}{\delta\phi(3)}d3, \tag{2.40}$$

or by isolating the self-energy Σ as:

$$\Sigma(1,2) = i \int v(1,4) G(1,3) \frac{\delta G^{-1}(4,2)}{\delta \phi(4)} d3d4. \tag{2.41}$$

We now retrieve the equation of motion for the Green's function as it appeared in Eq. 2.32 as:

$$\left[i\frac{\partial}{\partial t} - \hat{H}_0(1) - V(1) \right] G(1,2) - i \int \Sigma(1,3) G(3,2) d3 = \delta(1,2). \tag{2.42}$$

One could formally solve this equation as it stands using an iterative method, however it is worth noting that the resulting expansion of the self-energy Σ would contain increasing powers of the bare Coulomb interaction v. It is unlikely that the resulting series will converge particularly quickly if it converges at all. Therefore it is necessary to expand Σ in a closed form without making reference to the perturbing potential ϕ. In doing so the equations are rearranged so that the bare Coulomb interaction is modified and the electrons experience an effective screened Coulomb interaction. This will be done in the next two sections.

4 Hedin's equations

4.1 Dielectric function

At this point it is useful to introduce the following functional relationships which define the dielectric function in a many-body system. We will switch back to labeling time and space coordinates as $\mathbf{r}, t$ here for ease of reference Section 2.1.

The effective potential acting on the electrons is:

$$V(\mathbf{r}, t) = \phi(\mathbf{r}, t) - i \int v(\mathbf{r}, \mathbf{r}') G(\mathbf{r}', \mathbf{r}', t, t^+) d\mathbf{r}', \tag{2.43}$$

where $iG(\mathbf{r}', \mathbf{r}', t, t^+)$ is the single particle density $n(\mathbf{r}')$. We now define the inverse dielectric function to be the self-consistent variation of this effective potential

with respect to the external perturbing potential:

$$\varepsilon^{-1}(\mathbf{r}, t, \mathbf{r}', t') = \frac{\delta V(\mathbf{r}, t)}{\delta \phi(\mathbf{r}', t')}. \tag{2.44}$$

Upon inserting Eq. 2.43 into Eq. 2.44 we arrive at:

$$\varepsilon^{-1}(\mathbf{r}, t, \mathbf{r}', t') = \delta(\mathbf{r} - \mathbf{r}')\delta(t - t') + \int v(\mathbf{r}, \mathbf{r}'') \frac{\delta n(\mathbf{r}'', t)}{\delta \phi(\mathbf{r}', t')} d\mathbf{r}''. \tag{2.45}$$

Eq. 2.45 has a simple physical interpretation. The inverse dielectric function encodes the self-consistent variation in the charge density with respect to a variation in the potential ϕ. This rearrangement of charge means that the bare Coulomb interaction between two points is altered by the induced screening in the interacting medium. This altered Coulomb interaction is the screened Coulomb interaction, and can be defined in terms of the inverse dielectric function as:

$$W(\mathbf{r}, t, \mathbf{r}', t') = \int v(\mathbf{r}, \mathbf{r}'') \delta(t - t'') \frac{\delta V(\mathbf{r}', t')}{\delta \phi(\mathbf{r}'', t'')} dr'' dt''. \tag{2.46}$$

The screened Coulomb interaction can also be written as an integral equation:

$$W(\mathbf{r}, t, \mathbf{r}', t') = v(\mathbf{r}, \mathbf{r}') + \int d\mathbf{r}''' v(\mathbf{r}, \mathbf{r}''') \int P(\mathbf{r}''', t, \mathbf{r}'', t'') W(\mathbf{r}'', t'', \mathbf{r}', t') dt'' d\mathbf{r}''. \tag{2.47}$$

where the polarizability, P, has been introduced:

$$P(\mathbf{r}, \mathbf{r}', t, t') = \frac{\delta n(\mathbf{r}', t')}{\delta V(\mathbf{r}, t)}. \tag{2.48}$$

Alternatively we can introduce the dielectric function in its non-inverted form as:

$$\epsilon(\mathbf{r}, t, \mathbf{r}', t') = \delta(\mathbf{r} - \mathbf{r}')\delta(t - t') - \int v(\mathbf{r}, \mathbf{r}'') P(\mathbf{r}'', t'', \mathbf{r}', t') \delta(t - t'') d\mathbf{r}'' dt''. \tag{2.49}$$

4.2 Hedin's equations

While the Coulomb repulsion between electrons remains the bare Coulomb interaction, the dielectric function provides a route to interpreting an auxiliary system of quasi-electrons interacting via a *screened* Coulomb interaction.

In order to include this screening implicitly in the definition of the self-energy, we go back to the definition of Σ in Eq. 2.41. We now use the chain rule to take the functional derivative of G with respect to the total potential V rather than the perturbing potential ϕ:

$$\Sigma(1,2) = i \int v(1,4)G(1,3)\frac{\delta G^{-1}(3,2)}{\delta V(5)}\frac{\delta V(5)}{\delta \phi(4)}d3d4d5. \tag{2.50}$$

By comparison of Eqs. 2.44, 2.46, and 2.50 we can combine the inverse dielectric function and the bare Coulomb interaction into the screened Coulomb interaction W:

$$\Sigma(1,2) = i \int W(1,4)G(1,3)\frac{\delta G^{-1}(3,2)}{\delta V(4)}d3d4. \tag{2.51}$$

The final piece of notation to be introduced is the vertex function. This is defined as the variation of the inverse Green's function with respect to the potential V:

$$\Gamma(1,2;3) = \frac{\delta G^{-1}(1,2)}{\delta V(3)}. \tag{2.52}$$

Having obtained the expression for the vertex function in Eq. 2.52 we can write all of Hedin's equations in a closed form. We summarize Hedin's equations describing the interacting Green's function, the screened Coulomb interaction, the

polarizability, and the vertex function of the system:

$$\Sigma(1,2) = i \int W(1^+,4)G(1,3)\Gamma(3,2;4)d4d3 \tag{2.53}$$

$$W(1,2) = \int \varepsilon^{-1}(1,3)v(3,2)d3 \tag{2.54}$$

$$\epsilon(1,2) = \delta(1,2) - \int v(1,3)P(3,2)d3 \tag{2.55}$$

$$P(1,2) = -i \int G(1,3)\Gamma(3,4;2)G(4,1^+)d4d3 \tag{2.56}$$

$$\Gamma(1,2;3) = \delta(1,2)\delta(1,3) + \int \frac{\delta\Sigma(1,2)}{\delta G(4,5)} G(4,6)G(7,5)\Gamma(6,7;3)d4d5d6d7 \tag{2.57}$$

In summary, starting from the equation of motion, and relating the two particle Green's function to the functional derivative of the one particle Green's function with respect to a perturbing potential, we obtained a set of self-consistent equations known as Hedin's equations. When solved iteratively these equations incorporate all the many body effects of a many-electron system.

5 Conclusion

In this chapter we have discussed the Hohenberg-Kohn theorem which states that the ground-state energy of an interacting electronic system is a function of the ground-state charge density. We then discussed the Kohn-Sham scheme, which provides a prescription for obtaining a set of wavefunctions, and eigenvalues, that describe the ground-state density. The various approximations to the exchange correlation functional commonly used in applications of Kohn-Sham DFT were discussed: the LDA, GGA, and hybrid functionals.

We discussed various schemes for extending DFT, a theory for the ground state, to describe excited state properties. In particular we discussed an approach based on Green's function methods to accurately treat processes involving electron addition and removal. Along these lines we presented a detailed discussion of the analytic properties of the Green's function and a full derivation of Hedin's

equations which define the *GW* approximation.

In the next chapter we discuss the details and practicalities of performing DFT and *GW* calculations for real materials.

3 Practical Calculations

In order to apply the theory discussed in chapter 2 to obtain information about the electronic properties of real physical systems, we must discuss some technical aspects: e.g. the basis set needed for representing the electronic wavefunctions and the other operators which appear in the formalism.

Upon having obtained a ground state description of the system from DFT we discuss the operators required to perform GW calculations. We discuss the construction of the Green's function, the polarizability, and the self-energy. We also discuss some of the issues regarding the numerical convergence of these quantities.

Throughout this thesis we will employ a planewaves basis set to represent the electronic wavefunctions obtained via a DFT calculation. We will discuss the advantages and disadvantages of this basis set and describe the construction of the various operators. In particular we will discuss how the electron-ion interaction is treated in a planewaves basis set and techniques for treating the divergence of the Coulomb potential and systems of reduced dimensionality.

Finally, we will discuss how the GW formalism gives us information about the spectral properties of materials, both single particle excitations and collective excitations, and allows us to make contact with experimental data.

1 Single iteration of Hedin's equations: G_0W_0

In this section we discuss the construction of the quantities required to perform a G_0W_0 calculation. We describe the practical application of Hedin's equations discussed in chapter 2 to real materials first demonstrated in Ref. [34] and Refs. [35, 36].

To begin the iterative process Hedin's approach starts with the simplest ap-

proximation to the vertex operator, Eq. 2.57:

$$\Gamma(1,2;3) = \delta(1,2)\delta(1,3). \tag{3.1}$$

The expression for the polarizability, Eq. 2.56, then reduces to:

$$P(1,2) = -iG(1,2)G(2,1^+). \tag{3.2}$$

The polarizability can then be used to construct the dielectric function, Eq. 2.55, the inverse dielectric function, Eq. 2.44, and finally the screened Coulomb interaction, Eq. 2.54.

Using equation Eq. 3.1 and Eq. 2.53 the self-energy becomes:

$$\Sigma(1,2) = iG(1,2)W(1^+,2). \tag{3.3}$$

From the self-energy we can construct and solve the quasiparticle equation, Eq. 2.12 to correct the eigenvalues and eigenvectors obtained from a DFT calculation. In the remainder of this chapter we describe how, starting from a set of one electron states and eigenvalues provided by a Kohn-Sham DFT calculation, we can construct explicit expressions for each of these quantities: the Green's function, the polarizability, and the screened Coulomb interaction.

1.1 Calculating the polarizability

The first work using the Green's function approach to study the interacting electron problem with the effect of the ionic lattice included was in Ref. [37]. By disrupting translational symmetry the electron cloud becomes distorted, and the atomic scale variation in charge density means the screening will take on a more complicated form.

The work of Ref. [37] used the Green's function techniques of Martin and Schwinger [19] to deduce some of the important changes that will occur as a

result of the introduction of a crystal lattice. The work presented in Ref. [37] was subsequently refined by Adler and Wiser in Refs. [38] and [39] respectively leading to the standard Adler-Wiser expression for the polarizability:

$$P(\mathbf{r},\mathbf{r}';\omega) = 2\sum_{nm}\frac{f_n - f_m}{\epsilon_n - \epsilon_m - \omega}\phi_m^*(\mathbf{r})\phi_n(\mathbf{r})\phi_m(\mathbf{r}')\phi_n^*(\mathbf{r}'), \tag{3.4}$$

where f_n and f_m are the fermion occupation factors for states n, m (1 if occupied and 0 if unoccupied), and the factor 2 is for spin degeneracy.

Eq. 3.4 is a sum over the entire manifold of valence and conduction states. The convergence of the polarizability with respect to the number of conduction states included in the sum is slow and a point worthy of some discussion. The slow convergence has been demonstrated for transition metal oxides [40–43], standard semiconductors like silicon, germanium, and gallium arsenide [44], and for chalcogenide based photovoltaic interfaces [45]. In chapter 4 and chapter 5 we will discuss alternative formulations which avoid the construction of the polarizability as a sum over states.

1.2 The Screened Coulomb interaction

The dielectric function is defined as:

$$\varepsilon(\mathbf{r},\mathbf{r}';\omega) = \delta(\mathbf{r},\mathbf{r}') - v(\mathbf{r},\mathbf{r}')P(\mathbf{r},\mathbf{r}';\omega). \tag{3.5}$$

An inversion of Eq. 3.5 is then required to form the inverse dielectric function. From the inverse dielectric function we can then construct the screened Coulomb interaction:

$$W(\mathbf{r},\mathbf{r}';\omega) = \epsilon^{-1}(\mathbf{r},\mathbf{r}';\omega)v(\mathbf{r},\mathbf{r}'). \tag{3.6}$$

1.3 Plasmon-pole model

To mitigate the workload required for constructing the polarizability at every frequency ω, various approximations to the dynamical dependence of the operator have been proposed. The plasmon-pole model was one of the first methods for efficiently describing the frequency dependence of the screened Coulomb interaction when constructing the self-energy. Two of the most commonly used plasmon-pole models employed in *ab initio* calculations were developed in Ref. [36] and Ref. [46]. The physics of the plasmon-pole model has a long history and goes back to some of the earliest work which discussed the electron gas interacting via collective excitations [47]. Overhauser gives a thorough discussion of the electron gas interacting via plasmons, [48], and performs a calculation of the correlation energy of an electron gas using a plasmon-pole model.

The plasmon-pole model assumes a single pole structure in the screened Coulomb interaction. This implies there are two free parameters: the energy of the pole and its oscillator strength. These parameters can be determined by calculating the dielectric response at two points. In the Godby-Needs method [46] one generally chooses to calculate $\varepsilon^{-1}(\omega)$ at $\omega = 0$ and $\omega = i\omega_p$, where ω_p is the classical plasma frequency. This model reproduces the static dielectric constant and approximates the first moment of the actual dielectric response. The Hybertsen-Louie model Ref. [36] takes a slightly different approach. The frequency dependence of the screened Coulomb interaction is also represented using a single pole however, the two parameters of the model are fixed using the static dielectric constant and then applying the f-sum rule [36].

The suitability of the plasmon-pole model for systems with a single well defined collective excitation is well established [30]. Recently,however, see for instance studies performed on ZnO, the *GW* gap quasiparticle gap has been shown to be very sensitive to the plasmon-pole model that is used [40–42]. In addition, in systems with reduced dimensionality the plasmon-pole model is an inadequate

approximation to the frequency dependence of the screened Coulomb interaction. This motivates the development of alternative strategies not requiring the approximation.

An alternative fitting procedure to the plasmon-pole model is the use of Padé approximants, which allow us to analytically continue quantities to the real axis that are calculated on the imaginary axis. This has been demonstrated in Refs. [49–54]. We will discuss this procedure in detail in Chapter 5.

1.4 The Green's function and the self-energy

The non-interacting Green's function can be defined in terms of the single particle eigenvectors:

$$G(\mathbf{r},\mathbf{r}';\omega) = \sum_n \frac{\phi_n(\mathbf{r})\phi_n^\star(\mathbf{r}')}{\epsilon_n - \omega \pm i\eta}. \tag{3.7}$$

where η is a positive infinitesimal and the $\pm$ refers to conduction states and valence states respectively.

Having constructed the single particle Green's function and the screened Coulomb interaction the self-energy can be constructed as a convolution in the frequency domain:

$$\Sigma(\mathbf{r},\mathbf{r}';\omega) = i\int G(\mathbf{r},\mathbf{r}';\omega-\omega')W(\mathbf{r},\mathbf{r}',\omega')e^{i\omega'\delta}d\omega'. \tag{3.8}$$

Eq. 3.8 is often split into two contributions:

$$\Sigma(\mathbf{r},\mathbf{r}';\omega) = \Sigma^{\mathrm{X}}(\mathbf{r},\mathbf{r}') + \Sigma^{\mathrm{C}}(\mathbf{r},\mathbf{r}';\omega). \tag{3.9}$$

The first part is the bare exchange contribution, which runs over the occupied manifold, and can be written as:

$$\Sigma^{\mathrm{X}}(\mathbf{r},\mathbf{r}') = \sum_{v\in occ} v(\mathbf{r},\mathbf{r}')\phi_v(\mathbf{r})\phi_v^\star(\mathbf{r}') \tag{3.10}$$

The second part is the correlation contribution to the self-energy.

$$\Sigma^{\mathrm{C}}(\mathbf{r},\mathbf{r}';\omega) = i\int G(\mathbf{r},\mathbf{r}';\omega+\omega')\left[W(\mathbf{r},\mathbf{r}';\omega') - v(\mathbf{r},\mathbf{r}')\right]d\omega'. \tag{3.11}$$

The construction of the self-energy in this manner is known as the G_0W_0 approximation. It involves a single iteration of Hedin's equations using the simplest approximation to the vertex operator. Before discussing the connection of the self-energy to experiment, and how it can be used to calculate quasiparticle corrections to the ground state we discuss the practical side of performing electronic structure calculations on real materials.

2 Planewaves and pseudopotentials

2.1 Planewave basis set

A planewave basis is an effective way of describing the spatial structure of wave functions in a crystal. We introduce the vectors $\mathbf{a}_1$, $\mathbf{a}_2$, and $\mathbf{a}_3$ which define the primitive unit cell of a crystal and reflect the smallest rigid translation of the lattice which commutes with the Hamiltonian. The volume of the real space unit cell,Ω, is then given by:

$$\Omega = |\mathbf{a}_1 \cdot (\mathbf{a}_2 \times \mathbf{a}_3)|. \tag{3.12}$$

Any vector of the real space lattice is then given by:

$$\mathbf{R} = n_1\mathbf{a}_1 + n_2\mathbf{a}_2 + n_3\mathbf{a}_3, \tag{3.13}$$

where n_1, n_2, n_3, are integers. Primitive reciprocal lattice vectors can then be constructed from the real space lattice vectors via:

$$\mathbf{b}_1 = 2\pi\frac{\mathbf{a}_2 \times \mathbf{a}_3}{\mathbf{a}_1 \cdot (\mathbf{a}_2 \times \mathbf{a}_3)}, \tag{3.14}$$

with vectors $\mathbf{b}_2$, and $\mathbf{b}_3$ obtained via cyclic permutations of the indices. The reciprocal lattice vectors can then be defined:

$$\mathbf{G} = n_1\mathbf{b}_1 + n_2\mathbf{b}_2 + n_3\mathbf{b}_3, \tag{3.15}$$

where again n_1, n_2, n_3 are all integers.

The planewaves basis set provides a uniform basis for describing the entire unit cell. Hence there is no sampling bias in a planewave basis set towards a particular region of space.

Using the reciprocal lattice vectors $\mathbf{G}$, the electronic wave functions can be expanded in terms of planewaves:

$$\phi_{n\mathbf{k}}(\mathbf{r}) = e^{i\mathbf{k}\cdot\mathbf{r}}\frac{1}{\sqrt{\Omega}}\sum_{\mathbf{G}} u_{n\mathbf{k}}(\mathbf{G})e^{i\mathbf{G}\cdot\mathbf{r}} \tag{3.16}$$

The $\phi_{n\mathbf{k}}(\mathbf{r})$ are known as Bloch wavefunctions. The translational symmetry of the lattice means each wave function in the crystal can be indexed with a wavevector $\mathbf{k}$ and a band index n. A Bloch wave function is composed of two parts: a cell periodic part $u_{n\mathbf{k}}(\mathbf{r})$ and a phase contributed by $e^{i\mathbf{k}\cdot\mathbf{r}}$. The cell periodic part of the Bloch wave function satisfies the relation: $u_{n\mathbf{k}}(\mathbf{r}) = u_{n\mathbf{k}}(\mathbf{r}+\mathbf{R})$.

In atomic units the quantity $\frac{1}{2}|\mathbf{G}|^2$ has the same units as energy. The energy cutoff on the basis, $E_c = \frac{1}{2}|\mathbf{G}_{\max}|^2$, where $\mathbf{G}_{\max}$ denotes the largest magnitude planewave included in the calculation, determines the smallest variation in real space that can be described.

In addition to the electronic wave functions, we will also expand the polarizability, the Green's function, and the screened Coulomb interaction in terms of planewaves. Given the lattice and the reciprocal lattice a generic function of one variable can be expanded as:

$$F(\mathbf{r}) = \frac{1}{\sqrt{\Omega}}\sum_{\mathbf{kG}} f_{\mathbf{k}}(\mathbf{G})e^{i(\mathbf{k}+\mathbf{G})\cdot\mathbf{r}}. \tag{3.17}$$

For expanding functions of two variables we will use the convention:

$$F(\mathbf{r},\mathbf{r}',\omega) = \frac{1}{N_{\mathbf{k}}\Omega}\sum_{\mathbf{kGG}'} \mathrm{e}^{-i(\mathbf{k}+\mathbf{G})\cdot\mathbf{r}} f_{[\mathbf{k},\mathbf{G},\omega]}(\mathbf{G}')\mathrm{e}^{i(\mathbf{k}+\mathbf{G}')\cdot\mathbf{r}'}. \tag{3.18}$$

2.2 Pseudopotentials

The description of the interaction between valence electrons and nuclei and core electrons is handled using the pseudopotential formalism [2]. The variations in the electronic wave function near the nucleus are rapid because of orthogonalization constraints between electrons in the system and the divergence of the electron-nuclear Coulomb interaction.

The idea behind pseudopotentials is that an effective form for the electron-ion interaction can be constructed, which does not necessitate very high energy planewaves. The pseudopotential procedure generates wave functions which are smooth and effectively represented using Eq. 3.16 in the inter-atomic region. The wavefunctions are generated by choosing a cutoff radius, r_c, centered on a nucleus, and then performing an all-electron calculation to obtain the atomic wave functions. The pseudized wave functions are then matched to the all electron wave functions outside of r_c. The procedure is required not only to provide smooth wave functions outside the core region, but also guarantee that the scattering properties of the pseudopotential and the all-electron ion are the same. The introduction of norm conserving pseudopotentials,[55], ultrasoft pseudopotentials [56], and projector augmented waves, [57], now enable accurate electronic structure calculations while keeping the number of planewaves manageable. In this thesis we only employ norm conserving pseudopotentials of the type described in Ref. [58]. The scheme imposes the following requirements:

1. The radial integrals from 0 to r of the charge densities for the pseudo and all-electron wave functions agree for $r > r_c$.

2. The logarithmic derivatives of the all-electron and pseudo wave function and their first energy derivatives agree at the cutoff radius.

The potential thus generated is frequently represented using the Kleinman-Bylander formulation Ref. [59]. In Ref. [59] a factorization of the non-local potential into two contributions, a local contribution, $V_{\rm loc}(\mathbf{r})$ and a non-local, angular-momentum dependent part:

$$\int \hat{V}^{\rm NC}(\mathbf{r},\mathbf{r}')\phi_{n\mathbf{k}}(\mathbf{r}')d\mathbf{r}' = V_{\rm loc}(\mathbf{r})\phi_{n\mathbf{k}}(\mathbf{r}) + \sum_{l\neq l_{\rm loc}}\sum_{m}\chi_{lm}(\mathbf{r})E_l\int\chi^*_{lm}(\mathbf{r}')\phi_{n\mathbf{k}}(\mathbf{r}')d\mathbf{r}', \tag{3.19}$$

the scalar value E_l determines the magnitude and sign of the scattering potential in a particular angular momentum channel. The number of angular momentum channels is determined by the atom for which one is constructing a pseudopotential. The choice of which angular momentum channel is represented locally in the pseudopotential $V_{\rm loc}(\mathbf{r})$ and which are described via the projector functions χ depends on the atomic system under consideration. The rule of thumb is to choose the local component of the pseudopotential as the highest angular momentum channel in the pseudopotential.

The use of pseudopotentials within the *GW* approximation requires some discussion. Following Ref. [60] we split the Green's function into two contributions: $G = G_c + G_v$ where G_c is the contribution to the Green's function from the core electrons and G_v is the contribution stemming from the valence electrons. The polarizability is divided in similar manner $P = P_c + P_v$. This allows us to define a self-energy decomposed into three terms:

$$\Sigma = i\frac{(G_c+G_v)v}{1-v[P_v+P_c]} \tag{3.20}$$

$$\Sigma = iG_cW + iG_vW_vP_cW_v + iG_vW_v \tag{3.21}$$

As observed in Ref. [61] the length scale of the core electrons is typically much

smaller than the characteristic screening radius, hence the first term energy contribution is essentially a bare core-valence exchange term. The second term relates to the polarizability of the atomic core and can become significant for higher atomic numbers.

Efforts to include the effects of core polarization in pseudopotential based *GW* calculations has also been made in Refs. [62, 63]. The contribution of the additional terms in the self-energy resulting from the core electrons and the resulting differences between pseudopotential and all electron *GW* calculations have been studied explicitly in Refs. [24, 44, 64–66].

Provided all relevant valence electrons are treated explicitly in the pseudopotential framework satisfactory consistency can be obtained between all electron and pseudo potential *GW* calculations.

2.3 Kohn-Sham equation with planewaves

Having discussed the treatment of the electron-ion interaction, we briefly describe the construction and application of the remaining operators in the Kohn-Sham Hamiltonian:

$$\left[-\frac{1}{2}\nabla^2 + V^{\mathrm{H}}(\mathbf{r}) + V^{\mathrm{xc}}(\mathbf{r}) + V^{\mathrm{ion}}\right]\phi_{n\mathbf{k}}(\mathbf{r}) = \epsilon_{n\mathbf{k}}\phi_{n\mathbf{k}}(\mathbf{r}). \tag{3.22}$$

The action of $V^{\mathrm{xc}}(\mathbf{r})$ is applied in real space. The value of $V^{\mathrm{xc}}(\mathbf{r})$ is determined as a scalar function of the electronic density, $n(\mathbf{r})$, at the point $\mathbf{r}$ and is computed as a product, $V^{\mathrm{xc}}(\mathbf{r})\phi_{n\mathbf{k}}(\mathbf{r})$, with the wavefunction in real space.

The Hartree potential is most conveniently calculated from the Poisson equation in reciprocal space:

$$V^{\mathrm{H}}(\mathbf{G}) = \frac{4\pi n(\mathbf{G})}{|\mathbf{G}|^2}. \tag{3.23}$$

The Hartree potential, $V^{\mathrm{H}}(\mathbf{G})$, can be applied to the wave function in reciprocal space and the product Fourier transformed back into real space. For $|\mathbf{G}| = 0$

there is a divergence in the Hartree potential. In a ground state calculation of a charge neutral system this divergence is canceled by the compensating background potential of the nuclei and the $V^H(\mathbf{G}=0)$ term is typically set to zero. The kinetic energy operator is calculated and applied in reciprocal space.

2.4 Truncation of the Coulomb interaction

In real space the Coulomb potential is:

$$v(\mathbf{r},\mathbf{r}') = \frac{4\pi}{|\mathbf{r}-\mathbf{r}'|}. \tag{3.24}$$

In reciprocal space the bare Coulomb interaction is:

$$v(\mathbf{q}) = \frac{4\pi}{|\mathbf{q}|^2}, \tag{3.25}$$

which diverges when $\mathbf{q}=0$. A further problem is the slow decay of the Coulomb potential as $1/|\mathbf{r}|$. For systems of reduced dimensionality, i.e. two dimensional slab geometries or isolated molecules, this can lead to spurious Coulomb interactions between the repeated images. A number of approaches have been proposed to treat the divergence systematically, and eliminate the periodic interaction. In this thesis we use the methods described in Ref. [67] and Ref. [68] to truncate the Coulomb interaction so that the divergence is avoided and there is no spurious interaction between periodic images.

Spherical Truncation

In isolated systems with spherical symmetry a cutoff in real space to the Coulomb interaction can be introduced. In real space the modified Coulomb interaction takes the form:

$$v(\mathbf{r},\mathbf{r}') = \frac{\Theta(R_c - |\mathbf{r}-\mathbf{r}'|)}{|\mathbf{r}-\mathbf{r}'|}, \tag{3.26}$$

where R_c is the chosen cut-off radius in real space. The reciprocal space representation of the truncated interaction now takes the modified form:

$$v(\mathbf{q}) = \frac{4\pi}{|\mathbf{q}|^2}\left[1 - \cos(\mathrm{R_c}|\mathbf{q}|)\right]. \tag{3.27}$$

The $|\mathbf{q}| = 0$ case is then well defined:

$$v(|\mathbf{q}| = 0) = \frac{4\pi \mathrm{R_c^2}}{2} \tag{3.28}$$

For crystalline systems we follow the suggestion of Ref. [68] and define the cutoff radius, R_c, as:

$$\mathrm{R_c} = (\frac{3}{4\pi}\Omega \mathrm{N})^{\frac{1}{3}}, \tag{3.29}$$

where N is the number primitive unit cells in the equivalent supercell determined by the sampling of the Brillouin zone.

2D Truncation

For slab geometries we employ the truncation strategy of Ref. [67]. The effect of periodic image interaction is particularly relevant in 2D systems [69, 70]. For the 2D system the following modification to the Coulomb potential in real space has been proposed in Ref. [67]:

$$v_c^{2D}(\mathbf{r}, \mathbf{r}') = \frac{\Theta(z_c - z)}{|\mathbf{r} - \mathbf{r}'|}. \tag{3.30}$$

Where the slab is infinitely extended in the x and y directions, and z_c is the the truncation height, beyond which the Coulomb potential is set to zero. The Fourier transform of v_c^{2D} is:

$$v_c^{2D}(\mathbf{q}) = \frac{4\pi}{|\mathbf{q}|^2}\left[1 + e^{-|\mathbf{q}_{\mathrm{xy}}|\mathrm{z_c}}\left(\frac{|\mathbf{q}_z|}{|\mathbf{q}_{xy}|}\sin(|\mathbf{q}_z|z_c) - \cos(|\mathbf{q}_z|z_c)\right)\right]. \tag{3.31}$$

Let R_z be the length of the crystal cell along z. If the cutoff z_c is chosen to be $z_c = R_z/2$ all the $\sin(|\mathbf{q}_z|z_c)$ terms are zero. This leads to the proposed truncation in reciprocal space:

$$v_c^{2D}(\mathbf{q}) = \frac{4\pi}{|\mathbf{q}|^2}\left[1 - e^{-|\mathbf{q}_{xy}|z_c}\cos(|\mathbf{q}_z|z_c)\right]. \tag{3.32}$$

By employing a modified Coulomb interaction appropriate for spherical and 2-dimensional geometries, the divergence in the Coulomb potential can be handled numerically, and computational savings can be achieved without the need to incorporate large vacuum regions in the model to prevent artificial image interaction.

3 G_0W_0 self-energy and corrections to LDA eigenvalues

In the first section of this chapter we have discussed the procedure for constructing the G_0W_0 self-energy operator. We have also discussed some of the considerations required when performing DFT calculations within a planewaves basis set. It remains to show how the G_0W_0 self-energy can be used to connect the eigenvalues obtained from a DFT calculation.

We proceed as in Ref. [36] by assuming the G_0W_0 self-energy can be treated as a perturbation to the DFT Kohn-Sham exchange and correlation potential.

In Chapter 2 we discussed the quasiparticle equation:

$$\left[-\frac{1}{2}\nabla^2 + \hat{V}^{\text{ion}} + \hat{V}^{\text{H}}\right]\phi_{n\mathbf{k}}(\mathbf{r}) + \int d\mathbf{r}'\Sigma(\mathbf{r},\mathbf{r}';E_{n\mathbf{k}})\phi_{n\mathbf{k}}(\mathbf{r}') = E_{n\mathbf{k}}\phi_{n\mathbf{k}}(\mathbf{r}). \tag{3.33}$$

By adding and subtracting $V_{xc}(\mathbf{r})\psi_{n\mathbf{k}}(\mathbf{r})$ one obtains:

$$(-\frac{1}{2}\nabla^2+\hat{V}^{\text{ion}}+\hat{V}^{\text{H}}+\hat{V}^{\text{xc}})\phi_{n\mathbf{k}}(\mathbf{r})+\int d\mathbf{r}'\left[\Sigma(\mathbf{r},\mathbf{r}';E_{n\mathbf{k}}) - \hat{V}^{\text{xc}}(\mathbf{r}')\delta(\mathbf{r},\mathbf{r}')\right]\phi_{n\mathbf{k}}(\mathbf{r}') = E_{n\mathbf{k}}\phi_{n\mathbf{k}}(\mathbf{r}). \tag{3.34}$$

If we treat $\Sigma - V^{\text{xc}}$ as a perturbation we can express $E_{n\mathbf{k}}$ in terms of the Kohn-

Sham eigenvalues $\epsilon^{\mathrm{LDA}}_{n\mathbf{k}}$ using first order perturbation theory:

$$E^{\mathrm{QP}}_{n\mathbf{k}} = \epsilon^{\mathrm{LDA}}_{n\mathbf{k}} + \langle n\mathbf{k}|\Sigma(E^{\mathrm{QP}}_{n\mathbf{k}}) - \hat{V}^{\mathrm{xc}}|n\mathbf{k}\rangle. \tag{3.35}$$

Following Ref. [36] we expand the self-energy operator to first order around the LDA eigenvalue:

$$\Sigma(E^{\mathrm{QP}}_{nk}) = \Sigma(\epsilon^{\mathrm{LDA}}_{nk}) + \left.\frac{\partial\Sigma(\omega)}{\partial\omega}\right|_{\omega=\epsilon^{\mathrm{LDA}}_{n\mathbf{k}}} (E^{\mathrm{QP}}_{n\mathbf{k}} - \epsilon^{\mathrm{LDA}}_{n\mathbf{k}}). \tag{3.36}$$

The quasiparticle energy can than be obtained by substituting Eq. 3.36 into Eq. 3.35:

$$E^{\mathrm{QP}}_{n\mathbf{k}} = \epsilon^{\mathrm{LDA}}_{n\mathbf{k}} + \left(1 - \left.\frac{\partial\Sigma(\omega)}{\partial\omega}\right|_{\omega=\epsilon^{\mathrm{LDA}}_{n\mathbf{k}}}\right)^{-1} (E^{\mathrm{QP}}_{n\mathbf{k}} - \epsilon^{\mathrm{LDA}}_{n\mathbf{k}}). \tag{3.37}$$

The quasiparticle renormalization value Z is defined by:

$$Z_{n\mathbf{k}} = \left[1 - \left.\frac{\partial\Sigma(\omega)}{\partial\omega}\right|_{\omega=\epsilon^{\mathrm{LDA}}_{n\mathbf{k}}}\right]^{-1}. \tag{3.38}$$

In summary, we find the expression for the G_0W_0 perturbative correction to the LDA eigenvalues is:

$$E^{\mathrm{QP}}_{n\mathbf{k}} = \epsilon^{\mathrm{LDA}}_{n\mathbf{k}} + Z_{n\mathbf{k}}\langle n\mathbf{k}|\Sigma(\epsilon^{\mathrm{LDA}}_{n\mathbf{k}}) - V^{xc}_{n\mathbf{k}}|n\mathbf{k}\rangle. \tag{3.39}$$

4 The Spectral function

4.1 The GW spectral function

In this section we introduce the spectral function. For simplicity we will contract the block notation $n\mathbf{k}$ to a single index n, and then reintroduce the full Bloch notation when we arrive at the final expression for the spectral function.

Given a set of single particle eigenvectors $\phi_m(\mathbf{r})$ we can take matrix elements

of the single particle states with the Green's function and self-energy:

$$G_{mn}(\omega) = \int\int \phi_m^\star(\mathbf{r}) G(\mathbf{r},\mathbf{r}';\omega)\phi_n(\mathbf{r}')d\mathbf{r}d\mathbf{r}', \tag{3.40}$$

$$\Sigma_{mn}(\omega) = \int\int \phi_m^\star(\mathbf{r}) \Sigma(\mathbf{r},\mathbf{r}';\omega)\phi_n(\mathbf{r}')d\mathbf{r}d\mathbf{r}'. \tag{3.41}$$

We can employ the same notation for matrix elements with $V^{\mathrm{xc}}(\mathbf{r})$, and the Kohn-Sham Hamiltonian $\hat{H}^{\mathrm{KS}}$. In matrix notation the Dyson equation [28] can be written:

$$G^{-1} = G_0^{-1} - [\Sigma(\omega) - V_{\mathrm{xc}}]. \tag{3.42}$$

Eq. 3.42 gives the expression for interacting Green's function. We note that the exchange and correlation potential of the ground state calculation is subtracted from the final self-energy. If the Green's function is diagonal in the state indices we can invert each element of the matrix and write:

$$G_{nn}(\omega) = \frac{1}{\omega - \epsilon_n^{\mathrm{KS}} + \mathrm{Re}\Sigma_{nn}(\omega) - V_{nn}^{\mathrm{xc}} + \mathrm{Im}\Sigma_{nn}(\omega)}. \tag{3.43}$$

In the case where the non-diagonal elements cannot be ignored, a full matrix inversion would be required to construct the Green's function:

$$G_{mn}(\omega) = [\omega\delta_{mn} - \epsilon_{mn}^{\mathrm{KS}}\delta_{mn} + \mathrm{Re}\Sigma_{mn}(\omega) - V_{nn}^{\mathrm{xc}} + \mathrm{Im}\Sigma_{mn}(\omega)]^{-1}. \tag{3.44}$$

At this stage we introduce the spectral function by defining it in terms of the Green's function:

$$A_{mn}(\omega) = \mathrm{Im}|G_{mn}(\omega)|. \tag{3.45}$$

Reintroducing the Bloch notation we can write the full spectral function for the diagonal Green's function:

$$A_{\mathbf{k}}(\omega) = \frac{1}{\pi}\sum_n \frac{|\mathrm{Im}\Sigma_{n\mathbf{k}}(\omega)|}{[\omega - \epsilon_{n\mathbf{k}} - (\mathrm{Re}\Sigma_{n\mathbf{k}}(\omega) - V_{n\mathbf{k}}^{\mathrm{xc}})]^2 + [\mathrm{Im}\Sigma_{n\mathbf{k}}(\omega)]^2}. \tag{3.46}$$

The spectral function helps clarify the quasiparticle picture. Eq. 3.46 is strongly peaked when the frequency ω sweeps through the renormalized eigenvalue $\epsilon_{n\mathbf{k}} + \mathrm{Re}(\Sigma_{n\mathbf{k}}(\omega) - V^{\mathrm{xc}}_{n\mathbf{k}})$. Given the frequency dependence of Σ additional zeros in the real part of the denominator of Eq. 3.46 are possible. These can correspond to the appearance of new excitations which are not present in the non-interacting system. Finally the imaginary part of the self-energy introduces a broadening of the the quasiparticle peak and is associated with lifetime effects.

4.2 Contact with experiment

Angle Resolved Photoemission Spectroscopy (ARPES) is a very useful probe for investigating the electronic structure of materials [3]. The intensity of the electrons captured at the experimental detector, $I_{\mathbf{k}}(\omega)$, can be expressed in terms of the quasiparticle spectral function [3]:

$$I_{\mathbf{k}}(\omega) = I_0(\mathbf{k}, \nu) f(\omega) A_{\mathbf{k}}(\omega), \tag{3.47}$$

Where ν is the frequency of the incident radiation and $f(\omega)$ is the Fermi-Dirac distribution. The factor $I_0(\mathbf{k}, \nu)$ includes matrix element effects, i.e. the strength of the coupling of the initial and final electron states via the electromagnetic probe, the effect of surfaces, and inelastic scattering in the sample [3].

4.3 Bardyszewski-Hedin theory of photoemission

A comprehensive analysis of the connection between the spectral function and photoemission data is given by Bardyszewski and Hedin in Ref. [71]. Their formulation begins by relating the photocurrent, J, i.e. the number of electrons ejected from the sample, per unit solid angle and energy to the intensity, I, measured at the detector:

$$\frac{\partial^2 J}{\partial \Omega \partial \epsilon_{\mathbf{k}}} \sim I. \tag{3.48}$$

The standard definition for the intensity is then given in Refs. [72, 73]:

$$I = \sum_s |\langle \mathbf{k}, N-1, s|\hat{\Delta}|N\rangle|^2 \delta(\epsilon_{\mathbf{k}} - \epsilon_s - \omega). \tag{3.49}$$

The $|\mathbf{k}, N-1, s\rangle$ state is a product state of the photoelectron with wave vector $\mathbf{k}$ and the $|N-1, s\rangle$ many electron wavefunction described in Eq. 2.21. The frequency of the incoming radiation is ω. The $\hat{\Delta}$ operator is the electric dipole operator.

Eq. 3.49 explicitly couples many-body states via the dipole operator. The intrinsic contribution of a particular photoelectron $\tilde{\phi}_{\mathbf{k}}$, to the measured photocurrent can now be written in terms of the one-electron spectral function discussed in Section 4.1 [71]:

$$I(\mathbf{k}, \omega) = \int \tilde{\phi}^{\star}_{\mathbf{k}}(\mathbf{r})\hat{\Delta}(\mathbf{r})A(\mathbf{r}, \mathbf{r}'; \epsilon_{\mathbf{k}} - \omega)\hat{\Delta}(\mathbf{r}')\tilde{\phi}_{\mathbf{k}}(\mathbf{r}')d\mathbf{r}d\mathbf{r}'. \tag{3.50}$$

If we assume the spectral function is diagonal in $\mathbf{r}$, $\mathbf{r}'$, and exploit the matrix notation for the spectral function from the previous section we arrive at the expression:

$$I(\mathbf{k}, \omega) \approx \sum_n |\langle \tilde{\phi}_{\mathbf{k}}|\hat{\Delta}|\phi_n\rangle|^2 A_{nn}(\epsilon_{\mathbf{k}} - \epsilon_n - \omega). \tag{3.51}$$

The photoelectron will not generally travel unimpeded to the detector. Along the way the photoelectron can scatter off of phonons, plasmons, or other particle-hole excitations. Ref. [71] provides a detailed derivation of the expressions reported here for the intrinsic intensity of the photocurrent and the possible types of quasiparticle excitations in an interacting system. These results are mentioned here because they provide a direct connection between experimental probes and the mathematical formalism of the *GW* approximation.

5 Conclusion

In this chapter we have described the steps required for the construction of the G_0W_0 self-energy. We have also discussed the basics of the planewaves pseudopotential framework for performing DFT calculations. We have discussed the treatment of divergences and spurious periodic image interaction in the Coulomb operator.

We concluded by discussing how the self-energy and the interacting Green's function obtained from a GW calculation can be used to correct the eigenvalues from the ground state calculation, and to construct the quasiparticle spectral function. Finally the relationship between the spectral function and ARPES experiments was discussed.

In the next chapter we will provide a summary of the scaling properties and numerical challenges of standard GW calculations. We will also describe various attempts to improve the efficiency and accuracy of the procedure.

4 Alternative Approaches to Performing GW Calculations

As we have discussed, GW calculations represent a well established theoretical and computational framework for studying electronic excitations. Excitation energies calculated using the GW method are generally in good agreement with experiment in many cases, from bulk solids [36] to surfaces and interfaces, [74–76] defects, [77], and molecules Ref. [78].

Despite the successes of the GW method and the growing interest in this technology, the computational workload remains considerably heavier than in ordinary density-functional theory (DFT) calculations. As a rule of thumb, while standard DFT total energy calculations scale as N^3, N being the number of atoms in the system, the scaling of GW calculations is of the order of N^4.

In the previous chapter we discussed the sum-over-states method for performing GW calculations and highlighted the slow convergence of the GW corrections with respect to the number of empty bands included in the terms for the polarizability and the Green's function. In this chapter we will describe alternative means of performing GW calculations which have been developed recently.

The developments can be classified in two different groups: direct methods and effective energy techniques. The former class involves the direct calculation of the polarizability and the Green's function by solving a linear system of equations, the latter seeks to reduce the computational workload of the sum-over-states technique by rewriting the required quantities in terms of occupied states only. We will discuss the details of both methods, and their scaling properties. In this chapter we will also discuss recent work which moves beyond the G_0W_0 approximation described in the previous chapter.

1 *GW* with optimal polarizability basis and Lanczos recursion

In this section we discuss an approach to performing *GW* calculation based on the construction of a new basis for the polarizability operator and the use of Lanczos recursion techniques. For convenience we will refer to the total approach as the *GWL* method, as proposed in Ref. [79], and Ref. [80]. The two objectives of the method are to eliminate the sum-over-states Green's function in the polarizability, and to reduce the size of the basis set required to represent the polarizability.

The first step in the method is the construction of an optimal basis for the polarizability. The method starts from the description of the polarizability in the time domain:

$$\hat{P}_0(\tau) = \sum_{cv} \phi_c(\mathbf{r})\phi_v(\mathbf{r})\phi_c^*(\mathbf{r}')\phi_v^*(\mathbf{r}')e^{-i(\epsilon_c-\epsilon_v)\tau}, \tag{4.1}$$

where $\tau = (t - t')$. The first approximation in the *GWL* approach is to assume that the eigenvectors of the static polarizability matrix:

$$\hat{P}_0(\tau = 0) = \sum_{cv} |\phi_v(\mathbf{r})\phi_c(\mathbf{r})\rangle\langle\phi_c(\mathbf{r}')\phi_v(\mathbf{r}')|, \tag{4.2}$$

span the same space as the the eigenvectors of the full dynamic polarizability. The eigenvectors Φ_μ and eigenvalues λ_μ of the matrix in Eq. 4.2 are obtained using a singular value decomposition of the matrix:

$$\hat{P}_0(\tau = 0)\Phi_\mu = \lambda_\mu\Phi_\mu. \tag{4.3}$$

Only eigenvalues greater than a selected numerical value are kept to describe the polarizability.

Two transformations are made to reduce the dimension of the polarizability basis. First the occupied manifold of states, ϕ_v, are transformed into maximally

localized Wannier functions, w_v, using the procedure described in Ref. [81]. The second transformation is that all conduction states up to an energy $E^\star$ are replaced with planewaves, which have been orthogonalized to the valence manifold:

$$|\tilde{\mathbf{G}}_c\rangle = \left[1 - \sum_v |\phi_v\rangle\langle\phi_v|\right] |\mathbf{G}\rangle, \tag{4.4}$$

where the coordinate representation of the vector $|\mathbf{G}\rangle$ is given by: $\langle\mathbf{r}|\mathbf{G}\rangle = e^{i\mathbf{G}\cdot\mathbf{r}}$.

Using these two transformations the static polarizability in Eq. 4.2, takes the form:

$$\hat{P}_0(t=0) = \sum_{vc} |w_v\tilde{\mathbf{G}}_c\rangle\langle w_v\tilde{\mathbf{G}}_c|. \tag{4.5}$$

It is in this form that the singular value decomposition is performed.

The frequency dependent polarizability is then represented as a sum over the eigenvectors, Φ_μ, of the static polarizability:

$$\hat{P}_0(\mathbf{r},\mathbf{r}';i\omega) \approx \sum_{\mu\nu} \Phi_\mu(\mathbf{r}) P^0_{\mu\nu}(i\omega) \Phi_\nu(\mathbf{r}'). \tag{4.6}$$

Eq. 4.6 is an approximation because of the use of a truncated basis set. The frequency dependent coefficients $P^0_{\mu\nu}(i\omega)$ are calculated by solving the linear system:

$$P^0_{\mu\nu}(i\omega) = -4\mathrm{Re}\sum_v \langle\phi_v\Phi_\mu|\hat{P}_c\left[\hat{H}_0 - \epsilon_v + i\omega\right]^{-1}\hat{P}_c|\Phi_\nu\phi_v\rangle. \tag{4.7}$$

Here we have introduced the projector on to the conduction manifold:

$$\hat{P}_c = \sum_c |\phi_c\rangle\langle\phi_c|. \tag{4.8}$$

We will also at this stage introduce the closure relation:

$$\hat{P}_v + \hat{P}_c = 1, \tag{4.9}$$

where $\hat{P}_v$ is defined as:

$$\hat{P}_v = \sum_{n \in occ} |\phi_n\rangle\langle\phi_n|. \tag{4.10}$$

In practice Eq. 4.7 is solved using the Lanczos chain methods [82], described in Ref. [83], and employing an additional auxiliary basis set.

Having constructed the polarizability in the optimal basis, matrix elements of the single particle states with the self-energy operator are then calculated. At this stage the irreducible polarizability is introduced:

$$\Pi_0(i\omega) = \frac{\hat{P}_0(i\omega)}{1 - \hat{P}_0(i\omega) \cdot v}, \tag{4.11}$$

where the dot indicates a matrix product:

$$P_0 \cdot v = \int P_0(\mathbf{r}, \mathbf{r}''; i\omega) v(\mathbf{r}'', \mathbf{r}') d\mathbf{r}''. \tag{4.12}$$

The irreducible polarizability is represented using the same optimal basis as the polarizability. The projection of the single particle states onto the correlation part of the self-energy are now calculated for imaginary time arguments:

$$\langle\phi_n|\Sigma_c(i\tau)|\phi_n\rangle = -\frac{1}{2\pi} \sum_{\mu\nu j} f_j e^{i\omega_j \tau} \langle\phi_n(v \cdot \Phi_\nu)|G_0(i\omega_j)|(v \cdot \Phi_\mu)\phi_n\rangle \Pi_{\mu\nu}(i\tau), \tag{4.13}$$

where:

$$G_0(i\omega_j) = [\hat{H}_0 - i\omega_j]^{-1}. \tag{4.14}$$

Eq. 4.13 has the same form as 4.7 and is solved using the same technique of tridiagonalizing the matrix at $i\omega = 0$ and then obtaining the full frequency dependence using Lanczos chains. The projections $\langle\phi_n|\Sigma_c(i\tau)|\phi_n\rangle$ are obtained along a set of imaginary times $i\tau$, and then Fourier transformed to frequency space and analytically continued to the real axis.

There are two particular limitations to the GWL method. While the sum-

over-states is eliminated the convergence of the polarizability now depends on three different parameters: the energy cutoff for replacing conduction states with orthogonalized planewaves, the threshold for the singular value decomposition used to select the eigenvectors of the static polarizability, and the number of conduction states used to construct the Lanczos basis. The second limitation of the method is the formalism applies only to systems at the Γ point. This implies that to treat extended systems accurately large supercells are required. The advantages are a significant reduction in the size of the polarizability basis, and a direct and efficient method for generating the frequency dependence of the operators along the imaginary axis.

2 The *GW* with Spectral Decomposition Method

The *GW* with spectral decomposition (*GW*SD) method, as described in Ref. [84], has developed in two series of papers. The inital work focused on obtaining the dielectric matrix using an iterative technique [85–87]. The full extension to using the dielectric matrix for performing G_0W_0 calculations was then made in Ref. [84] and Ref. [88].

The *GW*SD shares some similarities with the *GWL* technique. The main difference is that the most significant eigenvectors of the static dielectric matrix are calculated using an iterative method rather than via a singular value decomposition.

In *GW*SD all calculations of the dielectric matrix are performed on the symmetrized, static, dielectric matrix:

$$\tilde{\varepsilon}_{\mathbf{GG'}}(\mathbf{q}) = \frac{|\mathbf{q}+\mathbf{G}|}{|\mathbf{q}+\mathbf{G'}|}\varepsilon_{\mathbf{GG'}}(\mathbf{q}). \tag{4.15}$$

By working with the symmetrized version of the dielectric matrix, which is Hermitian, it can be guaranteed all the eigenvectors of the matrix are orthogonal.

Instead of obtaining the eigenvalues of Eq. 4.15, as in the *GWL* method, the

*GW*SD uses an orthogonal iteration procedure [89], to obtain a representation of the dielectric matrix in terms of the eigenvalues, λ_i, and eigenvectors Φ_i:

$$\tilde{\varepsilon}^{-1}(\mathbf{r},\mathbf{r}') = \sum_{i}^{N_{\text{eig}}} (\lambda_i^{-1} - 1)\Phi_i(\mathbf{r})\Phi_i^*(\mathbf{r}'). \tag{4.16}$$

The procedure is as follows. A set of orthogonal trial potentials are selected. The dielectric matrix is applied to the trial potentials via an operation which we will describe shortly. The application of the dielectric matrix to the trial potentials is followed by a step where the new vectors are orthogonalized to each other. This procedure is repeated until the the dielectric eigenvectors and eigenvalues are obtained.

In practice the application of the dielectric matrix to a trial potential is performed indirectly. The action of the dielectric matrix on a trial potential, denoted ΔV_{tr}, can be calculated via:

$$(\tilde{\varepsilon} - 1)\Delta V_{\text{tr}}(\mathbf{r}) = -v_c \Delta n(\mathbf{r}), \tag{4.17}$$

where v_c is the Coulomb potential. The variation in the charge density is given by:

$$\Delta n(\mathbf{r}) = 4\text{Re} \sum_{n \in \text{occ}} \phi_n(\mathbf{r}) \Delta\phi_n^*(\mathbf{r}). \tag{4.18}$$

The variations $\Delta\phi_v$, with the index v denoting a valence state, are obtained by solving the Sternheimer equation [90]:

$$(\hat{H} + \alpha\hat{P}_v - \epsilon_v)|\phi_v\rangle = -P_c \Delta V_{\text{tr}}|\phi_v\rangle, \tag{4.19}$$

where $\alpha\hat{P}_v$ is a scalar times the projection operator of the occupied manifold. This is introduced to prevent the linear system in Eq. 4.19 from becoming singular Ref. [91]. Eq. 4.19 will be discussed at length in the next chapter. Efficient techniques for calculating $\Delta n(\mathbf{r})$ via Eq. 4.19 have been reviewed in Ref. [91].

The initial trial potentials are any set of mutually orthogonal potentials with the stipulation that none of the trial potentials is orthogonal to any of the first N_{eig} eigenvectors of the system. At the end of the procedure the initial trial potentials will have converged to the dielectric eigenvectors Φ_i. The effectiveness of the truncation at N_{eig} number of eigenvectors is determined by the rate at which the eigenvalues λ_i approach 1 in Eq. 4.16.

In this approach the number of eigenvectors used to construct the dielectric matrix becomes the essential convergence parameter. Upon obtaining a basis for the static dielectric matrix, the self energy, can be obtained in the same manner as in the GWL method with some minor differences. In fact the self energy is given by:

$$\langle\phi_n|\hat{\Sigma}_c(i\omega)|\phi_n\rangle = \frac{1}{2\pi}\sum_{ij}^{N_{\text{eig}}}\int d\omega' c_{ij}(i\omega')\langle\phi_n(v_c^{\frac{1}{2}}\Phi_i)|\left[\hat{H} - i(\omega-\omega')\right]^{-1}|\phi_n(v_c^{\frac{1}{2}}\Phi_j)\rangle, \tag{4.20}$$

where the vectors $|\phi_n(v_c^{1/2}\Phi_j)\rangle$ have the coordinate representation:

$$\langle\mathbf{r}|\phi_n(v_c^{1/2}\Phi_j)\rangle = \phi_n(\mathbf{r})\int d\mathbf{r}' v_c(\mathbf{r},\mathbf{r}')^{1/2}\Phi_j(\mathbf{r}'). \tag{4.21}$$

The coefficients $c_{ij}(i\omega)$, of the frequency dependent polarizability are given by:

$$c_{ij}(i\omega) = 2\sum_v\left[\langle(\phi_v(v_c^{\frac{1}{2}})\Phi_i)|\hat{P}_c\left[\hat{H} - \epsilon_v \pm i\omega\right]^{-1}\hat{P}_c|\phi_v(v_c^{\frac{1}{2}})\Phi_j\rangle\right], \tag{4.22}$$

again employing the Lanczos chain technique. The advantages of the GWSD technique are that it completely eliminates the need for unoccupied states from the construction of the polarizability, and eliminating the need for a plasmon-pole model. The disadvantage seems to be limited to performing an analytic continuation of the self-energy to obtain the quasiparticle corrections.

3 Effective Energy Technique

The Effective Energy Technique (EET) has been developed in Refs. [92–96]. The method has been applied to the study of crystalline Si, Ar, ZnO, and SnO_2 as well as the organic molecule rubrene. In all cases the technique was found to accelerate convergence to the obtained by performing the full sum-over-states[94].

For a detailed derivation and discussion of the equations defining the effective energy technique we refer to Refs. [93–95]. Briefly the sum over the entire conduction manifold is replaced by a single effective energy. This can be accomplished by using the closure relation to eliminate the unoccupied states appearing in Eq. 3.4, and then working out a series of commutator relations to define the effective energy in the denominator.

The primary limitation of the method is that the accuracy can only be tested by direct comparison with a sum-over-states calculation. However the accuracy of the EET has been benchmarked over a wide range of systems and can accurately reproduce the results of a sum over states calculation. The technique is easily implemented within a planewave pseudopotential code, and can, therefore, be exploited to improve the efficiency of routines reliant on G_0W_0 calculations, for instance the COHSEX+G_0W_0 calculations performed in Ref. [93].

4 Self-Consistency and the GW approximation

The philosophy underpinning practical G_0W_0 calculations is that one can obtain a reasonable description of the electronic ground state in terms of non-interacting single particle orbitals obtained from a DFT calculation [36]. The G_0W_0 corrections to the ground state wavefunctions and energies, can then be evaluated perturbatively, as demonstrated in Eq. 3.39.

It can be argued that the smaller the first order correction to the energy, the more accurately the Kohn-Sham states describe the interacting physical system. In some cases the LDA is insufficient to obtain a suitably accurate initial approxi-

mation to the ground state eigenvectors and eigenvalues. Transition metal oxides are a good example. Calculations including an Hubbard U-parameter [97, 98], which accounts explicitly for the large electron correlation due to the d electrons present in these systems are often necessary to obtain a satisfactory description of the ground state. *GW* corrections based on LDA+U calculations have been discussed in Refs. [41, 43, 98, 99]. Similarly, hybrid functionals using DFT and a certain fraction of exact exchange, for instance Refs. [24, 25], have been employed as a basis for *GW* calculations. These approaches seek to obtain "the best" possible description of the ground state by going beyond the LDA to the exchange and correlation functional and then perform a G_0W_0 calculation.

Perturbative *GW* calculations maintain some notable deficiencies: the quasiparticle corrections are dependent on the ground state calculation, ground-state properties are inaccessible, the initial dielectric screening may be inappropriate, and particle conservation is violated [100]. Correcting these deficiencies requires moving beyond perturbative corrections by introducing some form of self-consistency. In Ref. [36] an approximate form of self-consistency is proposed whereby the eigenvalues of the Green's function and the polarizability are updated with the real part of the self-energy from the initial calculation. While this improves agreement with experiment, in some cases, it does not fully eliminate the aforementioned deficiencies.

The numerical workload of a full iterative solution to Hedin's equations means certain approximate self-consistent schemes have been investigated. In Refs. [65, 101] a self-consistent *GW* procedure, based on a symmetrized version of the self-energy operator was introduced. This approach mitigates the workload of a full self-consistent calculation by constructing a Hermitian self-energy operator. The scheme has been applied to a number of different real materials [102–104].

Work has also been done to obtain a full iterative solution to Hedin's equations. In this case the full interacting Green's function is updated using the

calculated self-energy at each iteration. The complexity of the numerical enterprise required to perform these calculations is such that only a few fully self-consistent *ab initio* calculations exist for real materials: in the case of solids we refer to Refs. [105, 106], and for atoms and molecules Refs. [100, 107, 108]. The latter calculations convincingly eliminate many of the deficiencies of the G_0W_0 approximation.

5 Scaling considerations

In the final section of this chapter we discuss the reported scaling of the standard sum-over-states expression and the alternative methods for performing *GW* calculations.

The work load in the sum over states approach scales as $N_{\mathrm{pw}}^2 N_{\mathrm{c}} N_{\mathrm{v}}$ where N_{v} is the number of valence states, N_{c} is the number of conduction states, and N_{pw} is the number of planewaves used to describe the system. Each of the quantities N_{pw}, N_{c}, and N_{v}, scales linearly with N the number of atoms in the system. Therefore, the total scaling of the sum over states approach is N^4.

The *GWL* method also scales as N^4, although the optimal basis set reduces the prefactor and memory requirements as compared to the sum-over-states methods.

In the *GW*SD method the solution of Eq. 4.19 scales as $N_{\mathrm{pw}} N_{\mathrm{v}}^2$, and must be performed N_{eig} times. The spectral decomposition therefore scales as $N_{\mathrm{eig}} N_{\mathrm{pw}} N_{\mathrm{v}}^2$, see Ref. [86], which is also N^4 scaling. The advantage over sum-over-states comes by avoiding the inversion of the dielectric matrix via a direct calculation of the eigenvectors, and by avoiding the need to store and calculate a large number of conduction states. It is also possible to reduce the number of times the operator $\tilde{\epsilon} - I$ is applied to the trial potentials by selecting the trial potentials to be approximate eigenvectors. Approximate eigenvectors can be found quickly by using looser convergence criteria and then performing a more refined calculation.

The EET method scales again as N^4 see Refs. [93, 94].

6 Conclusion

In this chapter we have discussed the basic theory underlying alternative approaches to *GW* calculations. All these methods seek to reduce or eliminate the need for a sum-over-states expansion in the construction of the polarizability and the self-energy. The direct methods, *GWL* and *GW*SD, follow similar routes, i.e. the introduction of a truncated basis set to describe the dielectric matrix and the solution of a linear system of equations to obtain the expansion coefficients. Both methods exploit the Lanczos technique to generate the frequency dependence of the Green's function and polarizability.

In the case of the EET the expressions for the Green's function and the polarizability are transformed so that the whole sum-over-states replaced by a single energy.

We have discussed the reported scaling of the various methods discussed, and compared them to the original sum-over-states formulation.

In addition to the alternative methods for performing *GW* calculations we have also briefly discussed work which has moved beyond a single iteration of Hedin's equations and perturbation theory. These efforts include systematic variation of the starting Hamiltonian i.e. LDA+U and hybrid exchange schemes. Reference was also made to work reporting fully self-consistent *GW* calculations. These topics have been introduced here to provide context for the Sternheimer-*GW* method which will be discussed in the remaining chapters.

5 Theory and Implementation of the Sternheimer-GW Approach

In this chapter we discuss the formalism for performing Sternheimer-GW calculations. In Ref. [54] the Sternheimer-GW approach was first demonstrated using a proof-of-concept pilot implementation. This proof of concept was built on top of the *empirical* pseudopotential method introduced in Ref. [109]. The major focus of this thesis has been the development and extension of the Sternheimer-GW method presented in Ref. [54] to a fully *ab initio* pseudopotential framework based on a planewaves basis.

The theoretical approach to performing GW calculations has been implemented building on routines from the electronic structure package Quantum Espresso [110]. The current implementation exploits the symmetry operations of the crystal space group and the optimized implementation of efficient techniques for solving linear systems of equations.

The organisation of this chapter is as follows: the first Section provides a brief synopsis of the history and applications of the Sternheimer equation. In Section 2 we present a general formulation. In Section 3 we specialize the treatment to a planewaves basis. In Section 4 we discuss the use of crystal symmetry to reduce the computational workload of the method. Finally in Section 5 we discuss the description of the frequency dependence of the operators arising in the GW formalism and some technical details of the implementation.

1 The Sternheimer equation

The Sternheimer equation was first employed in Ref. [90] for calculating the electronic polarizability of ions. In that work the first order variations of the

electronic wave functions, $\Delta\psi_n(\mathbf{r})$, due to a perturbation by an external electric potential, $\Delta V(\mathbf{r})$, were obtained via the direct solution of the following equation:

$$(\hat{H} - \varepsilon_n)\Delta\psi_n(\mathbf{r}) = -\hat{P}_c\Delta V(\mathbf{r})\psi_n(\mathbf{r}). \tag{5.1}$$

Eq. 5.1 is derived via standard first order perturbation theory, see Ref. [91] for a brief derivation, and in the electronic structure community is often referred to as the Sternheimer equation.

The Sternheimer equation allows a variety of a material's response properties to be calculated. The perturbation ΔV in Eq. 5.1 is not limited to an electric field potential. ΔV can also take the form of an ionic displacement which allows one to calculate phonon dispersion relations. In this context, the Sternheimer equation has been extensively discussed in Ref. [91] and Ref. [111]. By setting ΔV to an external magnetic field, or the magnetic field produced by a nucleus, the use of the first order response equations of the Sternheimer type has been employed in Ref. [112] and Ref. [113] to obtain nuclear magnetic resonance (NMR) chemical shifts and NMR J-coupling constants.

The Sternheimer equation provides a means for obtaining the response properties of an electronic system via the direct solution of a linear system of equations. In the Sternheimer-GW method we exploit the Sternheimer equation to calculate the electronic response of a material to Coulombic perturbations. An analogous system of equations can be formulated to obtain the Green's function. It is the central role that the Sternheimer equation takes in our approach which motivates terming the overall approach Sternheimer-GW.

2 Real-space formulation

In this section we provide the general formulation of the Sternheimer-GW approach. We will have occasion to refer to many of the equations discussed in Chapter 2, and we will reproduce some of those here when convenient.

The goal of a GW calculation is to construct the self-energy Σ given in terms of the Green's function G and the screened Coulomb interaction W by:

$$\Sigma(\mathbf{r},\mathbf{r}';\omega) = \frac{i}{2\pi}\int_{-\infty}^{\infty} G(\mathbf{r},\mathbf{r}';\omega+\omega')W(\mathbf{r},\mathbf{r}';\omega')\mathrm{e}^{-i\eta\omega'}d\omega'. \tag{5.2}$$

As noted in Chapters 3 and 4 the construction of the Green's function and the screened Coulomb interaction both involve a sum over the conduction state manifold. In the Sternheimer-GW approach these summations are fully eliminated and are replaced by the solution of linear systems of equations.

Due to the multivariable nature of both the Green's function and the screened Coulomb interaction, it will often be convenient to write them as functions in $\mathbf{r}'$ parametric in the variables $[\mathbf{r},\omega]$:

$$G(\mathbf{r},\mathbf{r}',\omega) = G_{[\mathbf{r},\omega]}(\mathbf{r}'), \tag{5.3}$$

and

$$W(\mathbf{r},\mathbf{r}',\omega) = W_{[\mathbf{r},\omega]}(\mathbf{r}'). \tag{5.4}$$

This provides a more compact notation when we discuss the equations arising in the Sternheimer-GW formalism. We will also employ an additional short-hand notation in writing equations, e.g.:

$$W_{[\mathbf{r},\omega]}(\mathbf{r}')\psi_n(\mathbf{r}') = W_{[\mathbf{r},\omega]}\psi_n, \tag{5.5}$$

where the $\mathbf{r}'$ is implied on the right hand side. In general the omitted variables will be clear from the context.

2.1 Screened Coulomb interaction

The use of the Sternheimer equation for calculating elements of the dielectric matrix was demonstrated for the first time in Ref. [114]. Earlier attempts along

the same lines involved non-perturbative calculations using supercells Ref. [115]. The desirable features of a direct calculation were also highlighted in Ref. [116] but the numerical workload exceeded computational capacity at the time.

In the Sternheimer approach the screened Coulomb interaction is obtained by solving, for each occupied state ψ_v, the following two Sternheimer equations:

$$(\hat{H} - \varepsilon_v \pm \omega)\Delta\psi^{\pm}_{v[\mathbf{r},\omega]}(\mathbf{r}') = -(1 - \hat{P}_{\text{occ}})\Delta V_{[\mathbf{r},\omega]}(\mathbf{r}')\psi_v(\mathbf{r}'), \tag{5.6}$$

the choice of sign $\pm$ corresponding to the positive and negative frequency components of the frequency response, and the sum over unoccupied states has been eliminated using the closure relation (Eq. 4.9.

Here $\hat{P}_{\text{occ}}$ is the projection operator onto the manifold of occupied states, and $\Delta\psi^{\pm}_{v[\mathbf{r},\omega]}$ are the variations of the single-particle wavefunctions corresponding to the perturbation $\Delta V_{[\mathbf{r},\omega]}$. The perturbation can be considered as the Coulomb potential due to a point charge located at the position $\mathbf{r}$ and varying in time with frequency ω. From the variation of the electronic wave functions the first order change of the density can be calculated as:

$$\Delta n_{[\mathbf{r},\omega]}(\mathbf{r}') = 2\sum_v \psi^*_v(\mathbf{r}') \left(\Delta\psi^{+}_{v[\mathbf{r},\omega]}(\mathbf{r}') + \Delta\psi^{-}_{v[\mathbf{r},\omega]}(\mathbf{r}')\right). \tag{5.7}$$

The variation in the charge density in turn produces an induced Hartree potential:

$$\Delta V^{\text{H}}_{[\mathbf{r},\omega]} = \int \Delta n_{[\mathbf{r},\omega]}(\mathbf{r}'')v(\mathbf{r}'',\mathbf{r}')d\mathbf{r}''. \tag{5.8}$$

In order to proceed we need to demonstrate how the first order variations in the charge density can be used to construct the screened Coulomb interaction.

There are two different routes to the construction of the screened Coulomb interaction depending on the choice of $\Delta V_{[\mathbf{r},\omega]}(\mathbf{r}')$. In the first case the perturbation is chosen to be the bare Coulomb interaction and the variation in the charge density is calculated directly. This process is called the "non self-consistent Stern-

heimer approach" and allows one to calculate the dielectric matrix of the material. In the second case the perturbation is chosen to be the screened Coulomb interaction itself. This requires a self-consistent process and allows for the direct construction of the screened Coulomb interaction. We refer to this procedure as the "self-consistent Sternheimer approach". We will now derive the connection between the formal definitions of the dielectric matrix and screened Coulomb interaction and the first order variation in the electronic density.

Non Self-Consistent Sternheimer

In the non-self-consistent approach we can directly calculate the dielectric matrix. This is accomplished by introducing a point charge perturbation located at $\mathbf{r}$. This perturbation produces the bare Coulomb potential: $v(\mathbf{r}, \mathbf{r}')$. We set the perturbing potential $\Delta V_{[\mathbf{r},\omega]}(\mathbf{r}') = v_{[\mathbf{r}]}(\mathbf{r}')$ and wish to demonstrate that the first order variation of the density yields the dielectric matrix:

$$\epsilon(\mathbf{r}, \mathbf{r}', \omega) = \delta(\mathbf{r}, \mathbf{r}') - \Delta n_{[\mathbf{r},\omega]}(\mathbf{r}'). \tag{5.9}$$

The proof of this is as follows. We refer to Chapter 2, Section 4.1, where the dielectric matrix was defined as Eq. 2.49:

$$\epsilon(\mathbf{r}, t, \mathbf{r}', t') = \delta(\mathbf{r} - \mathbf{r}')\delta(t - t') - \int v(\mathbf{r}, \mathbf{r}'')P(\mathbf{r}'', t, \mathbf{r}', t')d\mathbf{r}''. \tag{5.10}$$

If we perform a Fourier transform to the frequency domain and rewrite the polarizability using its representation as a sum over states, given by Eq. 3.4, we obtain:

$$\epsilon(\mathbf{r}, \mathbf{r}'; \omega) = \delta(\mathbf{r} - \mathbf{r}') - 2\int v(\mathbf{r}, \mathbf{r}'') \sum_{nm} \frac{(f_n - f_m)\psi_m^*(\mathbf{r}'')\psi_n(\mathbf{r}'')\psi_m(\mathbf{r}')\psi_n^*(\mathbf{r}')d\mathbf{r}''}{\epsilon_n - \epsilon_m \pm \omega + i\eta}. \tag{5.11}$$

We rewrite Eq. 5.11 as:

$$\epsilon(\mathbf{r},\mathbf{r}';\omega) = \delta(\mathbf{r}-\mathbf{r}') - 4\sum_{n\in\mathrm{occ},m} \psi_n^*(\mathbf{r}')\frac{(f_n - f_m)\langle\psi_m|\Delta V_{[\mathbf{r},\omega]}|\psi_n\rangle}{\epsilon_n - \epsilon_m \pm \omega + i\eta}\psi_m(\mathbf{r}'), \quad (5.12)$$

where $\langle\psi_m|\Delta V_{[\mathbf{r},\omega]}|\psi_n\rangle$ is a matrix element with the integral over $\mathbf{r}''$. We restricted n to the occupied states and let m run over the entire manifold since the factors f_n and f_m couple only occupied and unoccupied states. Each of these pairs occurs twice which gives rise to the extra factor of two. Now we can define the quantity:

$$\Delta\psi_n^{\pm} = \sum_m \frac{\langle\psi_m|\Delta V_{[\mathbf{r},\omega]}|\psi_n\rangle}{\epsilon_n - \epsilon_m \pm \omega + i\eta}\psi_m. \quad (5.13)$$

This is precisely the formal solution of the Sternheimer equation, Eq. 5.6.

Having identified the first order variations in the wave functions we can use Eq. 5.7 to rewrite Eq. 5.12 as:

$$\epsilon(\mathbf{r},\mathbf{r}',\omega) = \delta(\mathbf{r},\mathbf{r}') - \Delta n_{[\mathbf{r},\omega]}(\mathbf{r}'), \quad (5.14)$$

as required. The direct approach to calculating the dielectric matrix has an intuitive physical interpretation: the electrons in the system respond to the perturbing charge by rearranging themselves according to the RPA polarizability of the system.

To obtain the screened Coulomb interaction, the dielectric matrix $\epsilon(\mathbf{r},\mathbf{r}';\omega)$ must first be inverted at each frequency. This matrix inversion scales as N^3 and is performed according to the standard procedure described in Refs. [36, 117, 118].

Self-Consistent Sternheimer Calculation

It is also possible to obtain the screened Coulomb interaction via a self-consistent solution of the Sternheimer equation.

To derive the self-consistent Sternheimer technique it is best to start from the definition of the screened Coulomb interaction, Eq. 2.47, in terms of the Dyson

equation:

$$W(\mathbf{r},t,\mathbf{r}',t') = v(\mathbf{r},\mathbf{r}') + \int d\mathbf{r}'''v(\mathbf{r},\mathbf{r}''') \int P(\mathbf{r}''',t,\mathbf{r}'',t'')W(\mathbf{r}'',t'',\mathbf{r}',t')dt''d\mathbf{r}''. \tag{5.15}$$

We now follow a similar procedure to the direct case. We transform Eq. 5.15 to the frequency domain and using the sum-over-states representation of the polarizability we arrive at:

$$W(\mathbf{r},\mathbf{r}';\omega) = v(\mathbf{r},\mathbf{r}') + 2\int d\mathbf{r}^{'''}v(\mathbf{r},\mathbf{r}''')\sum_{nm}\psi_n^*(\mathbf{r}')\frac{\langle\psi_m|W_{[\mathbf{r}''',\omega]}|\psi_n\rangle}{\epsilon_n - \epsilon_m \pm \omega}\psi_m(\mathbf{r}'). \tag{5.16}$$

Again the quantity under the summation is equivalent to the $\Delta n_{[\mathbf{r},\omega]}$ calculated by solving the Sternheimer equation via Eq. 5.6 and Eq. 5.7. In this case the perturbing potential is chosen to be the screened Coulomb interaction: $\Delta V_{[\mathbf{r},\omega]}(\mathbf{r}') = W_{[\mathbf{r},\omega]}(\mathbf{r}')$.

Clearly the screened Coulomb interaction is not initially known; it must be obtained via an iterative solution of the Dyson equation. This self-consistent procedure is facilitated by denoting the input perturbing potential as $\Delta V^{\text{in}}_{[\mathbf{r},\omega]}$, and the output potential as $\Delta V^{\text{out}}_{[\mathbf{r},\omega]}$. Initially the perturbing potential in the Sternheimer equation is set to the bare interaction $\Delta V^{\text{in}}_{[\mathbf{r},\omega]}(\mathbf{r}') = v_{[\mathbf{r}]}(\mathbf{r}')$. The variation of the density yields the output Hartree potential, which screens the bare Coulomb interaction:

$$\Delta V^{\text{out}}_{[\mathbf{r},\omega]} = v(\mathbf{r},\mathbf{r}') + \int d\mathbf{r}''\Delta n_{[\mathbf{r},\omega]}(\mathbf{r}'')v(\mathbf{r}'',\mathbf{r}'). \tag{5.17}$$

It could also be noted at this stage that effects beyond the RPA screening, can be incorporated by including the exchange-correlation potential as part of the response potential, Ref. [36]:

$$\Delta V^{\text{out}}_{[\mathbf{r},\omega]} = v(\mathbf{r},\mathbf{r}') + \int d\mathbf{r}''\Delta n_{[\mathbf{r},\omega]}(\mathbf{r}'')v(\mathbf{r}'',\mathbf{r}') + \frac{\delta V_{xc}(\mathbf{r})}{\delta n(\mathbf{r})}\Delta n(\mathbf{r}). \tag{5.18}$$

This possibility was studied in Ref. [119] and Sternheimer-*GW* calculations performed with this "RPA+V^{xc}" screening are presented in the next chapter. $\Delta V^{\mathrm{out}}_{[\mathbf{r},\omega]}$ is then combined with $\Delta V^{\mathrm{in}}_{[\mathbf{r},\omega]}$ according to some mixing technique and used as the next $\Delta V^{\mathrm{in}}_{[\mathbf{r},\omega]}$ perturbation in the Sternheimer equation.

We have investigated two schemes to expedite this self-consistency process. The most successful has been Broyden's method for potential mixing, described in Ref. [120]. This scheme has been generalized to deal with complex potentials in Ref. [54]. We also investigated a second mixing scheme based on a model dielectric response function. This scheme followed the work of Ref. [121] but was found to be less effective than Broyden's method.

This iterative procedure is continued until the relative change in the input and output potential is below a user defined threshold, which implies that the self-consistent solution of Eq. 5.15 has been found.

In both cases, self-consistent and non self-consistent, the Sternheimer approach to calculating the screened Coulomb interaction has an intuitive physical meaning. A test charge is introduced at the point $\mathbf{r}$ and the frequency dependent rearrangement of the electronic charge density is calculated.

The choice between the self-consistent Sternheimer scheme and the non self-consistent scheme depends on the system under consideration. The inversion of the dielectric matrix is very fast for small systems, and in these cases the non self-consistent scheme is advantageous. In the case of large systems where memory requirements are important, the self-consistent scheme is preferable. In Chapter 6 we will present results produced using both techniques.

2.2 Green's function

Similar to the construction of the screened Coulomb interaction we would like to construct the Green's function in a way that only requires the calculation of the occupied states. To do this we need to transform the standard expression for the

Green's function:

$$G(\mathbf{r},\mathbf{r}';\omega) = \sum_n \frac{\phi_n(\mathbf{r})\phi_n^*(\mathbf{r}')}{\omega - \epsilon_n \pm i\eta}. \tag{5.19}$$

We rewrite Eq. 5.19 as the sum of a function G^{A} which is analytic in the upper half of the complex plane, and a non-analytic part G^{N} which is composed of the singularities contributed by the manifold of occupied states. By adding and subtracting a sum over only the occupied states we proceed as in Ref. [54]:

$$G(\mathbf{r},\mathbf{r}';\omega) = \sum_n \frac{\phi_n(\mathbf{r})\phi_n^*(\mathbf{r}')}{\omega - \epsilon_n \pm i\eta} \pm \sum_v \frac{\phi_v(\mathbf{r})\phi_v^*(\mathbf{r}')}{\omega - \epsilon_v + i\eta}. \tag{5.20}$$

By clearing fractions Eq. 5.20 is rearranged in terms of the analytic part G^A, and the non-analytic component G^N:

$$G(\mathbf{r},\mathbf{r}';\omega) = G^{\mathrm{A}}(\mathbf{r},\mathbf{r}';\omega) + G^{\mathrm{N}}(\mathbf{r},\mathbf{r}';\omega). \tag{5.21}$$

The explicit expressions of these functions in terms of single-particle states $\phi_n(\mathbf{r})$ with eigenvalues ε_n are:

$$G^{\mathrm{A}}(\mathbf{r},\mathbf{r}';\omega) = \sum_n \frac{\phi_n(\mathbf{r})\phi_n^*(\mathbf{r}')}{\omega - \varepsilon_n + i\eta}, \tag{5.22}$$

$$G^{\mathrm{N}}(\mathbf{r},\mathbf{r}';\omega) = 2\pi i \sum_v \delta(\omega - \varepsilon_v)\phi_v(\mathbf{r})\phi_v^*(\mathbf{r}'). \tag{5.23}$$

The latter sum is restricted to occupied single-particle states ϕ_v of energy ε_v, and the functions $\delta(\omega - \varepsilon_v)$ are Dirac's deltas. This partition allows us to eliminate the sum over conduction states in the construction of the Green's function. The G^{N} component is expanded in terms of occupied states and the G^A component can be calculated in the following way.

We apply $(\hat{H} - \omega - i\eta)$ to both sides of Eq. 5.22, to obtain:

$$(\hat{H} - \omega - i\eta)G^{\mathrm{A}}_{[\mathbf{r},\omega]} = \sum_n \frac{\phi_n(\mathbf{r})\left[H - \omega - i\eta\right]\phi_n}{\omega - \varepsilon_n + i\eta}, \tag{5.24}$$

which simplifies to:

$$(\hat{H} - \omega - i\eta)G^{\mathrm{A}}_{[\mathbf{r},\omega]} = -\delta_{[\mathbf{r}]}, \tag{5.25}$$

where $\delta_{[\mathbf{r}]}(\mathbf{r}')$ is a Dirac delta centered at the position $\mathbf{r}$ and is obtained from the completeness of the wavefunctions:

$$\sum_n \phi_n(\mathbf{r})\phi_n^*(\mathbf{r}') = \delta_{[\mathbf{r}]}(\mathbf{r}'). \tag{5.26}$$

The analytic component of the Green's function can now be obtained by solving a linear system, similar to the construction of the screened Coulomb interaction.

3 Reciprocal-space formulation

In this section we describe the equations for the Sternheimer-*GW* method specialized to a planewaves basis set. An alternative formulation based on local orbitals has also been presented in Ref. [122] and Ref. [123]. The motivation for a full implementation in a planewaves basis are (i) the possibility of controlling the numerical accuracy of the calculations using a single parameter, i.e. the kinetic energy cutoff, and (ii) the availability of many established electronic structure codes based on planewaves. In addition the planewaves basis set provides an effective basis for describing delocalized states.

3.1 Screened Coulomb interaction

In Chapter 3 the single particle wave function in a planewaves basis was introduced:

$$\phi_{n\mathbf{k}}(\mathbf{r}) = \frac{1}{\sqrt{\Omega}} \sum_{\mathbf{G}} u_{n\mathbf{k}}(\mathbf{G}) e^{i(\mathbf{k}+\mathbf{G})\cdot\mathbf{r}}. \tag{5.27}$$

The first order linear variation of the occupied eigenfunctions appearing in Eq. 5.6 are functions of $\mathbf{r}, \mathbf{r}'$ and ω, and have a more complicated expression:

$$\Delta\phi^{\pm}_{v\mathbf{k}[\mathbf{r},\omega]}(\mathbf{r}') = \frac{1}{N_{\mathbf{q}}\Omega} \sum_{\mathbf{q}\mathbf{G}\mathbf{G}'} \mathrm{e}^{-i(\mathbf{q}+\mathbf{G})\cdot\mathbf{r}} \mathrm{e}^{i(\mathbf{k}+\mathbf{q}+\mathbf{G}')\cdot\mathbf{r}'} \Delta u^{\pm}_{v\mathbf{k}[\mathbf{q},\mathbf{G},\omega]}(\mathbf{G}').$$

Here the appearance of the Bloch wavevectors $\mathbf{k}$ and $\mathbf{k}+\mathbf{q}$ in the exponentials is a consequence of the conservation of crystal momentum in the Sternheimer equation [91], [54]. The reciprocal space counterpart of Eq. 5.6 for the variation of the wavefunctions induced by the Coulomb interaction is:

$$(\hat{H}_{\mathbf{k}+\mathbf{q}} - \varepsilon_{v\mathbf{k}} \pm \omega)\Delta u^{\pm}_{v\mathbf{k}[\mathbf{q},\mathbf{G},\omega]} = -(1 - \hat{P}^{\mathbf{k}+\mathbf{q}})\Delta v_{[\mathbf{q},\mathbf{G},\omega]} u_{v\mathbf{k}}, \tag{5.28}$$

where $\hat{H}_{\mathbf{k}}$ indicates the $\mathbf{k}$-projected single-particle Hamiltonian, $\hat{P}^{\mathbf{k}+\mathbf{q}}_{\text{occ}}$ is the projector over the occupied states with Bloch wavevector $\mathbf{k}+\mathbf{q}$. This equation is solved for each $\mathbf{k}$, $\mathbf{q}$, $\mathbf{G}$, and ω using the generalized conjugate-gradient techniques, and multishift solver, discussed in Appendix C. Since the linear operator $\hat{H}_{\mathbf{k}+\mathbf{q}} - \varepsilon_{v\mathbf{k}} \pm \omega$ becomes singular when the excitation energy ω corresponds to transitions between occupied and unoccupied states, we choose to calculate $\Delta u^{\pm}_{v\mathbf{k}[\mathbf{q},\mathbf{G},\omega]}$ along the imaginary axis, and to obtain the real axis solutions by approximate analytic continuation or by means of the Godby-Needs plasmon-pole model introduced in Ref. [46]. These aspects are described in more detail in Sec. 5. Once we have obtained the variations of the wavefunctions from Eq. 5.28 for every $\mathbf{k}$-vector, we can construct the linear change in the density matrix. The reciprocal space counterpart of Eq. 5.7 is:

$$\Delta n_{[\mathbf{q},\mathbf{G},\omega]} = \frac{2}{N_{\mathbf{k}}} \sum_{v\mathbf{k}} u^{*}_{v\mathbf{k}} \left(\Delta u^{+}_{v\mathbf{k}[\mathbf{q},\mathbf{G},\omega]} + \Delta u^{-}_{v\mathbf{k}[\mathbf{q},\mathbf{G},\omega]} \right). \tag{5.29}$$

By using Eq. 5.29 and the definition of the two spatial variable Fourier transform given in Eq. 3.18, it is then straightforward to obtain the reciprocal-space version of Eqs. 5.9-5.17. For instance if a self-consistent density response has been calculated, then the screened Coulomb interaction is easily constructed in reciprocal space:

$$W_{\mathbf{G}\mathbf{G}'}(\mathbf{q},\omega) = \left[\delta_{\mathbf{G}\mathbf{G}'} + \Delta n_{\mathbf{G}\mathbf{G}'}(\mathbf{q},\omega)\right] v(\mathbf{q}+\mathbf{G}), \tag{5.30}$$

and in real space this becomes:

$$W(\mathbf{r},\mathbf{r}';\omega) = \sum_{\mathbf{qGG}'} e^{-i(\mathbf{q}+\mathbf{G})\cdot\mathbf{r}} W_{\mathbf{GG}'}(\mathbf{q},\omega) e^{i(\mathbf{q}+\mathbf{G}')\mathbf{r}'}. \tag{5.31}$$

By calculating the reponse to each planewave $e^{i\mathbf{G}\cdot\mathbf{r}}$, we can construct an entire row of the screened Coulomb interaction.

3.2 Green's function

The counterpart of Eq. 5.25 for the analytic part of the Green's function in reciprocal space is:

$$(\hat{H}_{\mathbf{k}} - \omega - i\eta) g^{\mathrm{A}}_{[\mathbf{k},\mathbf{G},\omega]}(\mathbf{G}') = -\delta_{\mathbf{GG}'}, \tag{5.32}$$

This equation is solved for each $\mathbf{k}$ and $\mathbf{G}$ using standard methods based on conjugate-gradient solvers. The frequency dependence is dealt with using Frommer's multishift method presented in Ref. [124] and described in Sec. 5, and Appendix C, and effectively requires calculations only for one value of ω.

3.3 The self-energy

Eqs. 5.28 and 5.32 are used to calculate the complete Green's function $G_{\mathbf{GG}'}(\mathbf{k},\omega)$ and the complete screened Coulomb interaction $W_{\mathbf{GG}'}(\mathbf{q},\omega)$ in reciprocal space.

Once these quantities have been determined the W and G matrices are represented in reciprocal space. It is possible to calculate the Bloch-periodic part of the GW self-energy $\Sigma_{\mathbf{k}}(\mathbf{r},\mathbf{r}',\omega)$ by performing a Fourier transform of the two quantities into real space, and evaluating the convolution in frequency space:

$$\Sigma_{\mathbf{k}}(\mathbf{r},\mathbf{r}',\omega) = \frac{i}{2\pi}\frac{1}{N_{\mathbf{q}}} \sum_{\mathbf{q}} \int d\omega' \mathrm{e}^{-i\delta\omega'} G_{\mathbf{k}-\mathbf{q}}(\mathbf{r},\mathbf{r}',\omega+\omega') W_{\mathbf{q}}(\mathbf{r},\mathbf{r}',\omega'). \tag{5.33}$$

In practice we split the self-energy into two different parts:

$$\Sigma(\mathbf{r},\mathbf{r}';\omega) = \Sigma^{\mathrm{ex}}(\mathbf{r},\mathbf{r}') + \Sigma^{\mathrm{c}}(\mathbf{r},\mathbf{r}';\omega). \tag{5.34}$$

The exact exchange part is composed of the occupied electronic states:

$$\Sigma^{\mathrm{ex}}(\mathbf{r},\mathbf{r}') = -\sum_{v\mathbf{k}} \phi_{v\mathbf{k}}(\mathbf{r})\phi^{*}_{v\mathbf{k}}(\mathbf{r}')v(\mathbf{r},\mathbf{r}'). \tag{5.35}$$

The correlation energy is given by:

$$\Sigma^{\mathrm{c}}(\mathbf{r},\mathbf{r}';\omega) = \frac{i}{2\pi}\int_{-\omega_c}^{\omega_c} G(\mathbf{r},\mathbf{r}';\omega+\omega')\left[W(\mathbf{r},\mathbf{r}';\omega') - v(\mathbf{r},\mathbf{r}')\right] d\omega', \tag{5.36}$$

where ω_c is the frequency cutoff on the integral.

4 Crystal symmetry

In this section we discuss one aspect of our methodology which is critical for achieving competitive performance: the use of crystal symmetry operations. The use of crystal symmetry operations has been discussed in the context of *GW* calculations based on the sum-over-states approach [116, 125]. Here we generalize their treatment and discuss how to minimize the computational workload of Sternheimer-*GW* calculations by exploiting crystal symmetry.

With reference to Sec. 3 it is possible to significantly reduce the number of $\mathbf{k}$, $\mathbf{q}$, and $\mathbf{G}$ vectors in four places:

1. Eq. 5.28 only needs to be solved for inequivalent $\mathbf{G}$ vectors and $\mathbf{q}$ vectors.
2. Eq. 5.32 only needs to be solved for inequivalent $\mathbf{G}$ vectors and $\mathbf{k}$ vectors.
3. Eq. 5.29 can be restricted to a sum over the irreducible part of the Brillouin zone.
4. In Eq. 5.33 the convolution over the Brillouin zone can be restricted to a subset of $\mathbf{q}$ vectors.

Taken together these symmetry considerations allow us to reduce the number of independent Sternheimer equations that need to be solved.

We here denote a symmetry operation of the crystal following the notation of Ref. [126]:

$$\{\mathcal{S}|\mathbf{v}\}\,\mathbf{r} = \mathcal{S}\mathbf{r} + \mathbf{v}, \tag{5.37}$$

where $\mathcal{S}$ is a rotation and $\mathbf{v}$ is the (possibly) associated fractional translation. We denote by $\mathcal{G}_{\mathbf{q}}$ the small group of $\mathbf{q}$, i.e. the subset of operations which leave this wavevector unchanged modulo a reciprocal lattice vector ($\mathcal{S}\mathbf{q} = \mathbf{q} + \mathbf{G}$).

The self-energy Σ, the Green's function G, and the screened Coulomb interaction W are all invariant under any crystal symmetry operation $\{\mathcal{S}|\mathbf{v}\}$:

$$f\left(\{\mathcal{S}|\mathbf{v}\}\,\mathbf{r}, \{\mathcal{S}|\mathbf{v}\}\,\mathbf{r}'; \omega\right) = f(\mathbf{r}, \mathbf{r}'; \omega), \text{ with } f = \Sigma, G, W. \tag{5.38}$$

By applying this relation to the Fourier expansion in Eq. 3.18 we obtain:

$$f_{[\mathbf{q},\mathbf{G},\omega]}(\mathbf{G}') = f_{[\mathcal{S}\mathbf{q},\mathcal{S}\mathbf{G},\omega]}(\mathcal{S}\mathbf{G}')\mathrm{e}^{i(\mathbf{G}'-\mathbf{G})\cdot\mathbf{v}}. \tag{5.39}$$

If $\mathbf{q}$ belongs to $\mathcal{G}_{\mathbf{q}}$ then we have a recipe for generating the solution $\Delta v_{[\mathbf{q},\mathcal{S}\mathbf{G},\omega]}$ of Eq. 5.28 from the solution $\Delta v_{[\mathbf{q},\mathbf{G},\omega]}$ without explicitly solving the Sternheimer equation for $\mathcal{S}\mathbf{G}$:

$$\Delta v_{[\mathbf{q},\mathcal{S}\mathbf{G},\omega]}(\mathbf{G}') = \mathrm{e}^{-i\mathcal{S}^{-1}(\mathbf{G}'-\mathbf{G})\cdot\mathbf{v}}\Delta v_{[\mathbf{q},\mathbf{G},\omega]}(\mathcal{S}^{-1}\mathbf{G}'). \tag{5.40}$$

This observation implies that we only need to solve the Sternheimer equation for the subset of planewaves which are irreducible with respect to the small group $\mathcal{G}(\mathbf{q})$.

Once the solution $\Delta v_{[\mathbf{q},\mathbf{G},\omega]}(\mathbf{G}')$ has been determined for every $\mathbf{G}, \mathbf{G}'$ and one wavevector $\mathbf{q}$ in the Brillouin zone, we use the symmetries of the full space group of the crystal in order to generate the symmetry-equivalent solutions for all the

other wavevectors belonging to the star of $\mathbf{q}$. The transformation law is again derived from Eq. 5.39 and reads as follows:

$$\Delta v_{[\mathcal{S}\mathbf{q},\mathbf{G},\omega]}(\mathbf{G}') = \mathrm{e}^{-i\mathcal{S}^{-1}(\mathbf{G}'-\mathbf{G})\cdot\mathbf{v}}\Delta v_{[\mathbf{q},\mathcal{S}^{-1}\mathbf{G},\omega]}(\mathcal{S}^{-1}\mathbf{G}'). \tag{5.41}$$

The sum over the wavevectors $\mathbf{k}$ in Eq. 5.29 can be restricted to the wedge of the Brillouin zone which is irreducible with respect to $\mathcal{G}_\mathbf{q}$. In order to show that this is the case, we consider the simplest case of non-degenerate bands and we rewrite the Sternheimer equation, Eq. 5.28, for the wavevector $\mathcal{S}\mathbf{k}$, with $\mathcal{S}$ belonging to $\mathcal{G}_\mathbf{q}$:

$$(\hat{H}_{\mathcal{S}\mathbf{k}+\mathbf{q}} - \varepsilon_{v\mathcal{S}\mathbf{k}} \pm \omega)\Delta u^{\pm}_{v\mathcal{S}\mathbf{k}[\mathbf{q},\mathbf{G},\omega]} = -(1 - \hat{P}^{\mathcal{S}\mathbf{k}+\mathbf{q}}_{\mathrm{occ}})\Delta v_{[\mathbf{q},\mathbf{G},\omega]}u_{v\mathcal{S}\mathbf{k}}. \tag{5.42}$$

If we now observe that $\hat{H}_{\mathcal{S}\mathbf{k}+\mathbf{q}}(\mathbf{r}) = \hat{H}_{\mathbf{k}+\mathbf{q}}(\mathcal{S}^{-1}\mathbf{r})$ and $u_{v\mathcal{S}\mathbf{k}}(\mathcal{S}\mathbf{r}) = u_{v\mathbf{k}}(\mathbf{r})$ we find:

$$[\hat{H}_{\mathbf{k}+\mathbf{q}}(\mathbf{r}) - \varepsilon_{v\mathbf{k}} \pm \omega]\Delta u^{\pm}_{v\mathcal{S}\mathbf{k}[\mathbf{q},\mathbf{G},\omega]}(\mathcal{S}\mathbf{r}) = -[1 - \hat{P}^{\mathbf{k}+\mathbf{q}}_{\mathrm{occ}}(\mathbf{r})]\Delta v_{[\mathbf{q},\mathbf{G},\omega]}u_{v\mathbf{k}}(\mathbf{r}). \tag{5.43}$$

In this last equation the non-locality of the Hamiltonian and of the projector are not displayed for clarity. By comparing Eq. 5.43 with Eq. 5.28 we obtain the transformation law for the variation of the wavefunctions:

$$\Delta u^{\pm}_{v\mathcal{S}\mathbf{k}[\mathbf{q},\mathbf{G},\omega]}(\mathbf{r}) = \Delta u^{\pm}_{v\mathbf{k}[\mathbf{q},\mathbf{G},\omega]}(\mathcal{S}^{-1}\mathbf{r}). \tag{5.44}$$

This result can be employed in Eq. 5.29 in order to reduce the $\mathbf{k}$-vectors to the irreducible wedge of the Brillouin zone for the small group of $\mathbf{q}$. In fact, from Eq. 5.9 we see that the density matrix response $\Delta n_{[\mathbf{r},\omega]}(\mathbf{r}')$ inherits the symmetry properties of the screened Coulomb interaction. In addition, from Eq. 5.44 we know that every term $u^*_{v\mathbf{k}}\Delta u^{+}_{v\mathbf{k}[\mathbf{q},\mathbf{G},\omega]}$ appearing in Eq. 5.29 transforms as the square modulus of the Bloch wavefunction $|u_{v\mathbf{k}}|^2$. By combining these observations together we conclude that the rule for the Brillouin zone reduction is

identical to the case of standard DFT calculations of the electron density, provided the symmetries are restricted to $\mathcal{G}_{\mathbf{q}}$. This is the same rule which applies to density-functional perturbation theory calculations of phonon dispersion relations [91]. Finally, in the case of degenerate eigenvalues this procedure holds unchanged, and the unitary relation between the Bloch wavefunctions $u_{v\mathbf{k}}$ and $u_{v\mathcal{S}\mathbf{k}}$ is traced out in the calculation of the density matrix response.

In the calculation of the Green's function $g^{\mathrm{A}}_{[\mathbf{k},\mathbf{G},\omega]}(\mathbf{G}')$ via Eq. 5.32 we also make use of the symmetries of the entire space group of the crystal. The transformation law is most easily seen by considering the *formal* expansion of the Green's function over the entire set of single-particle states $u_{n\mathbf{k}}$:

$$G_{\mathbf{k}}(\mathbf{r},\mathbf{r}',\omega) = \sum_{n} \frac{u_{n\mathbf{k}}(\mathbf{r}) u^{*}_{n\mathbf{k}}(\mathbf{r}')}{\omega - \varepsilon_{n\mathbf{k}}}. \tag{5.45}$$

The same transformation law for the states $u_{n\mathbf{k}}$ leading to Eq. 5.43 gives in this case:

$$G_{\mathcal{S}\mathbf{k}}(\mathbf{G},\mathbf{G}',\omega) = G_{\mathbf{k}}(\mathcal{S}^{-1}\mathbf{G},\mathcal{S}^{-1}\mathbf{G}',\omega), \tag{5.46}$$

where use was made of the convention expressed by Eq. 3.18.

If we now restrict the symmetry operations to the small group of $\mathbf{k}$, $\mathcal{G}(\mathbf{k}) = \{\mathcal{S}|\mathcal{S}\mathbf{k} = \mathbf{k} + \mathbf{G}\}$, then the last equation can be adapted to reduce the number of explicit solutions of Eq. 5.32:

$$G_{\mathbf{k}}(\mathcal{S}\mathbf{G},\mathbf{G}',\omega) = G_{\mathbf{k}}(\mathbf{G},\mathcal{S}^{-1}\mathbf{G}',\omega). \tag{5.47}$$

Lastly, it is possible to restrict the Brillouin zone sum in Eq. 5.33 by using only the $\mathbf{q}$ vectors which are irreducible with respect to the symmetry operations belonging to the small group $\mathcal{G}(\mathbf{k})$. This is possible since whenever $\mathcal{S}\mathbf{k} = \mathbf{k} + \mathbf{G}$ we can replace $G_{\mathbf{k}+\mathcal{S}\mathbf{q}} W_{\mathcal{S}\mathbf{q}}$ in Eq. 5.33 by its symmetry-equivalent $G_{\mathcal{S}^{-1}\mathbf{k}+\mathbf{q}} W_{\mathbf{q}} = G_{\mathbf{k}+\mathbf{q}} W_{\mathbf{q}}$. As an example of the saving afforded by the use of symmetry, in a highly symmetric crystal such as the typical example of silicon, the number of

evaluations of the Sternheimer equation is reduced by a factor of ~ 50.

As a final note, the convolutions over the Brillouin zone required to construct Σ^{ex}, Eq. 5.35, and Σ^{c}, Eq. 5.36, are also reduced. The small group of the point $\mathbf{k}$ determines the size of the irreducible Brillouin zone over which the convolution must be performed. In the following $w_{\mathbf{q}}$ is the weight of each $\mathbf{q}$ point (i.e. the ratio of the number of points in the full Brillouin zone which are equivalent under a symmetry operation to the total number of points used to sample the Brillouin zone) the exchange self-energy can now be written as:

$$\Sigma^{\text{ex}}_{\mathbf{k}}(\mathbf{r},\mathbf{r}') = \frac{i}{2\pi}\sum_{\mathbf{q}\in \text{IBZ}_{\mathbf{k}}} w_{\mathbf{q}}\psi_{\mathbf{k}-\mathbf{q}}(\mathbf{r})\psi^{*}_{\mathbf{k}-\mathbf{q}}(\mathbf{r}')v_{\mathbf{q}}(\mathbf{r},\mathbf{r}'), \tag{5.48}$$

and the correlation energy can be written as:

$$\Sigma^{\text{c}}_{\mathbf{k}}(\mathbf{r},\mathbf{r}';\omega) = 2\pi i\int_{-\omega_{\text{c}}}^{\omega_{\text{c}}}\sum_{\mathbf{q}\in \text{IBZ}_{\mathbf{k}}} w_{\mathbf{q}}G_{\mathbf{k}-\mathbf{q}}(\mathbf{r},\mathbf{r}';\omega+\omega')\left[W_{\mathbf{q}}(\mathbf{r},\mathbf{r}';\omega') - v_{\mathbf{q}}(\mathbf{r},\mathbf{r}')\right]d\omega'. \tag{5.49}$$

5 Frequency dependence

In this section we describe the strategies that we have examined for handling the frequency dependence of the Green's function and the screened Coulomb interaction.

The linear systems of equations that we are required to solve to construct the screened Coulomb interaction, Eq. 5.28, and the Green's function Eq. 5.32, both involve non-Hermitian operators. This means standard methods employed in ground state electronic structure calculations, for instance, the conjugate gradient method can no longer be used.

The presence of non-Hermitian operators, makes it necessary to replace the standard conjugate gradients method for the solution of these linear systems by its extension to non-Hermitian operators. These generalizations include the complex bi-conjugate gradients method (cBiCG) Ref. [127], the multishift version

of the cBiCG algorithm [124], and the stabilized version of cBiCG as described in Refs. [124, 128], hereafter referred to as BiCGStab(l). For clarity we have included the algorithms as they have been implemented for the cBiCG, cBiCG multishift, and BiCGStab(l) methods in Appendix C.

In this section we focus on two aspects regarding the frequency dependence of the Green's function, the screened Coulomb interaction, and the self-energy. The first is the use of the multishift solver to generate the full frequency dependence of the Green's function and the screened Coulomb interaction. The second is the use of analytic continuation so that calculations performed on the imaginary axis, can be extended to the real axis.

5.1 Multishift solver

In order to solve the non-Hermitian eigenvalue problem given by Eq. 5.32 we used the *multishift linear system solver* introduced by Frommer in Ref. [124]. The rationale for this choice is that the multishift method enables the construction of the complete spectral structure of the Green's function at the cost of one single frequency calculation.

Equation 5.32 is a special case of the general linear system:

$$(A + \omega I)x = b, \tag{5.50}$$

where A is a complex linear operator, b a known complex vector, I is the identity matrix, and x the unknown solution vector. This system can be thought of as being obtained from the "seed" system $Ax = b$ by "shifting" the operator A by a constant ω. Frommer's method relies on the observation that the Krilov subspaces associated with the seed and the shifted systems, i.e. $\{b, Ab, A^2b, \cdots\}$ and $\{b, (A + \omega I)b, (A + \omega I)^2b, \cdots\}$, span the same linear space. This makes it possible to build the solution vectors for both the seed and the shifted systems by performing only once the matrix-vector operations $Ab, A^2b, A^3b, \cdots$, and by

using different coefficients for the Krilov chains [124].

Our calculation proceeds in two steps. In the first step we address the seed system and solve Eq. 5.32 for $\omega = 0$ using the standard cBiCG algorithm. The cBiCG algorithm iteratively generates one sequence of solution vectors x_n, two sequences r_n and $\tilde{r}_n$ of biorthogonal residuals, and two sequences p_n and $\tilde{p}_n$ of search directions. The trial solution vector is set to $x_0 = 0$ in order to generate collinear residuals for the seed and shifted systems. The initial search directions are set to $p_0 = b$ and $\tilde{p}_0 = b^\star$. The calculation of each element of the solution sequence requires the evaluation of the following coefficients:

$$\alpha_n = \langle \tilde{r}_n | r_n \rangle / \langle \tilde{p}_n | A p_n \rangle, \tag{5.51}$$

$$\beta_n = -\langle A^\dagger \tilde{p}_n | r_{n+1} \rangle / \langle \tilde{p}_n | A p_n \rangle, \tag{5.52}$$

where $A^\dagger$ is the Hermitian conjugate of A [127]. The evaluation of the matrix-vector products Ap_n and $A^\dagger \tilde{p}_n$ is the time-consuming part of the whole procedure. The iterative solution continues until the residual $r_n = b - Ax_n$ becomes smaller than a given tolerance. At each iteration the residuals r_n and the coefficients α_n and β_n are stored for subsequent use with the shifted system.

In the second step of the procedure we address the shifted systems for each frequency ω. The sequence of residuals and the coefficients calculated for the seed system are retrieved and used to generate the corresponding quantities $r_{n,\omega}$, $\alpha_{n,\omega}$, and $\beta_{n,\omega}$ for the shifted operators $A - \omega I$. The recurrence relations for the Krilov chains of the shifted system are:[124]

$$r_{n,\omega} = \frac{r_n}{\pi_{n,\omega}}, \quad \alpha_{n,\omega} = \frac{\pi_{n,\omega}}{\pi_{n+1,\omega}} \alpha_n, \quad \beta_{n,\omega} = \left(\frac{\pi_{n,\omega}}{\pi_{n+1,\omega}} \right)^2 \beta_n, \tag{5.53}$$

with the coefficient $\pi_{n+1,\omega}$ given by:

$$\pi_{n+1,\omega} = (1 + \omega \alpha_n) \pi_{n,\omega} + \frac{\alpha_n \beta_{n-1}}{\alpha_{n-1}} (\pi_{n,\omega} - \pi_{n-1,\omega}). \tag{5.54}$$

Owing to these relations, in the case of the shifted systems we do not perform any matrix-vector operations. Since the application of the Hamiltonian to trial solutions is the most expensive part of the solution of Eq. 5.32, the use of the multishift method leads to a substantial computational saving. This will be demonstrated in Chapter 6.

For systems larger than those considered in this study, and for systems that require very high kinetic energy cutoffs, it may become necessary to use preconditioning schemes. While it should be possible to adapt polynomial preconditioners designed for Krilov multishift solvers, [129, 130] we did not explore this direction. Instead we experimented with the calculation of the Green's function in Eq. 5.32 using the standard (non-multishift) BiCGStab(l) algorithm, Ref. [128] and Ref. [131] combined with a slightly modified version of the Teter-Payne-Allen (TPA) preconditioner and Ref. [132].

The TPA conditioning matrix consists of a diagonal matrix whose elements are given by:

$$M_{\mathbf{k}}(\mathbf{G},\mathbf{G}') = \frac{27+18x+12x^2+8x^3}{27+18x+12x^2+8x^3+16x^4}\delta_{\mathbf{G},\mathbf{G}'}, \tag{5.55}$$

with $x = |\mathbf{k}+\mathbf{G}|^2/2E_{\text{kin}}^{\text{ref}}$ and $E_{\text{kin}}^{\text{ref}}$ a reference kinetic energy. This matrix ensures that the high-frequency Fourier components of the Kohn-Sham Hamiltonian (dominated by the kinetic energy) are "renormalized" to $E_{\text{kin}}^{\text{ref}}$, and the spectrum of the conditioned system is effectively compressed.

In the case of Eq. 5.32 the high-frequency Fourier components of the linear operator correspond to $|\mathbf{k}+\mathbf{G}|^2-\omega$, therefore the same effect as above is obtained by using:

$$x = (|\mathbf{k}+\mathbf{G}|^2-\omega)/2E_{\text{kin}}^{\text{ref}} \tag{5.56}$$

instead of the original TPA prescription. This corresponds to a translation of the TPA preconditioner along the energy axis. When $x<0$ (i.e. when $|\mathbf{k}+\mathbf{G}|^2<\omega$)

we set $M_{\mathbf{k}}(\mathbf{G},\mathbf{G}') = \delta_{\mathbf{G},\mathbf{G}'}$ in order to preserve the smooth behaviour of the TPA conditioner at low energy.

5.2 Analytic continuation

One of the motivations for the Sternheimer-*GW* method is creating a framework where the full frequency dependence of the operators is explicitly treated. In the next chapter we will present the quasiparticle spectral functions for silicon and diamond. For these plots we require the complete spectral structure of the screened Coulomb interaction and the Green's function. For real frequencies the linear operator in Eq. 5.28 can become singular. This leads to severe numerical difficulties in both the self-consistent and non self-consistent procedures. This motivates the solution of Eq. 5.28 for imaginary frequencies followed by an approximate analytic continuation to the real axis via Padé functions [50, 52, 133]. In the context of *GW* calculations the use of Padé approximants has been demonstrated in Refs. [50, 53, 54].

Given a function $f(\omega)$ whose values are known in N distinct frequencies $\omega_1, \ldots, \omega_N$ the Padé approximant of order N is defined as the rational function of order N [i.e. with numerator and denominator of order $(N \operatorname{div} 2)$] which matches f at each of these frequencies, and provides the best approximation to f outside of these points:

$$f(\omega) = \frac{p_1 + p_2\omega + \ldots + p_l\omega^l}{q_1 + q_2\omega + \ldots + q_{m-1}\omega^{m-1} + \omega^m}, \tag{5.57}$$

The coefficients of the polynomials are obtained by setting $f(\omega_i) = W_{\mathbf{q}}(\mathbf{G},\mathbf{G}',\omega_i)$ for $i = 1, \ldots, N$, and using the recursive algorithm of Ref. [133] and reproduced in Appendix B. Here we choose all the frequencies $\omega_1, \ldots, \omega_N$ to lie on the imaginary axis. In the present case of Sternheimer-*GW* calculations the use of Padé approximants with purely imaginary frequencies is especially useful. In fact choice guarantees that the worst-case scenario for the condition number

of the linear system in Eq. (5.28) corresponds to $\omega = 0$. Other choices for the frequencies $\omega_1, \ldots, \omega_N$ are certainly possible. For example one could set the Padé frequencies along an optimized path in the complex plane. This approach has been examined in Ref. [134] where the quality of the analytic continuation was found to improve substantially as the functions are sampled for contours parallel to the real axis with a constant displacement along the imaginary axis.

In Chapter 6, to make the link between Sternheimer-*GW* calculations and *GW* calculations based on the sum-over-states approach, we also employ the use of the Godby-Needs plasmon-pole model first described in Ref. [46]. It is interesting to point out that the Godby-Needs plasmon-pole model can be seen as a special case of Padé approximants, where the order of the rational function is set to $N = 2$ (i.e. two evaluations of W are required for each set of $\mathbf{q}, \mathbf{G}, \mathbf{G}'$).

Implementation and Parallelism

The *ab initio* Sternheimer-*GW* method has been implemented by starting from the QUANTUM ESPRESSO implementation of density-functional perturbation theory using the PHONON code described in Ref. [110]. The Sternheimer-*GW* approach is intrinsically parallel. This parallelism applies to the construction of the Green's function and the screened Coulomb interaction. Eq. 5.32 and Eq. 5.28 can be solved independently for every $\mathbf{G}$. For each $\mathbf{G}$-component of the Green's function $g^{\mathrm{A}}_{[\mathbf{k},\mathbf{G},\omega]}(\mathbf{G}')$ can be calculated on one processor independently of the other components and similarly for the first order response of the wavefunction $\Delta u^{\pm}_{v\mathbf{k}[\mathbf{q},\mathbf{G},\omega]}$. All the vectors $g^{\mathrm{A}}_{[\mathbf{k},\mathbf{G},\omega]}$ are then collected on a single processor before proceeding to the evaluation of the self-energy. The resulting W and G are collected at the end using global communications. The timing and scaling of the parallel implementation is analyzed in Chapter 6.

6 Conclusion

In this chapter we have presented the Sternheimer-*GW* formalism. We have discussed the use of the Sternheimer equation to calculate the dielectric response function of an electronic system and how this can be used to construct the screened Coulomb interaction. Similarly we have discussed the techniques for constructing the Green's function in terms of the occupied electronic states and the solution of a linear system of equations. We have discussed the computational techniques for obtaining solutions of these linear systems. In particular we have discussed the efficiency of multishift linear system solvers and the role crystal symmetry plays in reducing the computational workload of the procedure.

There are two distinct advantages of the Sternheimer-*GW* method. The first is that it avoids from the outset the use of unoccupied Kohn-Sham states. The second is that the numerical convergence of the Sternheimer-*GW* method is controlled by the planewave cutoff of the dielectric matrix.

In the next chapter we will demonstrate the Sternheimer-*GW* method by discussing its application to semiconducting and insulating crystals.

6 Tests and Validation of the Sternheimer-GW Method

In this chapter we validate the *ab initio* Sternheimer approach to GW calculations presented in Chapter 5. Initially we present some results for the polarizability of small molecules in order to validate the implementation of the Sternheimer equation for electronic response calculations. We then move on to performing full GW calculations of the quasiparticle energies for standard semiconductors and insulators including silicon, diamond, lithium chloride, and silicon carbide. The focus of the GW calculations presented here is three-fold. First, we compare our calculations of quasiparticle eigenvalues with the results of the standard sum-over-states approach to demonstrate the convergence and scaling properties of our method. Then we proceed to calculate the complete quasiparticle spectral functions of silicon and diamond extracting information about quasiparticle lifetimes from the line broadening. We also discuss the scaling and computational workload required to perform these calculations. We conclude this chapter by discussing the spatial structure of the full GW self-energy for silicon and the consequences of RPA+V^{xc} screening on the quasiparticle energies of silicon. The work presented in Sections 2-4, has been published in Ref. [135].

1 Polarizability calculations

As mentioned, the original application of the Sternheimer equation was to calculate the polarizability of atomic systems [90, 136]. Calculations of the dipole moment and polarizability of small molecular systems provide a useful test of the initial implementation of the Sternheimer-GW method. These calculations can also be compared to similar calculations performed using Gaussian basis sets.

The molecular polarizability can be calculated in a similar manner to the construction of the screened Coulomb interaction discussed in Chapter 5. However, in the case of the frequency-dependent polarizability, the self-consistent density response, $\Delta n_i(\mathbf{r}, \omega)$ is calculated for a sawtooth electric field directed along i. The dipole moment of Δn_i gives the polarizability tensor:

$$\alpha_{ij}(\omega) = \int d^3\mathbf{r} \Delta n_j(\mathbf{r}, \omega) r_i, \tag{6.1}$$

a detailed derivation of the equations leading to Eq. 6.1 is given in Ref. [134]. The quantity measured experimentally is:

$$\bar{\alpha}(\omega) = \frac{1}{3} \sum_{i=1}^{3} \alpha_{ii}(\omega), \tag{6.2}$$

where $\bar{\alpha}(\omega)$ is the isotropic average of the polarizability tensor.

Self-consistent Sternheimer calculations were performed on a series of molecules within a $30 \times 30 \times 30$ bohr^3 unit cell, and using the spherical Coulomb truncation discussed in Chapter 3. The plane wave cutoff was 80 Ry for the wavefunctions in CO and N_2, 70 Ry for the H_2O molecule, 60 Ry for H_2, HCl, and N_2. The self-consistent density response was calculated until the magnitude of the relative change in the integrated density response was lower than 10^{-10}. In all cases the Perdew-Zunger, parametrization of the exchange correlation functional was used [12], and Troullier-Martins norm-conserving pseudopotentials were used [137].

In Table 6.1 we compare our calculations of the polarizability along different axes for the carbon monoxide molecule (CO). The carbon-oxygen bond is oriented along the z-axis. Our calculations are compared with those of Ref. [138], where a real space grid is used to represent the wavefunctions, and Ref. [139] and Ref. [140] which both employ a Gaussian basis set and a sum-over-states formulation.

In Table 6.2 we present the static isotropic average of the polarizability,

	Ref. [138]	Ref. [139]	Ref. [140]	Present
α_{xx}	12.55	12.11	12.58	12.66
α_{zz}	15.82	16.00	15.88	15.88
$\bar{\alpha}$	13.64	13.41	13.68	13.73

Table 6.1: Static polarizability of CO as calculated using the real space formulation of Ref. [138], using Gaussian basis sets Ref. [139] and Ref. [140] and the present plane wave formulation of the Sternheimer method.

Molecule	Ref. [140]	Present	Experiment
H_2	5.9	5.9	5.18
N_2	12.27	12.38	11.74
HCl	18.63	18.73	17.39
H_2O	10.53	10.64	9.64
CO	13.87	13.73	13.09

Table 6.2: Static polarizability of a number of small molecules compared to the calculations performed using a Gaussian basis set and sum-over-states formulation and experimental data quoted in Ref. [140].

Eq. 6.2, for a small set of molecules, and compare them with those calculated using a Gaussian basis set and a sum-over-states formulation [140].

In all cases the agreement with previous calculations is good, and the agreement with experiment is reasonable for the level of theory. The root mean square (RMS) difference between our method and the real space calculation of Ref. [138] and our present calculation for CO was 0.6% compared to 1.5% for the calculations performed using Gaussian basis sets in the sum-over-states, as expected. In Table 6.2 the RMS difference between present calculations and Ref. [140] for the small molecule test set is 0.8%.

The advantages of the real space formulation of Ref. [138] and the present Sternheimer formulation for calculating the polarizability is the ability to systematically converge the description of the polarizability by refining the resolution of the grid or the planewaves cutoff.

The discrepancy with experiment which can be seen in Table 6.2 in the polarizability of the molecules considered here is attributed to the use of the LDA to describe exchange and correlation. Beyond their value as a benchmark, these

calculations of the polarizability could be used in future work to study the effects of replacing the LDA parametrization of the exchange and correlation potential with more recent functionals.

2 Quasiparticle corrections

The work on the polarizability of small molecules provides a basic verification of the implementation of the Sternheimer equation for calculating electronic response properties. A more comprehensive challenge is to obtain the full dielectric matrix and Green's function for a crystalline system. In this section we discuss the details of performing full Sternheimer-*GW* calculations of quasiparticle properties. We also discuss the comparison of the method with previous implementations in terms of numerical convergence and computational efficiency.

2.1 Quasiparticle eigenvalues

In this section we validate our method by comparing the quasiparticle corrections of Si, C, SiC, and LiCl obtained using Sternheimer-*GW* and those obtained in previous calculations.

To obtain the ground-state wave-functions and eigenvalues we performed DFT calculations using the `Quantum Espresso` electronic structure package. DFT calculations were performed within the local density approximation (LDA) using the Perdew-Zunger parametrization [12]. We used Troullier-Martins norm-conserving pseudopotentials [137], with planewaves kinetic energy cutoffs set to 20 Ry for Si, and 60 Ry for diamond, SiC, and LiCl. In Fig. 6.1 we demonstrate the convergence properties with planewave cutoff on the correlation energy for the systems considered in this chapter. We used a shifted 6×6×6 Monkhorst-Pack mesh [141] in order to describe the DFT electron density, as well as the screened Coulomb interaction W. The dielectric matrices were described using kinetic energy cutoffs of 10, 24, 20, and 15 Ry for silicon, diamond, silicon carbide, and lithium chloride, respectively. The exchange part of the self-energy was

calculated using the same cutoff as the density. The singularity in the Coulomb interaction at long wavelength was removed by using the spherical truncation scheme of Ref. [68] and discussed in Chapter 3.

In the case of the self-consistent solution of Eq. 5.28 we used an adaptive threshold in order to speed up the convergence of the combined procedure consisting of cBiCG iterations and density updates.

The quasiparticle corrections are defined with reference to the LDA Kohn-Sham eigenvalues using the prescription described in Ref. [142] and summarized

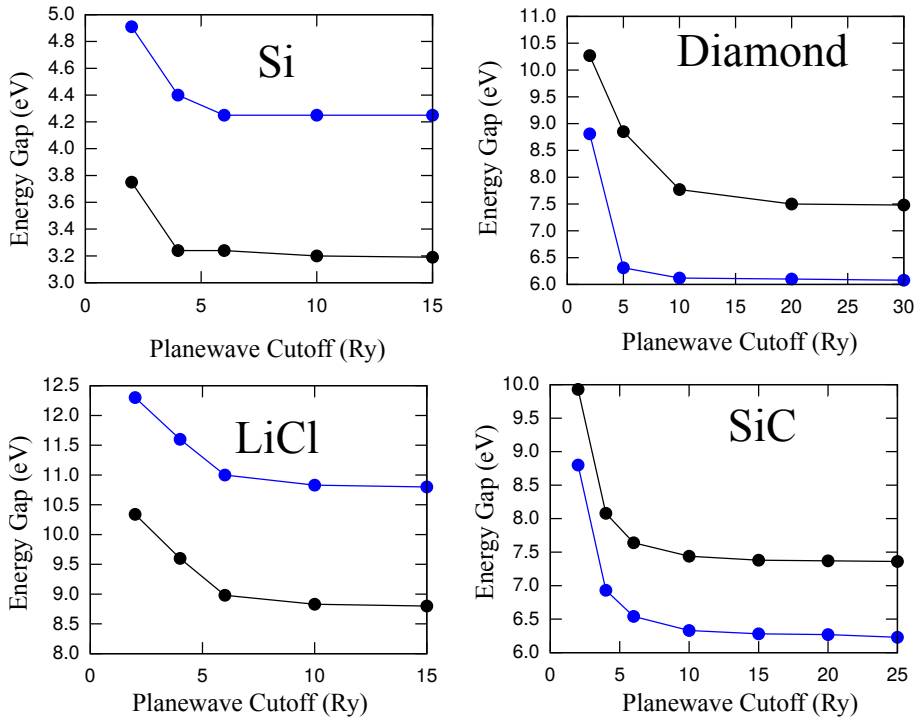


Figure 6.1: The convergence with planewave cutoff used to describe the self-energy operator of the quasiparticle energy gaps in Si, C, SiC, and LiCl. In general the correlation energy has a smoother spatial variation than the crystal wavefunctions and can be computed using a lower planewave cutoff. Curves in black represent the direct energy gap at Γ in eV. For completeness we have also included the convergence of the $\Gamma \rightarrow X$ transition for the different systems in blue.

in Chapter 3:

$$\Delta\varepsilon_{n\mathbf{k}} = Z_{n\mathbf{k}}\Delta\Sigma_{n\mathbf{k}}(\varepsilon_{n\mathbf{k}}), \tag{6.3}$$

where $Z_{n\mathbf{k}}$ is the quasiparticle renormalization of the state $\phi_{n\mathbf{k}}$.

In all cases discussed in this section we used the Godby-Needs plasmon-pole model, in order to be consistent with the sum-over-states method and previous calculations. We determine the plasmon-pole parameters by using the values of the dielectric matrix at $\omega = 0$ and at 1.2 Ry for Si and C, and at 1.3 Ry for SiC and LiCl. These values were chosen to be consistent with the classical plasma frequency. The Green's function was calculated on a uniform frequency grid slightly off the real axis. In particular we used frequencies equally spaced by 0.1 eV in the range $\pm$150 eV, and with an imaginary component of 0.3 eV. The calculation of the self-energy in Eq. (5.33) was performed numerically along the real axis, using a spacing of 0.1 eV and a broadening of 0.3 eV. The integration boundaries were set to $\pm$120 eV.

Fig. 6.2 depicts the Brillouin zone for the diamond and zinc-blend structure, with some of the high symmetry points highlighted.

Table 6.3 shows the quasiparticle energies of Si obtained using the Sternheimer-*GW* method. These values are compared to previously published calculations based on the sum-over-states approach, as well as experiment. In table 6.3 the agreement between the experimental data and the Sternheimer-*GW* calculations is very good. The calculations presented in Ref. [53] show some notable discrepancies, in particular at the X point in the Brillouin zone. In Ref. [44] and Ref. [147] it has been suggested this discrepancy is largely to do with the convergence with respect to empty states.

Table 6.4 shows our quasiparticle calculations for diamond. In this case the agreement with the calculations presented in Ref. [30] is within 0.1 eV. This is reasonable considering that in Ref. [30] the authors employ a different truncation strategy for the singularity in the Coulomb potential, and they truncate their

summations for the dielectric matrix and Green's function at 196 bands.

Finally, Table 6.5, shows results for the wide band gap insulators SiC and LiCl in Table 6.5. In the case of LiCl the values reported in Ref. [36] are actually the result of incorporating a level of self-consistency in the calculation. Ref. [36] also reports a value for the direct gap at the Γ-point of 8.9 eV for a G_0W_0 calculation which, is in good agreement with the present work.

In general, the agreement of Sternheimer-*GW* with previous calculations and experiment is very good. The small residual discrepancies of the order of 0.1 eV are assigned to the incomplete convergence of previous calculations, and to the integration scheme used to perform the convolution of the Green's function and the screened Coulomb interaction in the Sternheimer-*GW* approach.

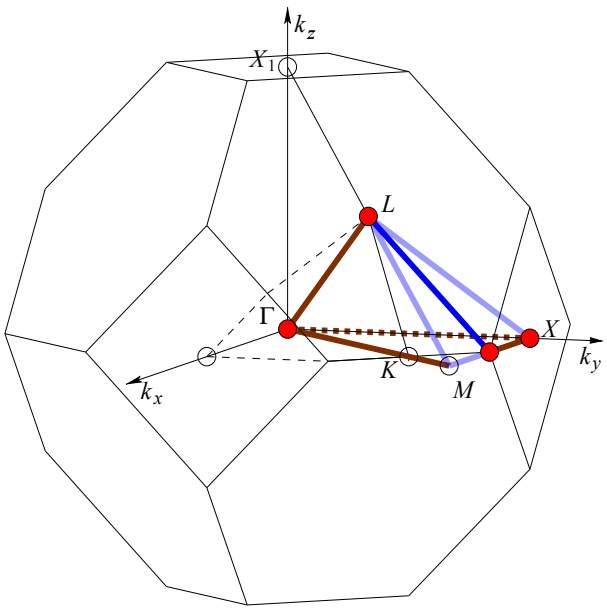


Figure 6.2: The Brillouin zone for diamond and zinc-blend structures studied in this chapter. High symmetry points referred to in this chapter are indicated. Figure adapted from Ref. [143].

	DFT/LDA		*GW*		Experiment
	Present	Ref. [53]	Present	Ref. [53]	
Γ'_{25v}	0.00	0.00	0.00	0.00	0.00
Γ_{15c}	2.55	2.54	3.26	3.09	3.40[a], 3.05[b]
X_{4v}	-2.87	-2.85	-2.92	-2.90	-3.3 $\pm$ 0.2[c]
X_{1c}	0.65	0.61	1.32	1.01	1.25[b]
L_{1v}	-6.99	-6.99	-7.10	-6.97	-6.7 $\pm$ 0.2[a]
L'_{3v}	-1.21	-1.19	-1.18	-1.16	-1.2 $\pm$ 0.2[a]
L_{1c}	1.49	1.44	2.19	2.05	2.4 $\pm$ 0.15[a]
L_{3c}	3.34	3.30	4.09	3.83	4.15$\pm$ 0.1[a]

Table 6.3: ([a]Ref. [144] [b]Ref. [145] [c]Ref. [146]) Quasiparticle energies corresponding to the band edges of Si at high-symmetry points: comparison between the results of Sternheimer-*GW* calculations and previous work. The initial DFT/LDA eigenvalues are reported for completeness. All values are in units of eV and the zero of the energy is set to the top of the valence bands in all cases.

	DFT/LDA		*GW*		Experiment
	Present	Ref. [30]	Present	Ref. [30]	
Γ'_{25v}	0.00	0.00	0.00	0.00	0.00
Γ_{15c}	5.6	5.58	7.50	7.63	7.3[a]
X_{4v}	-6.27	-6.26	-6.68	-6.69	.
X_{1c}	4.65	4.63	6.12	6.30	.
L_{1v}	-13.46	-13.33	-14.18	-14.27	-12.8$\pm$0.3[b]
L_{3v}	-2.82	-2.78	-2.93	-2.98	.
L_{1c}	8.49	8.39	10.53	10.63	.
L_{3c}	8.89	8.76	10.30	10.23	.

Table 6.4: ([a]Ref. [144] [b]Ref. [148]) Quasiparticle energies corresponding to the band edges of diamond at high-symmetry points.

2.2 Convergence of quasiparticle eigenvalues

In order to further validate the Sternheimer-*GW* method we performed *GW* calculations based on the sum-over-states approach. These calculations were performed using the `SaX` code Ref. [118], which used identical Kohn-Sham wavefunctions and eigenvalues obtained from `Quantum Espresso` as those used in the Sternheimer-*GW* method. In order to ensure consistency we used identical parameters, i.e. exchange and correlation functional, lattice parameters, truncation strategies and pseudopotentials in the `SaX` and Sternheimer-*GW* calculations.

	DFT/LDA		*GW*		Experiment
	Present	Previous	Present	Previous	
SiC					
Γ_{15v}	0.00	0.00	0.00	0.00	0.00
Γ_{1c}	6.34	6.25[a]	7.31	7.35[a]	7.4[b]
X_{5v}	-3.24	-3.20[c]	-3.53	-3.53[c]	.
X_{1c}	1.36	1.31[c]	2.12	2.19[c]	2.39[d]
L_{3v}	-1.08	-1.06[c]	-1.07	-1.21[c]	-1.15[d]
L_{1c}	5.40	5.34[d]	6.23	6.45[a]	6.35[d]
LiCl					
Γ_{1c}	5.90	6.00	8.80	9.10	9.4[e]
X_{4v}	-2.90	-3.00	-3.00	-3.30	.
X_{5v}	-1.10	-1.10	-1.20	-1.30	.
X_{1c}	7.50	7.50	10.80	10.70	.

Table 6.5: ([a]Ref. [53], [b]Ref. [149], [c]Ref. [30], [d]Ref. [144], [e]Ref. [150]) Quasiparticle energies corresponding to the band edges of SiC, and LiCl at high-symmetry points. All previous calculations for LiCl are from Ref. [36].

This limits the differences between results in the calculations to issues relating to numerical convergence.

In Figs. 6.3, and 6.4 we compare the quasiparticle corrections to the band edges in silicon and diamond, calculated by us using Sternheimer-*GW* (blue solid lines) and using the standard method as implemented in `SaX` (red dashed lines). These figures demonstrate that our method and the sum-over-states approach yield essentially the same quasiparticle corrections, provided a large number of unoccupied states is included in the latter calculation. The convergence of *differences* of quasiparticle corrections is relatively fast within the sum-over-states approach, however the calculation of *absolute* quasiparticle energies is considerably more challenging.

In fact, fully-converged sum-over-states calculations of the absolute quasiparticle energies require cutoffs comparable to that of the underlying planewave basis set. This result was somewhat expected since the wavefunction cutoff enters the matrix elements of the polarizability in the sum-over-states approach in

Ref. [142].

The fact that the Sternheimer-*GW* calculations are able to provide absolute quasiparticle energies as opposed to relative corrections, without the need for unoccupied states, is expected to be important for the study of heterogeneous systems like surfaces, interfaces, and defects.

An interesting observation that we can make by inspecting Fig. 6.3, and Fig. 6.4 is that, in fully-converged calculations, the *GW* correction is not concentrated on the conduction band as it is generally assumed. For example, in the case of silicon our calculations suggest that the quasiparticle correction is actually concentrated in the valence band (Fig. 6.3), while in the case of diamond the correction to the band gap is equally distributed between valence and conduction bands (Fig. 6.4). These findings are in line with recent calculations on oxides and semiconductors where similar trends were observed, [43, 45], and suggest that some caution should be used when applying semi-empirical scissor corrections.

We now analyze in detail the calculated quasiparticle corrections to the band edges of diamond at Γ, i.e. the Γ'_{25v} and Γ_{15c} states, shown in Fig. 6.4(a). This example is representative of all the test cases considered here. The corrections to the Γ_{15c} state calculated using Sternheimer-*GW* and the sum-over-states approach are identical to within 0.01 eV. The corrections to the Γ'_{25v} state are -0.86 eV (Sternheimer-*GW*) and -0.80 eV (fully converged sum-over-states). In this case the renormalization factor (0.83) and the bare exchange contribution to the quasiparticle correction (-19.21 eV) are the same in both methods, and the small residual discrepancy of 0.06 eV comes from the correlation part of the self-energy. We assign this small discrepancy to the different strategies used to perform the frequency integral in Eq. (5.33), since the standard method performs an analytic integration while we use numerical integration.

At any rate these very small differences are well below the typical accuracy

expected from converged *GW* calculations, especially if we take into account the dependence on the pseudopotentials, the initial choice of the DFT exchange and correlation functional and effects due to *GW* self-consistency or the lack thereof.

3 Quasiparticle spectral function

In this section we present examples of calculations of the quasiparticle spectral functions of silicon and diamond (Figs. 6.5 and 6.6). All the calculations were

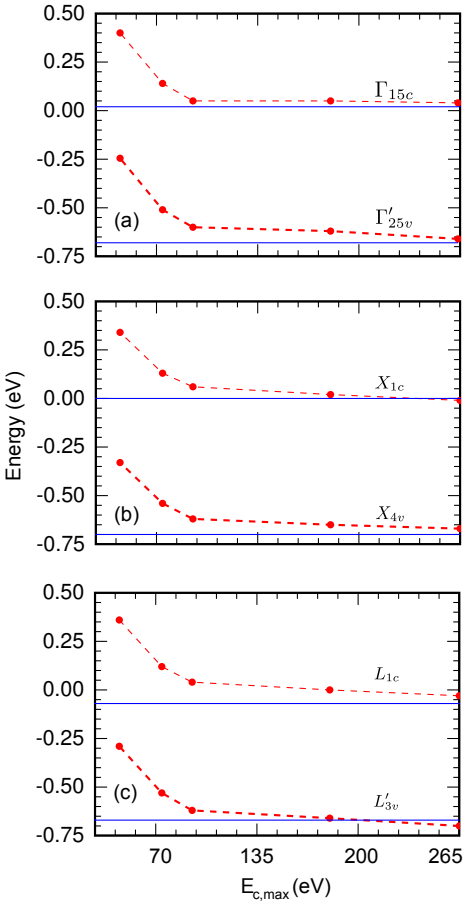


Figure 6.3: Quasiparticle corrections to the band edges at high-symmetry points in silicon: Sternheimer-*GW* (solid blue line), and sum-over-states approach as implemented in `SaX` (red disks and dashed line). The corrections are shown as a function of the energy of the highest unoccupied state included in the sum-over-states calculation. The zero of the energy is set to the top of the valence band. Top: Band edges at Γ, middle: band edges at X, and, bottom: band edges at L.

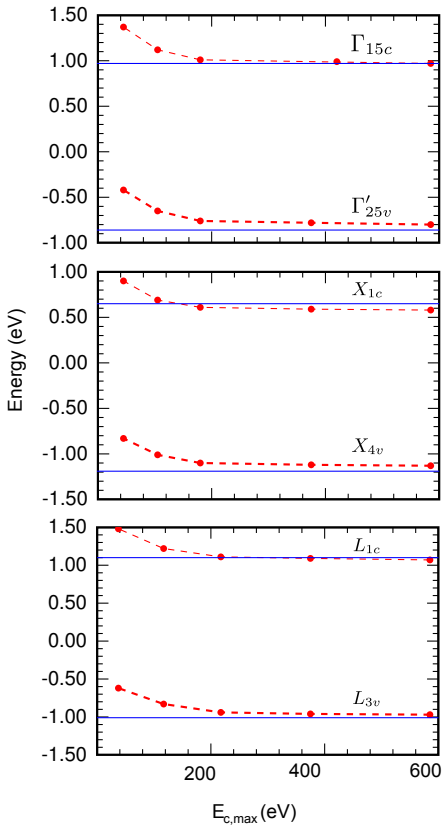


Figure 6.4: Quasiparticle corrections to the band edges at high-symmetry points in diamond: Sternheimer-*GW* (solid blue line), and sum-over-states approach as implemented in `SaX` (red disks and dashed line). The corrections are shown as a function of the energy of the highest unoccupied state included in the sum-over-states calculation. The zero of the energy is set to the top of the valence band. Top: band edges at Γ, middle: band edges at X, and bottom: band edges at L.

performed using Padé approximants as discussed in Sec. 5.2. Once we have obtained the self-energy Σ using the Sternheimer-*GW* method, the evaluation of the spectral function using Eq. (3.46) is straightforward and is carried out as a post-processing operation.

In order to obtain the quasiparticle spectral functions we need to go beyond the plasmon-pole model. Evaluation of the screened Coulomb interaction along the imaginary frequency axis was performed at frequencies equally spaced by 2 eV up to the plasmon frequency, and equally spaced by 20 eV beyond this point and up to 100 eV. This sampling was meant to capture at once the finer

structure in the dielectric response at low frequency and the asymptotic behavior at large frequency.

The direct construction of the spectral function makes it possible to obtain not only standard quasiparticle energies, but also the intensities and widths of the quasiparticle peaks. For example from Fig. 6.5 we can extract the width of the Γ_{1v} state at the bottom of the valence band of silicon. We obtain a width of 1.3 eV, corresponding to a quasiparticle lifetime of 3.2 fs. This finding is in agreement with previous G_0W_0 calculations of the spectral function of silicon in Ref. [53] and Ref. [151]. The same analysis carried out for diamond in Fig. 6.6 shows that the width of the states near the valence band bottom at Γ is 1.8 eV. This finding is in line with ARPES experiments indicating a linewidth of $\sim$2 eV as reported in Ref. [152]. We note that our calculated spectral functions carry an intrinsic linewidth of 0.3 eV. This linewidth is an artefact resulting from our choice of evaluating the Green's function at frequencies slightly off the real axis. This artificial broadening accounts for the finite linewidths observed near the top of the valence bands in Figs. 6.5 and 6.6.

3.1 Plasmaronic band structure

Fig. 6.7 shows a magnification of the calculated spectral function of silicon at large binding energies (20-40 eV). In the G_0W_0 approximation the structure of the real and imaginary parts of the self-energy lead to an additional spectral feature, which was termed a "plasmaron" in Ref. [153]. Interestingly, such plasmaron structures exhibit energy vs. wavevector dispersion relations which closely mimic the standard electron band structure in the binding energy range of 0-20 eV. Here we limit ourselves to point out that the energy of such plasmarons is overestimated in G_0W_0, and that more sophisticated solutions of Hedin's equations (e.g. based on the cumulant expansion) are known to correct the spacing between the plasmon resonance and the quasiparticle eigenvalues, and to yield

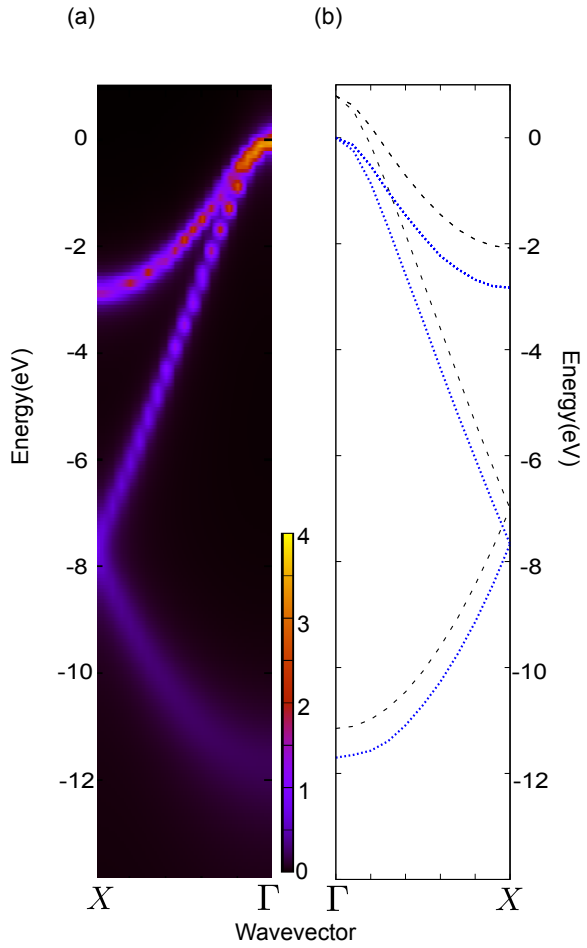


Figure 6.5: (a) Quasiparticle spectral function $A_{\mathbf{k}}(\omega)$ of silicon for $\mathbf{k}$ along Γ-X, calculated using the Sternheimer-GW method within the diagonal G_0W_0 approximation [Eq. (3.46)]. The "discrete" structure visible near the top of the valence bands is a visualization artefact, resulting from our choice of computing the self-energy at 20 equally spaced $\mathbf{k}$-points. (b) DFT/LDA band structure of silicon along Γ-X (black dashed lines), and the corresponding quasiparticle band structure obtained from (a) (blue solid lines). The units of the colorbar are eV^{-1}.

a series of satellites which are not captured within the G_0W_0 approximation. These effects have been studied in Refs. [154–157]. The current implementation of Sternheimer-GW carries the same limitations as the G_0W_0 approximation, hence Fig. 6.7 is only meant to show the capabilities of the method.

We note here that the dispersion of the plasmon resonance with wave vector is not included in Refs. [154–157]. This motivates using the G_0W_0 spectral functions

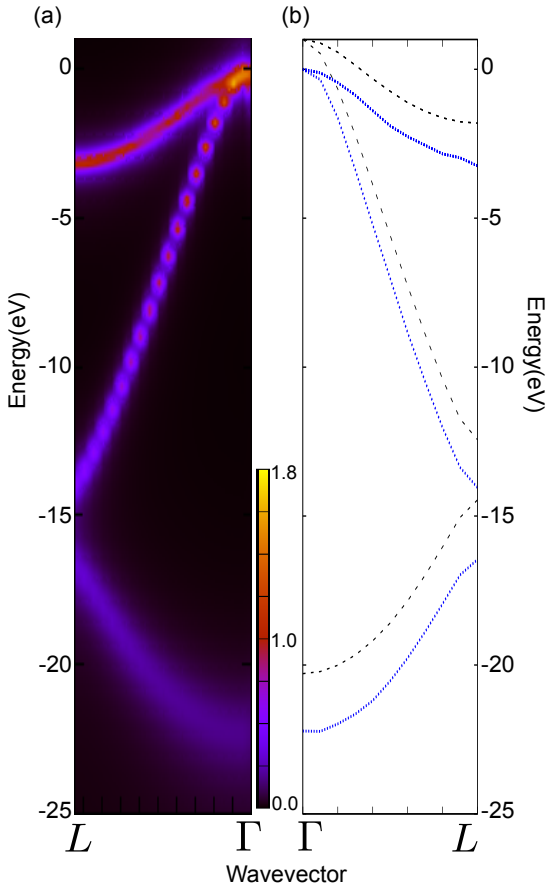


Figure 6.6: (a) Quasiparticle spectral function $A_{\mathbf{k}}(\omega)$ of diamond for $\mathbf{k}$ along Γ-L, calculated using the Sternheimer-GW method within the diagonal G_0W_0 approximation [Eq. (3.46)]. The "discrete" structure visible near the top of the valence bands is a visualization artefact, as discussed in Fig. 6.5, resulting from our choice of computing the self-energy at 20 equally spaced $\mathbf{k}$-points. (b) DFT/LDA band structure of diamond along Γ-L (black dashed lines), and the corresponding quasiparticle band structure obtained from (a) (blue solid lines). The units of the colorbar are eV^{-1}.

obtained within Sternheimer-GW as a starting point for more advanced calculations of photoemission satellites within the context of recent work described in Refs. [156, 157].

4 Scaling performance

Having discussed the physics of these quasiparticle calculations we also consider the computational workload involved in the Sternheimer-GW method. Fig. 6.8

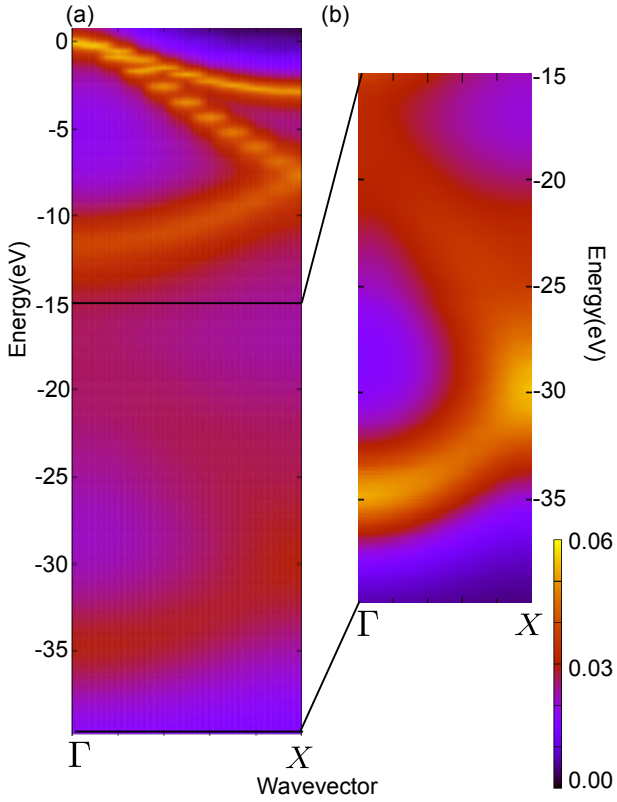


Figure 6.7: (a) Quasiparticle spectral function $A_{\mathbf{k}}(\omega)$ of silicon for $\mathbf{k}$ along Γ-X, calculated using the Sternheimer-GW method within the diagonal G_0W_0 approximation [Eq. (3.46)]. The energy range extends to -40 eV in order to show the "plasmaron band structure". The spectral function is given in a logarithmic scale in order to enhance the plasmaron satellites. (b) Zoom on the plot in (a) around the binding energy $15-40$ eV, showing the plasmaron band structure. In this case we use a linear scale with values given by the color bar. We note that the satellite energy is incorrect in the G_0W_0 approximation as discussed in Refs. [154–157]. The units of the colorbar are eV^{-1}.

reports the timing for the different stages of a calculation, construction of the screened Coulomb interaction, the construction of the Green's function, the convolution to produce the self-energy operator and the calculation of the quasiparticle corrections. We also examine how each of these stages scales with the number of processors employed. In this figure we see that the calculation of W is considerably more time-consuming than for G. This can be understood by comparing Eq. (5.28) and Eq. (5.32). In fact the calculation of the screened Coulomb

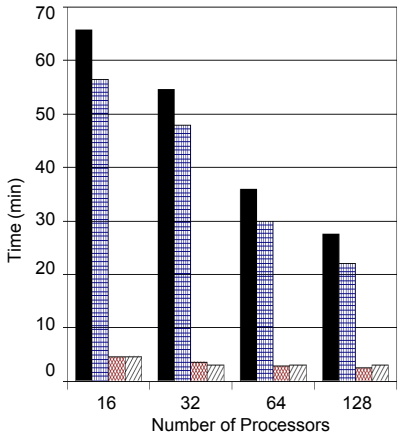


Figure 6.8: Parallel execution time for a Sternheimer-*GW* calculation of silicon. The construction of W here is carried out using a self-consistent solution. The time refers to a calculation of the complete self-energy $\Sigma_{\mathbf{k}}(\mathbf{G}, \mathbf{G}', \omega)$ with the parameters given in Sec. 5.2. We report the total execution time (full black bars), the time required for calculating the screened Coulomb interaction (straight cross-hatched blue bars), the Green's function (oblique cross-hatched red bars), and the frequency convolution in Eq. (5.33) (oblique hatched black bars).

interaction involves solutions for $\mathbf{k}$, $\mathbf{q}$, and the valence bands, while the calculation of the Green's function only involves solutions for the various $\mathbf{k}$-vectors in the irreducible Brillouin zone. The evaluation of the self-energy Σ is not parallel in the current implementation and the timing for this operation is a constant in Fig. 6.8.

The relative efficiency of the Sternheimer-*GW* and sum-over-states method has been discussed in Ref. [54]. If only the matrix elements of a subset of the states in the system are required and the summation is truncated, the Sternheimer approach has an equivalent scaling as the sum-over-states approach. However the Sternheimer approach has the added benefit of being converged from the outset and amenable to parallelization. In the case where the full self-energy operator is required, i.e. the full $\Sigma(\mathbf{r}, \mathbf{r}'; \omega)$ matrix needs to be computed, the Sternheimer approach is more efficient than the sum-over-states method. In the Sternheimer approach the full self-energy is obtained directly as a by-product of

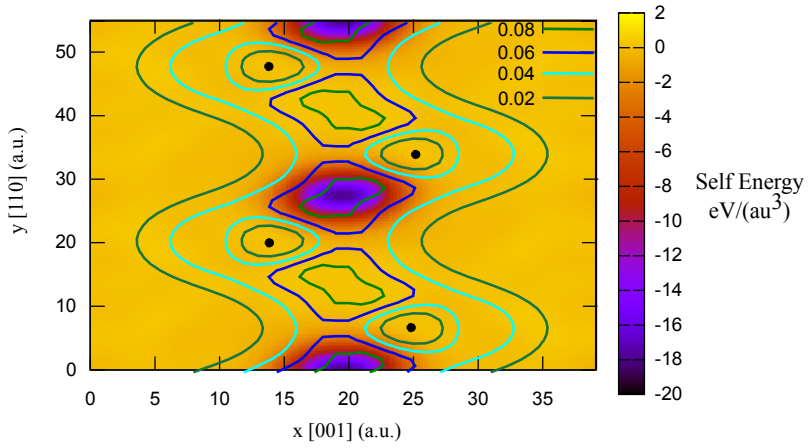


Figure 6.9: The spatial structure of the self-energy along a plane bisecting a chain of silicon bonds. $\Sigma(\mathbf{r}, \mathbf{r}'; \omega = \mathrm{E_g}/2)$ and $\mathbf{r}$ fixed at the bond center. The contour map gives the magnitude of the self-energy operator. The contour lines represent the electronic charge density in atomic units. Black dots are silicon atoms.

the calculation.

In the current implementation we only use one level of parallelization (over the $\mathbf{G}$ vectors). As a consequence the number of processors exceeds the number of symmetry-reduced planewave perturbations for certain $\mathbf{q}$ points. Therefore increasing the number of processors does not reduce the execution time. A second level of parallelization (over $\mathbf{q}$ vectors) would be needed in order to achieve linear parallel scaling.

5 Spatial structure of the self-energy

In the final section of this chapter we present two natural extensions of quasiparticle calculations based on the Sternheimer-*GW* framework. The first is the direct construction of the full $\Sigma(\mathbf{r}, \mathbf{r}'; \omega)$ self-energy operator rather than only calculating matrix elements with the single particle states. Having access to the full self-energy matrix allows one to construct the operator in real space. In Fig. 6.9 we present the real space structure of the self-energy in silicon. A similar calculation was presented in Ref. [158]. In Fig. 6.9 we have the first spatial variable

of the self-energy matrix, **r**, fixed at the bond center in silicon. The strongly localized nature of the self-energy is apparent in Fig. 6.9. The magnitude of the self-energy decreases from -20.0 eV/au^3 to $\pm$0.2 eV/au^3 within a range of 4.2 bohr. This is commensurate with the silicon bond length of 4.4 bohr.

6 Approximate Vertex Correction: RPA+$V^{\rm xc}$

Another useful aspect of the Sternheimer technique is the ease with which approximate vertex corrections can be incorporated into the calculations. In Ref. [36] the possibility of going beyond the RPA approximation by including the contribution of the exchange correlation potential at the LDA level was discussed. These approximate vertex corrections were performed in Ref. [119].

Recent calculations have suggested approximate vertex corrections to standard *GW* calculations are necessary for improving the agreement with experimental data. In particular Ref. [159] discusses the corrections to the valence electron band widths in Na and Li crystals at the RPA+$V^{\rm xc}$ level.

We have performed similar calculations to [119, 159] determine the effect of the approximate vertex corrections. Table 6.6 compares the results of quasiparticle eigenvalues and corrections performed with and without approximate vertex

	GW RPA	*GW* RPA+Vxc
Γ'_{25v}	0.00	0.00
Γ_{15c}	3.26	3.24
X_{4v}	-2.92	-2.93
X_{1c}	1.32	1.38
Abs. Γ'_{25v}	-0.61	-0.02
Abs. Γ_{15c}	0.09	0.66
Abs. X_{4v}	-0.66	-0.08
Abs. X_{1c}	0.04	0.70

Table 6.6: Quasiparticle energies corresponding to the band edges of Si at high-symmetry points. Comparison between the results of Sternheimer-*GW* calculations at the RPA level and with an approximate vertex correction in the response function. All values are in units of eV. The zero of the energy is set to the top of the valence bands in the top four rows. "Abs." indicate absolute corrections to the LDA eigenvalues.

corrections. While the relative quasiparticle eigenvalues in the two approaches are identical on the order of 0.01eV the absolute corrections to the quasiparticle eigenvalues are different. The correlation energy for the valence states is increased in the approximate vertex correction and the correction to the quasiparticle bandgap is concentrated on the conduction band.

7 Conclusion

In this chapter we have validated the Sternheimer-GW method by studying the quasiparticle properties of standard semiconducting and wide band gap insulating systems. We have compared our results with previous calculations based on the sum-over-states approach performed in a planewaves basis, and found very good agreement.

We have also produced quasiparticle spectral functions for silicon and diamond, and extracted information about quasiparticle lifetimes and plasmaronic structures. We have also discussed the scaling properties of the method, in particular the intrinsically parallel nature of the method which decouples the plane wave perturbations in the screened Coulomb interaction and in the Green's function. We have provided a graphical representation of the spatial structure of the self-energy in silicon, which allows for a visual understanding of the spatial structure of the G_0W_0 exchange and correlation potential.

In the next chapter we apply the Sternheimer-GW method to systems with reduced dimensionality, in particular layered transition metal dichalcogenides.

7 Quasiparticle Excitations in MoS_2

Following the discovery of single layer graphene there has been considerable interest in the electronic properties of other 2D materials [160, 161]. One such set of materials are the transition metal dichalcogenides (TMDs) [162].

The crystal structure of many TMDs is intrinsically layered with covalent bonding within the layer and van der Waals interactions between layers[163]. This means that single layers of these crystals can be isolated by mechanical or chemical exfoliation. Among the TMDs is molybdenum disulfide, MoS_2 [160, 162]. MoS_2 has a number of interesting optical and electronic properties. Interest in MoS_2 has led to the preparation of high quality bulk, monolayer, and stacked crystals Refs. [162, 164–166] and detailed experimental analysis of the optical and electronic properties Refs. [167–172]. In terms of *ab initio* studies the ground state band structure of MoS_2 has been investigated in Ref. [173] and Ref. [174]. A number of calculations have also been performed at the *GW* level [175–179].

In this chapter we perform quasiparticle calculations on bulk and monolayer MoS_2 using the Sternheimer-*GW* methodology. We examine the differences in the dielectric screening as a function of wavevector and frequency between bulk MoS_2 and the monolayer. We investigate the variability in the reported quasiparticle eigenvalues in Refs. [175–179], which suggests there remains difficulties in performing fully converged *ab initio* calculations on MoS_2 . In particular we identify two potential sources of discrepancy: the convergence of the head of the dielectric matrix with respect to vacuum size in the case of the monolayer, and the planewave cutoff of the dielectric matrix for both bulk and monolayer MoS_2 .

Finally, we present our preliminary *ab initio* spectral functions for bulk and monolayer MoS_2 as a further demonstration of the capabilities of the present methodology, and compare the results with the spectral functions presented in

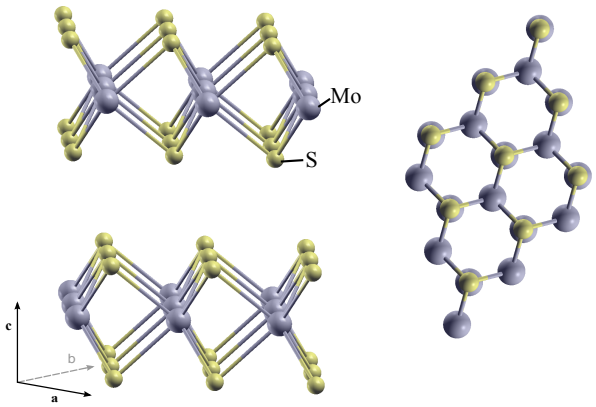


Figure 7.1: Crystal structure of MoS_2 . On the left is the crystal unit cell of bulk MoS_2 repeated three times in the x-y plane. On the right is the crystal unit cell viewed along the c axis showing the hexagonal lattice pattern.

Chapter 6.

1 Structure of MoS_2

The intrinsic two-dimensional nature of the MoS_2 crystal structure has been well-established for a long time. The structure of bulk MoS_2 was originally determined in 1923 by Dickinson and Pauling in Ref. [180]. In Fig. 7.1 we present the bulk trigonal prismatic crystal structure of MoS_2. More precisely we present the 2H confirmation of MoS_2 with space group $P6_3/mmc$. The "layered" nature of the material is immediately apparent.

Single-digit layers of MoS_2 can be obtained via micro-mechanical cleavage or chemical exfoliation as demonstrated in Ref. [160, 162]. The structure of single layered MoS_2 has been examined by crystallographic techniques and scanning tunneling microscopy in Ref. [165]. Single-layer exfoliated crystals of MoS_2 can exist in both a hexagonal semiconducting phase and an octahedral metallic phase. In this chapter we only discuss the semiconducting hexagonal structure in the bulk and monolayer case. In Fig. 7.2 we illustrate the high-symmetry points in the crystal. The in-plane points are Γ, K, M, and the out of plane direction is directed along $\Gamma - A$. A number of the interesting optical and electrical conductivity

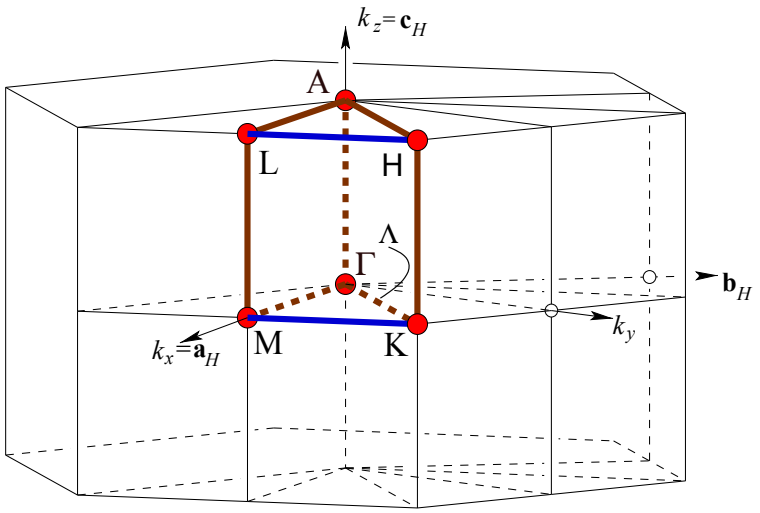


Figure 7.2: Brillouin zone of 2H-MoS_2 with high symmetry points labeled. Figure adapted from Ref. [143].

properties of MoS_2 have been determined along the Γ-K Refs. [164, 167, 168].

For our calculations we have performed geometry relaxations for both the monolayer and the bulk crystal using the Perdew-Zunger parameterization of the exchange correlation functional. The crystal structure is presented in Fig. 7.1. For the bulk crystal $a = 5.97$ bohr and the perpendicular lattice vector $c = 23.22$ bohr. For the monolayer the in-plane lattice vector is unchanged and we include a vacuum region equivalent to the thickness of five monolayers to minimize periodic image interactions. The effect of the vacuum region on the dielectric matrix and the quasiparticle eigenvalues will be discussed in Section 3. For bulk calculations a **k**-point mesh of $6 \times 6 \times 4$ was used, and in the case of the monolayer a **k**-point mesh of $10 \times 10 \times 1$ was used, corresponding to 14 points in the irreducible Brillouin zone. A planewave cutoff of 45 Ry was used for both monolayer and bulk MoS_2.

2 MoS_2 ground state electronic structure

Bulk MoS_2 is an indirect small band gap semiconductor [162]. In the monolayer limit the material becomes a direct gap semiconductor, as demonstrated experi-

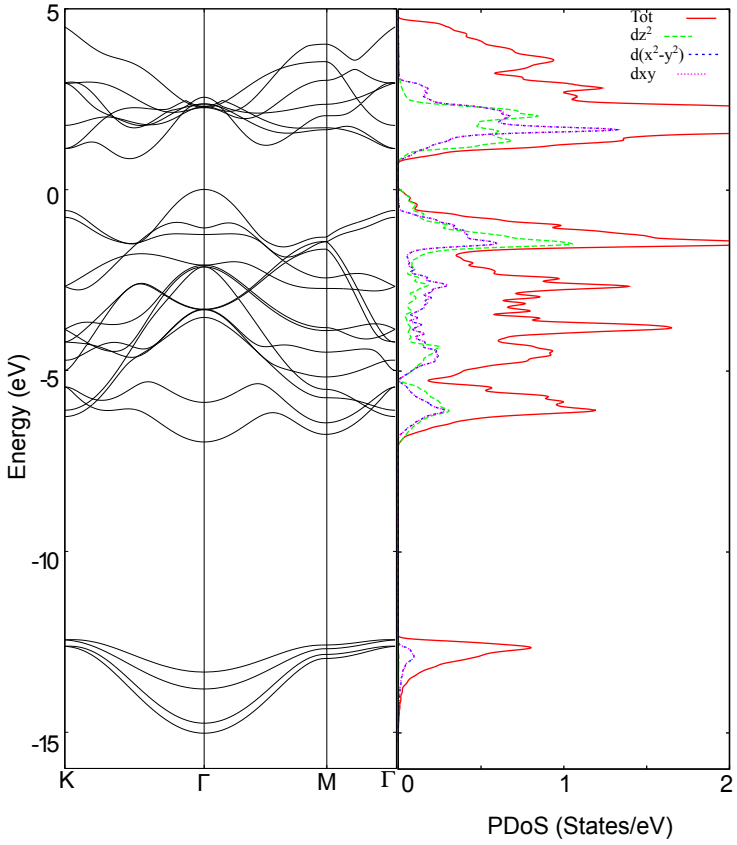


Figure 7.3: Calculated band structure and DOS for bulk MoS_2 . The valence band top has a definite d_{z^2} character and the conduction band bottom has d_{xy} and $d_{x^2-y^2}$ character. The zero of energy is set to the valence band top at the Γ point.

mentally in Ref. [167] and Ref. [168], and calculated using DFT in Ref. [173] and Ref. [174].

2.1 LDA calculations

In Fig. 7.3 and Fig. 7.4 we present the bandstructure and projected density of states (pDOS) for bulk and monolayer MoS_2. Bulk 2H-MoS_2 is an indirect gap semiconductor with the indirect band gap occuring between Γ and halfway along the $\Gamma - K$ line. The valence band top has a Mo-d_{z^2} character and the conduction band bottom has a predominant Mo-$d_{x^2-y^2}$ character.

Hexagonal monolayer MoS_2 is a direct gap semiconductor with the smallest

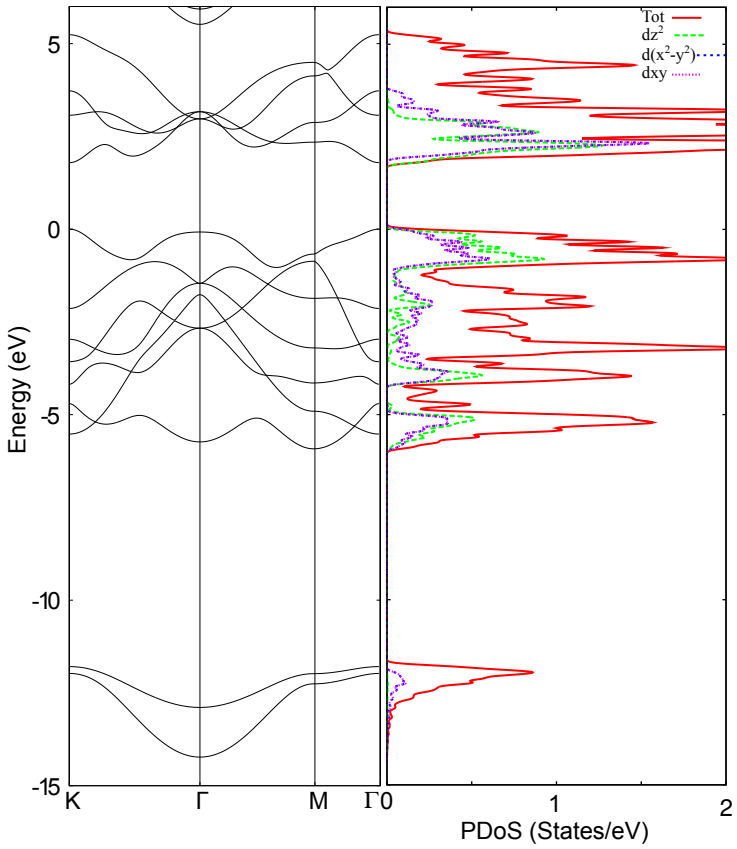


Figure 7.4: Calculated band structure and DOS for monolayer MoS_2 . The zero of the energy axis is set to the valence band top at K.

energy gap at the K point in the Brillouin zone. Again the pDOS suggests that the valence band top has Mo-d_{z^2} character but with a contribution from Mo-$d_{x^2-y^2}$ and d_{xy} character. This is the result of the raising of the d_{xy} and $d_{x^2-y^2}$ bands at the K point.

The calculations presented here are in agreement with previous theoretical work at the LDA level presented in Ref. [173] and Ref. [174]. In the following sections we analyze the difference in electronic screening in bulk and monolayer MoS_2, and discuss the GW calculations for these two systems.

	Present	Ref. [175]	Ref. [181]
2H-MoS_2(perpendicular)	9.86	8.5	7.43
2H-MoS_2(in-plane)	15.63	13.5	15.43
Monolayer MoS_2 (perpendicular)	3.66	2.8	1.63
Monolayer MoS_2 (in-plane)	6.19	4.3	7.36

Table 7.1: Calculated dielectric constants for $\epsilon_M(\mathbf{q}, \omega = 0)$ for bulk and monolayer MoS_2 with $\mathbf{q}$ parallel and perpendicular to the crystal planes.

3 Dielectric properties of MoS_2

Table 7.1 reports the in-plane and perpendicular macroscopic dielectric constants for bulk and monolayer MoS_2 . The macroscopic dielectric function is given by:

$$\epsilon_M(\mathbf{q}, \omega) = [\epsilon^{-1}_{\mathbf{G}=\mathbf{G}'=0}(\mathbf{q}, \omega)]^{-1}. \tag{7.1}$$

The values reported in Table 7.1 for the monolayer dielectric function depend on the size of the vacuum region according to classical electrostatics. In order to rationalize this behaviour and provide values which can be easily compared for different simulation cell sizes in different calculations, we approximate the monolayer as a continuous dielectric and model the slab-vacuum system using classical electrostatics. This treatment yields the following relation for the in-plane dielectric constant which is independent of the vacuum size:

$$\epsilon_{\text{slab}} = \epsilon_{\text{tot}} + (\epsilon_{\text{tot}} - \epsilon_0)\frac{v}{d}, \tag{7.2}$$

where ϵ_{tot} is the macroscopic dielectric constant for the supercell calculated *ab initio*, ϵ_{slab} is the effective dielectric constant of the monolayer, and ϵ_0 is the permittivity of vacuum. The simulation cell has a length c in the z direction the width of the slab given by d, and the vacuum region has a length v, such that $c = v + d$. Using Eq. 7.2 the correction of in-plane screening becomes 14.87. This is of a similar magnitude to the bulk case.

The use of classical electrostatics to discuss the nature of dielectric screening in slab geometries and the convergence of these quantities with respect to vacuum size and **k**-point sampling has been described in more detail in Ref. [69]. These values determined from the classical electrostatic models are insensitive to changes in the vacuum thickness and are better defined quantities.

In order to understand how the dynamical screening changes from bulk to monolayer we examine the behaviour of the head of the dielectric matrix. In all cases here the calculation of the frequency dependent dielectric function is done directly using the Sternheimer method, therefore the contribution from local field effects, the non-local part of the pseudopotential, and the full conduction manifold are included in the calculations. The frequency dependence of the dielectric function is generated using the multishift techniques discussed in Chapter 5.

Fig. 7.5 and Fig. 7.6 illustrate the frequency dependence and dispersion of the electronic response to perturbing potentials of the form $\delta V(\mathbf{q}) = e^{i\mathbf{q}\cdot\mathbf{r}}$. For the bulk material we see a spike in the loss function, $\mathrm{Im}[\epsilon_{00}^{-1}(\mathbf{q},\omega)]$, at 8 eV and another larger peak at 23 eV, respectively. These are the π and $\pi+\sigma$ plasmons and have been discussed for MoS_2 in Refs. [182–184]. The naming convention refers to an effective π valence band arising from the d orbitals of the molybdenum, and a deeper lying σ band arising from hybridized transition metal-chalcogenide orbitals. In Ref. [182] a classical treatment of the plasma resonances is proposed. According to Ref. [182] the two peaks to arise from either the π band with a plasma frequency given by:

$$\omega_{p\pi} = (\frac{4\pi N e^2}{m} n_\pi)^{\frac{1}{2}}, \tag{7.3}$$

or a combined plasmon resonance of the two effective bands π and σ with frequency,

$$\omega_{p\pi+\sigma} = (\frac{4\pi N e^2}{m} n_{(\pi+\sigma)})^{\frac{1}{2}}. \tag{7.4}$$

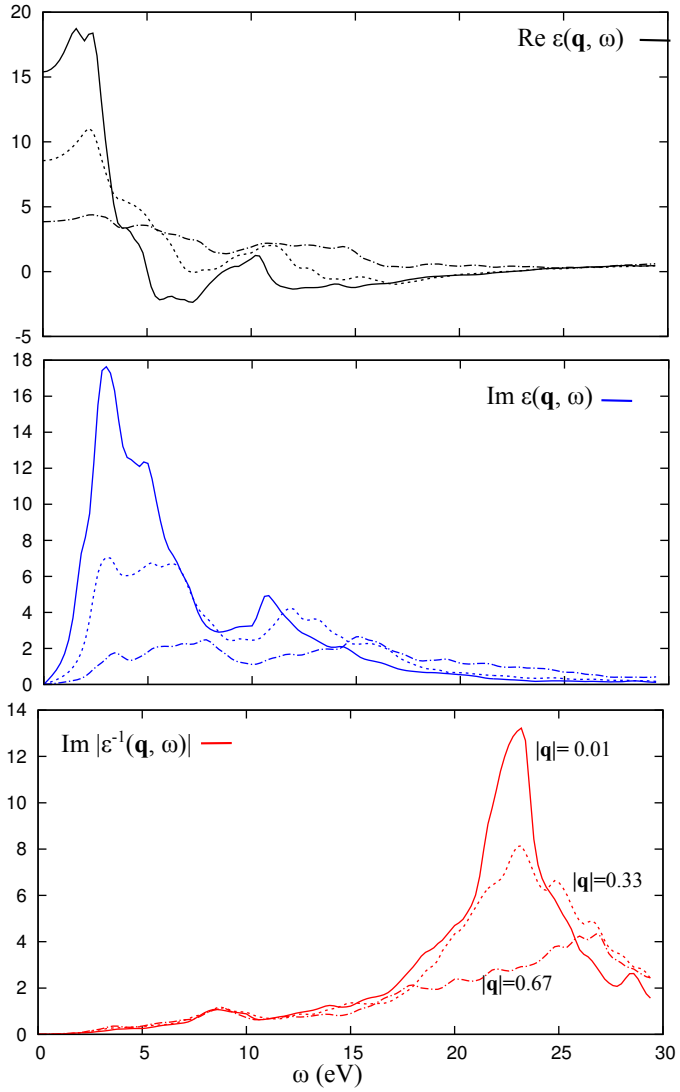


Figure 7.5: The real (black) and imaginary (blue) parts of the head of the dielectric matrix, and the loss function (red) for bulk MoS_2 . The dispersion is along the Γ to K line in the Brillouin zone. The magnitude, $|\mathbf{q}|$, of the inplane wave vector is given in atomic units. The hatching of the lines is consistent between the three panels and denotes the magnitude of the $\mathbf{q}$ vector.

In these expression n_π and n_σ are the number of electrons per atom contributing to each of the two effective bands. In Hartree units, Eq. 7.3 and Eq. 7.4 yield values for the plasmon energy of 12.5 eV and 20.7 eV respectively. Given the simplicity of the classical model the agreement with the *ab initio* plasmon peaks of 7.5 eV and 23 eV can be considered satisfactory.

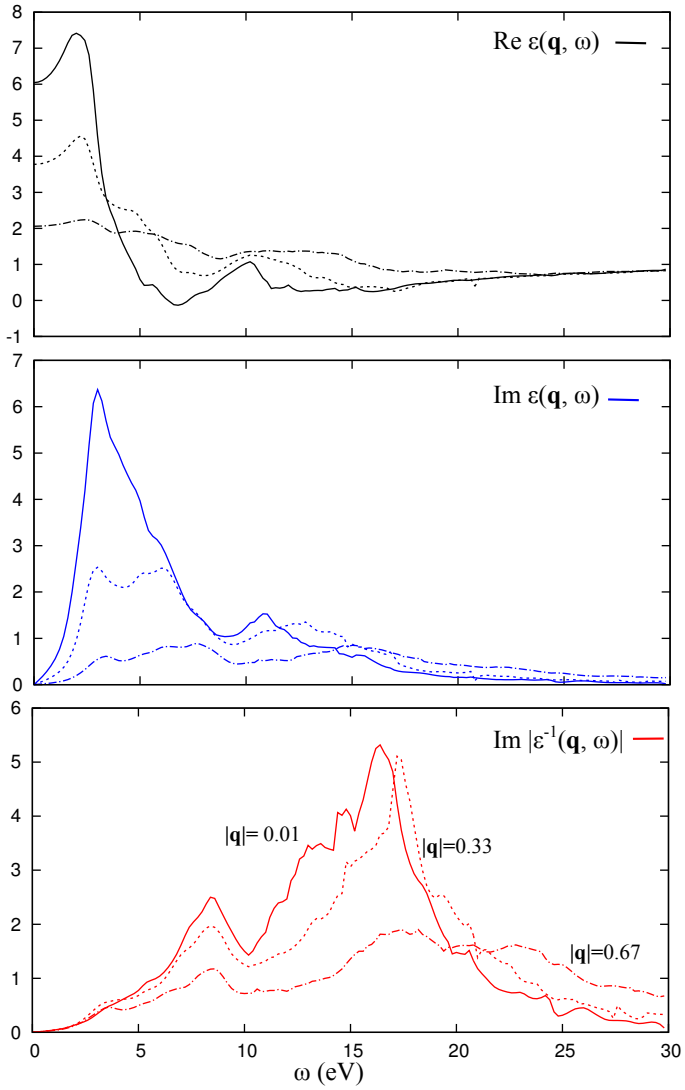


Figure 7.6: The real (black) and imaginary (blue) parts of the head of the dielectric matrix, and the loss function (red) for monolayer MoS_2 . The variation of $\mathbf{q}$ is along the Γ to K line in the Brillouin zone. The hatching of the lines is consistent between panels and denotes the magnitude of the $\mathbf{q}$ vector.

The change in the screening between the bulk and monolayer cases is significant. In Fig. 7.6 we plot the dielectric function and loss function for monolayer MoS_2 . The main loss peak present in the bulk is the $\pi + \sigma$ plasma resonance at 23 eV, whereas the π resonance at 8 eV is relatively suppressed. In the case of the monolayer the π plasmon is more prominent and the $\pi + \sigma$ resonance is

	DFT/LDA		*GW*				
			Present Work		Ref. [177]	Ref. [178]	
	Bulk	Monolayer	Bulk	Monolayer	Monolayer	Bulk	Monolayer
$\Gamma_v \to \Gamma_c$	2.26	3.05	2.80	3.70	4.11	2.69	3.49
$\Gamma \to \Lambda_c$	0.88	2.03	1.73	3.07	3.22	1.22	2.61
$K_v \to K_c$	1.72	1.79	2.95	2.86	2.78	2.23	2.41
$M_v \to M_c$	2.94	2.97	3.39	3.80	4.11	3.77	4.08
E_g	0.85	1.79	1.70	2.86	2.78	1.15	2.41

Table 7.2: Quasiparticle energies corresponding to the band edges of MoS_2. The DFT/LDA and *GW* corrections are reported for the bulk and monolayer. The energies are reported as relative transitions between states. Note the valence band top moves from the Γ point to the K point from the bulk to the monolayer. All values are in units of eV.

red-shifted by 8 eV, so that it appears around 17 eV. The classical treatment of the plasmons in the monolayer does not change the resonant frequency of either of the modes. This suggests that the large change of the $\pi + \sigma$ plasmon must stem from changes in the bandstructure when one goes from the bulk to the monolayer.

In all cases the calculated values for the plasmon energies are in good agreement with the previous calculations reported in Ref. [184] and the experimental data of Ref. [182] for the bulk, and Ref. [162] for monolayer MoS_2. In Sections 4 and 5 we will relate the changes in the static and dynamic parts of the electronic screening to the *GW* quasiparticle eigenvalues and lifetimes.

4 Quasiparticle eigenvalues

In Table 7.2 we present the LDA and quasiparticle eigenvalues for bulk and monolayer MoS_2 for some important electronic transitions in the Brillouin zone. In this section we focus on our calculated values for the G_0W_0 transition energies and compare our values to calculations in the literature. In Fig. 7.7 we highlight some of the key convergence parameters for performing *GW* calculations on the bulk and monolayer dichalcogenide systems. We find a cutoff of at least 10 Ry in necessary to describe the quasiparticle band gap correctly in the bulk and

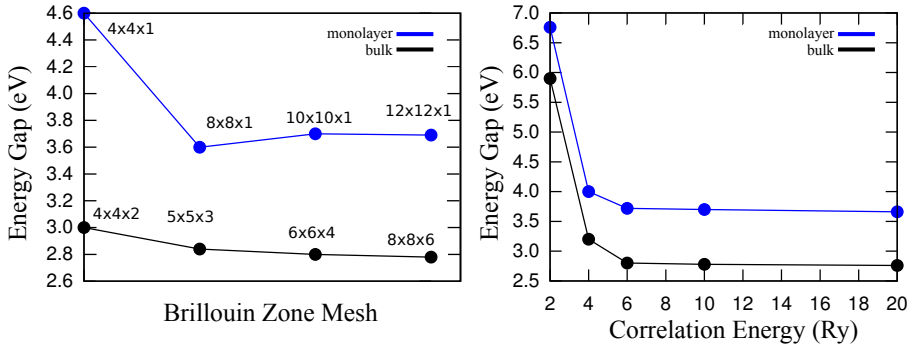


Figure 7.7: The direct gap at Γ for both monolayer and bulk MoS_2. The left panel demonstrates the convergence of the direct gap with respect to the mesh used to describe the Brillouin zone. The right panel demonstrates the convergence of the quasiparticle gap with respect to the planewave cutoff of the correlation energy.

monolayer systems. The convergence with respect to the vacuum in the case of the monolayer is practically immediate given the use of the 2D truncation of the Coulomb interaction.

To get a relative magnitude of the quasiparticle correction appearing in Table 7.2 we can average over the changes in the transition energies at the various points in the Brillouin zone. Doing this we find the bandgap opens by an average of 0.98 eV across the Brillouin zone in the case of bulk MoS_2 and 1.17 eV in the case of the monolayer.

As was mentioned in the introduction to this chapter, there is some discrepancy between the reported band gaps at the G_0W_0 level. In order to obtain a representative picture of the differences between different *GW* calculations we show the energy gaps reported in Table 7.2 in Fig. 7.8. The first potential source of discrepancy is the planewaves cutoff on the dielectric matrix. By eliminating the empty states required for the construction of the dielectric matrix we can directly inspect whether or not we are converged with respect to the **G**-vector cutoff on the dielectric matrix. Fig. 7.9 provide an heuristic demonstration of the convergence of the *GW* calculation with respect to the number of planewaves.

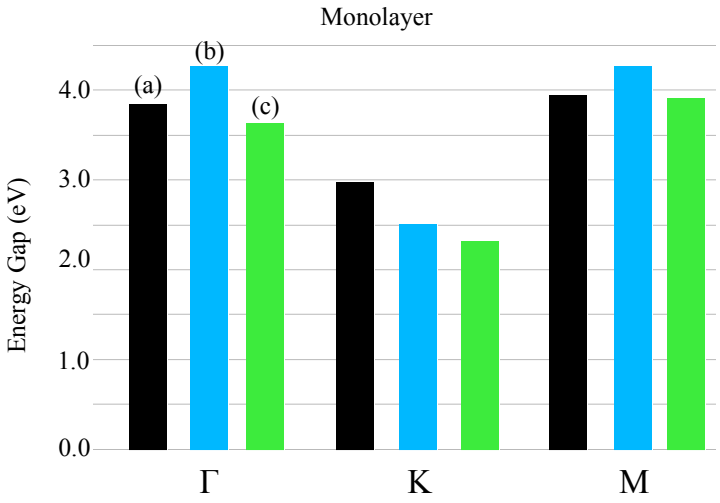


Figure 7.8: Energy gaps at high symmetry points for monolayer MoS_2. The numbers reported are those from (a) the present study, (b) Ref. [177], and (c) Ref. [178]. The largest variation occurs at the Γ point, with differences up to 0.6 eV.

By performing a singular value decomposition one can expect the magnitude of the eigenvectors of the dielectric matrix. By tracking the threshold for the magnitude of the dielectric eigenvalues it is possible to determine at what point the description of the screening has reached a sufficient level of accuracy.

An illustrative example is the direct transition at the M point for the monolayer. Our calculated value is 3.80 eV. In Ref. [177] a careful convergence study is performed and they compute a value of 3.87 eV for the energy of the direct transition at the M point.

The values reported from Ref. [177] in Table 7.2 are calculated at a lower convergence threshold in order to generate the full GW bandstructure at lower computational expense. To attain the fully converged value Ref. [177] needed on the order of 10^4 unoccupied states in the expressions for the polarizability and the Green's function. Even for this large number of states there is still a downward trend in the size of the gap, and our value of 3.80 eV is consistent with their most carefully converged result.

The study of Ref. [177] also notes that reaching this level of convergence

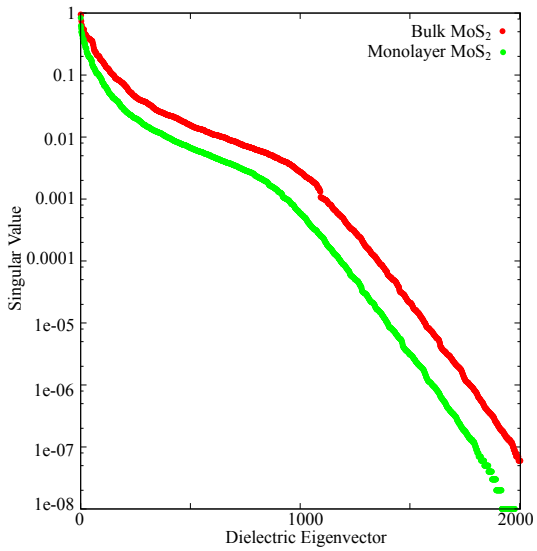


Figure 7.9: Convergence of the dielectric matrix with **G**-vector cutoff . By performing a singular value decomposition of the dielectric matrix we can accurately determine the contributions of higher wave vectors to the dielectric matrix. In terms of energy the 2000th dielectric eigenvector corresponds to a kinetic energy cutoff of 20 Ry

required a number of bands that is two orders of magnitude greater than typical *GW* calculations, see e.g. Refs. [175, 179, 185]. Furthermore the energy cutoff on the dielectric matrix is 4-5 times greater than in Ref. [178] and Ref. [179]. In Ref. [178] 50 planewaves are used to calculate the polarizability corresponding to an energy cutoff of approximately 1 Ryd. Our calculations suggest that at this cutoff the dielectric matrix is only converged to the first decimal place and an increased planewave cutoff is necessary to ensure convergence. As usual this increased planewave cutoff would also necessitate a higher cutoff on the number of conduction states included in the summations for the polarizability.

The magnitude of the energy cutoff for the dielectric matrix is also relevant when considering issues relating to the convergence with **k**-points. If very few **G** vectors are used to describe the dielectric matrix, then the relative importance of the $\epsilon^{-1}_{00}(|\mathbf{q}| = 0)$ entry in the dielectric matrix is correspondingly increased. This may explain why in Ref. [179] they obtain bandgaps for the MoS_2 monolayer

which range from 2.1 eV to 3.5 eV with variation of vacuum spacing and **k**-point grids. In the present study we employ a $10 \times 10 \times 1$, and $12 \times 12 \times 1$ **k**-point grid which is the same as Ref. [177]. Our direct band gap for the monolayer is 2.86 eV, to be compared with the $45 \times 45 \times 1$ **k**-point calculation reported in [179], yielding 2.77 eV.

Our calculations suggest that monolayer MoS_2 is a direct band gap semiconductor, in agreement with the experimental picture Ref. [167] and Ref. [168] and with the calculations in Ref. [177].

A final note on the calculations is the exact exchange contribution, Σ^x, to the self-energy. This quantity is particularly sensitive to the inclusion of the Mo semi-core states $4s^2$ and $4p^6$. To illustrate this effect we can consider the contribution of Σ^x (Eq. 5.35) to the valence band top and conduction band minimum at the Γ point. Without the inclusion of the semi-core states the *GW* correction to the LDA eigenvalues is positive for both valence and conduction states. The inclusion of these semi-core states increases the magnitude of the exact exchange contribution dramatically. For the valence band top in the monolayer the exchange matrix element is -12.56 eV without the semi-core states, and moves to -16.35 eV with the semi-core electrons included in the valence. The changes in the relative quasiparticle energies are much less pronounced due to the uniformity of the change in the exchange matrix elements for the states immediately around the top of the valence band.

In this section we have discussed what we consider to be the salient issues regarding convergence of the quasiparticle energies in MoS_2 . By direct inspection of the dielectric matrix and elimination of unoccupied states in the formalism it is possible to ensure that variation in the values does not stem from truncation of the dielectric matrix or unoccupied states. However more work needs to be done to clarify convergence issues in particular a careful study of not only the the diminishing importance of contributions to the dielectric matrix from higher

planewaves, but also a comparison of variation of the bandgap in the Sternheimer-*GW* approach with planewave cutoff vs. a sum-over-states calculation.

5 Spectral Functions

In this section we present the calculated quasiparticle spectral functions for bulk and monolayer MoS_2. As discussed in Chapter 3, and reproduced here for convenience, the quasiparticle spectral function can be written as:

$$A_{\mathbf{k}}(\omega) = \frac{1}{\pi} \sum_n \frac{|\mathrm{Im}\Sigma_{n\mathbf{k}}(\omega)|}{[\omega - \epsilon_{n\mathbf{k}} - (\mathrm{Re}\Sigma_{n\mathbf{k}}(\omega) - V^{\mathrm{xc}}_{n\mathbf{k}})]^2 + [\mathrm{Im}\Sigma_{n\mathbf{k}}(\omega)]^2} \tag{7.5}$$

The first term in the denominator gives the *GW* correction to the LDA eigenvalue, the second term corresponds to the line broadening in the spectral function.

First we discuss the spectral function of bulk MoS_2. In Fig. 7.10 we present the spectral function as obtained from the LDA bandstructure and a Lorentzian broadening of 200 meV. The broadening was determined by the experimental resolution in the ARPES data presented in Ref. [172]. There are a few distinct changes when going from the LDA bandstructure with experimental broadening to the G_0W_0 spectral function. Our G_0W_0 calculations suggest a large correction to the third valence band creating a separation between the top two bands and the remaining bands in the valence region. Furthermore the second band at the G_0W_0 level is significantly less dispersive than in the LDA calculation.

In Fig. 7.11 we present our calculated spectral functions for monolayer MoS_2 . In case of the monolayer we find that the most significant change between the LDA band structure and the G_0W_0 calculation occurs for the second band from the valence top. This band has a predominant d_{xz} character hybridized with the chalcogen p orbitals. The G_0W_0 correction displays a particularly strong $\mathbf{k}$ dependence, which is not seen in the standard semiconductors and insulators studied in chapter 6. To illustrate this we note that while the magnitude of the self-energy correction at the Γ point is -0.1 eV, at $|\mathbf{k}| = 0.67\text{Å}^{-1}$ the magnitude

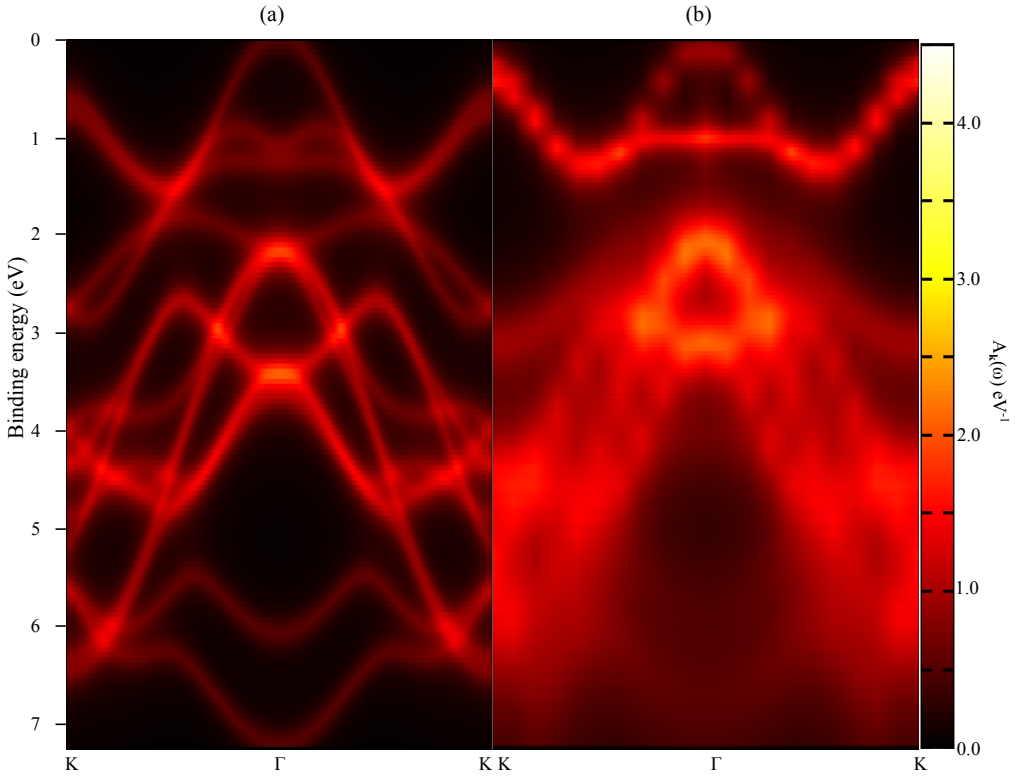


Figure 7.10: (a) The LDA bandstructure for bulk MoS_2 with a lorentzian broadening of 200 meV. (b)*ab initio* G_0W_0 spectral function for bulk MoS_2 .

of the correction rises to -0.86 eV. This has the effect of forcing down the second band from the valence band top as one approaches the K point in the Brillouin zone. As was the case in the bulk material, the G_0W_0 corrections create a more pronounced separation between the valence band top and the remaining valence bands.

We now discuss the behaviour of the imaginary part of the self-energy in the case of bulk and monolayer MoS_2. Again, the intrinsic broadening of 0.3 eV included in the calculation accounts for the finite lifetime of the states at the top of the valence band in Figs. 7.10 and 7.11.

For comparison we highlight the case of silicon discussed in Chapter 6. In silicon the bottom of the valence band is located 12 eV below the valence band top and the self-energy at this point was found to have an imaginary part of

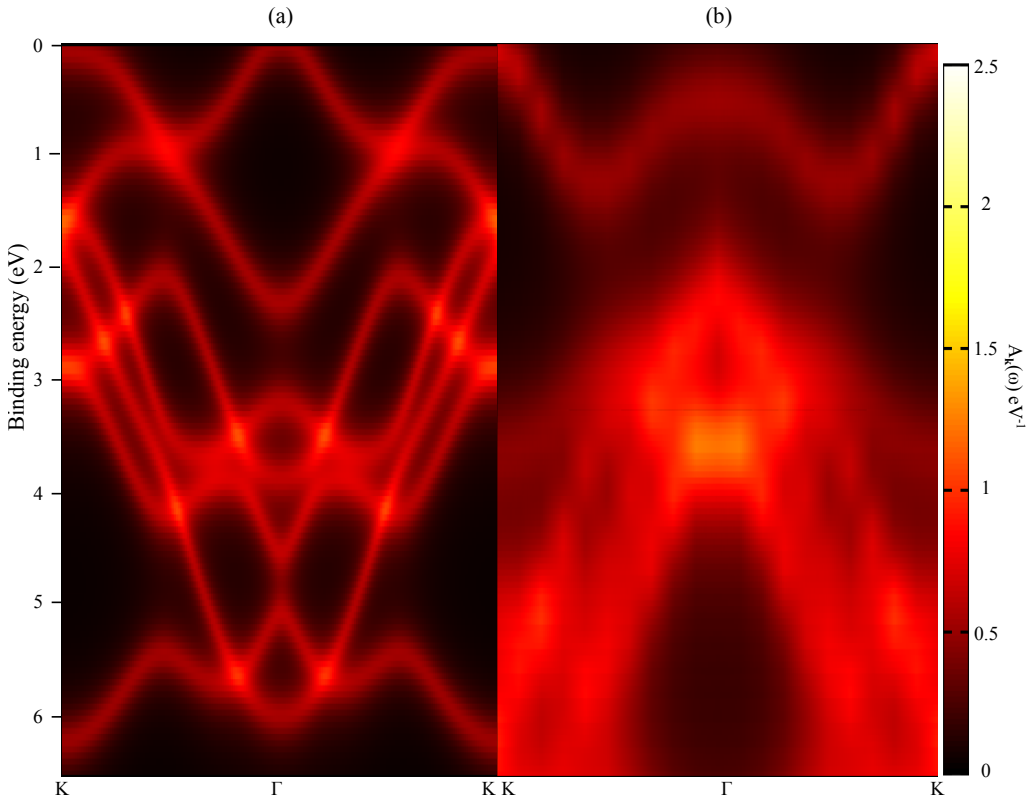


Figure 7.11: (a) The LDA bandstructure for monolayer MoS_2 with a lorentzian broadening of 200 meV. (b) *ab initio* G_0W_0 spectral function for monolayer MoS_2 .

1.3 eV. In line with our discussion of the behaviour of the dielectric function in the previous section we find a large increase in the imaginary part of the self-energy in bulk and monolayer as we approach the energy range of the π plasmon mode at 7 eV. We find for the bottom of the hybridized chalchogen-molybdenum bands in the bulk, located 7.2 eV below the valence band top an imaginary part of 1.08 eV, for the equivalent band in the monolayer we find a value of 1.46 eV. These are of similar magnitude to the imaginary part of the self-energy in silicon as the plasmon threshold is approached.

For reference we report the calculated imaginary part of the self-energy at the Γ point for the second valence band in the monolayer. We find an imaginary part of 0.7 eV. This is qualitatively consistent with the linewidth for this band

in the experimental data presented in Ref. [172].

In this section we have investigated the quasiparticle spectral function of MoS_2. The relative G_0W_0 corrections to different bands in MoS_2 are significantly more dependent on the wavevector than for the systems studied in Chapter 6. In both the monolayer and the bulk this has the effect of separating the valence band top from the remaining bands in the valence. In addition we have found that the changes in the frequency dependence of the dielectric matrix are reflected in the magnitude of the imaginary part of the self-energy, leading to an enhanced broadening in monolayer MoS_2. The increase in magnitude of the imaginary part of the self-energy when passing from the bulk to the monolayer can be tentatively assigned to the redshifting of the $\pi + \sigma$ pole in the case which has the effect of enhancing the imaginary part of the self-energy at lower frequencies.

6 Conclusion

The preliminary work on MoS_2 presented in this chapter has revealed a few interesting points. The variation in reported numbers for the quasiparticle corrections at the *GW* level demonstrates the difficulty of performing fully converged calculations for this material. We have compared our results using the Sternheimer methodology to previous calculations using the sum-over-states approach and found good agreement in cases where a very large number of conduction states are included in the sum-over-states calculations.

We have also performed a careful inspection of the frequency and wavevector dependence of the electronic screening in the bulk and monolayer systems. Here we identified a large shift in the $\pi + \sigma$ plasmon mode move from bulk to monolayer MoS_2. Since the classical plasmon model does not predict such a dramatic change, the effect must stem from some change in the bandstructure of monolayer MoS_2.

Finally we presented our initial results for the quasiparticle spectral function for bulk and monolayer MoS_2 . The G_0W_0 spectral functions were compared to

the experimentally broadened LDA bandstructures with some notable changes in the dispersion and relative positioning of the bands at the G_0W_0 level for both the bulk and monolayer. Future work will focus on generating the GW spectral function across a wider energy range. This will be in order to examine the difference between the single pole plasmon feature discussed in Chapter 6 and the consequences of a more prominent multi-pole structure in the frequency dependence of the dielectric function.

8 Conclusion

In this thesis we have discussed the development of a novel computational approach for performing *GW* calculations. The approach draws from a range of developments in the electronic structure community. The theoretical aspects of the approach are based on Kohn-Sham DFT and the *GW* approximation. The practical and computational aspects are based on the Sternheimer equation and linear response techniques. The overall approach allows for the direct construction of the quantities required in a *GW* calculation.

1 Summary of work to date

The work completed in this thesis is as follows. Building on the initial pilot implementation, which served as a proof of concept, we have implemented the Sternheimer-*GW* method in a fully *ab initio* planewave/pseudopotential framework. What started from an isolated codebase which ran only for the silicon crystal and used an empirical pseudopotential is now capable of treating all the elements in the periodic table with a range of functionals.

In order to achieve the level of numerical stability required for the solution of the Green's function and the screened Coulomb interaction, extensive experimentation with a wide variety of linear system solvers has been performed. Over the course of the work we implemented and tested the following iterative approaches to solving linear systems of equations: the complex bi-conjugate gradient method, the shifted bi-conjugate gradient method, and the generalized minimal residual method. Ultimately it was concluded that the speed and stability of the multi-shift methods gave us the most rapid access to the frequency dependence of the key operators in the *GW* formalism.

We have written routines which exploit crystal symmetry at various stages

of the calculation. This lightens the computational workload of constructing the screened Coulomb interaction and performing convolutions over the Brillouin zone when constructing the self-energy. We have performed initial calculations on standard semiconductors and insulators to demonstrate the validity of the method and obtain detailed spectral functions for these materials. The high resolution of the frequency grid and wave vectors means that we are able to obtain detailed information about quasiparticle lifetimes and collective excitations at the G_0W_0 level.

The initial work performed on MoS_2 has highlighted the difficulty in obtaining numerically converged calculations. This is evident from the spread of reported values in the literature. In particular the number of empty states and the planewaves cutoff used to describe the dielectric matrix are particularly important. Our present calculations suggest at the G_0W_0 level that monolayer MoS_2 is a direct band gap semiconductor and the magnitude of the corrections varies strongly through the Brillouin zone.

Beyond the corrections to the LDA eigenvalues we have presented an initial demonstration of our ability to calculate the full G_0W_0 spectral function for bulk and monolayer MoS_2. Future work will focus on unraveling the effects of plasmon excitations on the quasiparticle lifetimes, and extracting the effective masses in the bulk and monolayer cases.

2 Future work

In this section we discuss a few of the many possibilities for future work. These range from work which is to be undertaken immediately to a few ideas which are more speculative.

The Sternheimer-*GW* approach is more than just an alternative computational strategy for performing *GW* calculations. The Sternheimer-*GW* method is different because the dependence on the starting Hamiltonian is made explicit in the calculation of the Green's function and the screened Coulomb interaction.

For strongly correlated materials the LDA parametrization of the exchange-correlation functional is insufficient. The inclusion of a Hubbard U-parameter, or Hamiltonians with a component of exact exchange has been shown to be important [24, 43, 99]. The Sternheimer-GW approach allows for a straight-forward inclusion of these quantities in the starting Hamiltonian. Experimenting with these modified Hamiltonians could yield insight into the nature of the electronic screening and quasiparticle properties of these correlated materials.

It is also important to make use of all the quantities calculated in the course of a calculation. The direct construction of the frequency-dependent screened Coulomb interaction is a quantity of interest in its own right. For example, the theory of electron-phonon superconductivity requires models for the electronic screening which are often chosen empirically or arbitrarily [186, 187]. It should be possible to use the screened Coulomb interaction calculated in the current approach as input for Migdal-Eliashberg calculations of electron-phonon superconductors.

The wide variety of linear system solvers which were explored in the course of this work reflect the strong connection with the recent progress in linear algebra techniques. Recently there has been a great deal of work in the solution of linear systems of equations and multishift techniques. There are schemes in the literature which allow preconditioning to be applied to multishift techniques. This would improve the applicability of the present method, ensuring for a wider range of systems, rapid convergence of the seed system.

Furthermore, there are extensions to the multishift technique which allow for the simultaneous solution of multiple linear systems of equations with different right-hand sides, see Ref. [188] and references therein. In the present context this would mean solving for multiple right-hand sides of the Sternheimer equation, Eq. 5.28 or the Green's linear system, Eq. 5.32, simultaneously. Exploiting these techniques could lead to a rather dramatic speed up of the overall methodology.

Beyond the development of the computational techniques, the work on the full spectral function has led to an interest in the interplay of plasmons and quasiparticles. In particular 2D systems afford the possibility of varying the plasmon resonances and observing the effect on the quasiparticle eigenvalues and lifetimes. The present calculation should form a solid basis for a broad and systematic study of transition metal dichalcogenides. Unraveling the effect of interlayer interactions on the plasmon modes and quasiparticle lifetimes is work that is presently underway.

Given the present status of the methodology all of the above mentioned work is immediately accessible. A more speculative development of the methodology would involve exploiting the fact that we construct the full self-energy matrix. If a method could be arrived at whereby the self-energy matrix can be reused in the Sternheimer equation, this would provide a route to performing a form of self-consistent GW calculations. Alternatively the self-energy matrix could be used in one shot linear response calculations of other interesting physical quantities. Phonons, magnons, and other physical properties which can be accessed via linear response calculations often cite the limitations of the exchange correlation functional as one of the major reasons for discrepancy with experiment. A scheme where the full G_0W_0 self-energy is used in these calculations could provide improved predictive power and better agreement with experiment.

The development of numerical methods is challenging and the progress can be halting. However, as time passes and the range of the functionality grows, it becomes possible to apply the techniques to more and more interesting physical systems. The initial results reported in this thesis are quite satisfying and will hopefully provide a useful basis for future fruitful investigations into the electronic properties of materials.

A Functional Derivatives

In this appendix we provide a few functional and commutator identities and definitions which are useful in deriving Hedin's equations. These functional relationships are also given in Ref. [33]. The inverse of a generic functional is:

$$\int G(1,3)G^{-1}(3,2)d3 = \delta(1,2). \tag{A.1}$$

Using the product rule, we obtain the following relationship which is useful for defining the inverse of a functional:

$$\frac{\delta G(1,2)}{\delta\phi(3)} = -\int G(1,4)\frac{\delta G^{-1}(4,5)}{\delta\phi(3)}G(5,2)d4d5. \tag{A.2}$$

Similarly we find:

$$\frac{\delta G^{-1}(1,2)}{\delta\phi(3)} = -\int G^{-1}(1,4)\frac{\delta G(4,5)}{\delta\phi(3)}G^{-1}(5,2)d4d5. \tag{A.3}$$

B Rational Interpolation

The rational interpolation using continued fractions algorithm used in this thesis is described in Ref. [133]. A generic function $C_N(z)$ is written as a continued fraction:

$$C_N(z) = \frac{a_1}{1+}\frac{a_2(z-z_1)}{1+}...\frac{a_N(z-z_{N-1})}{1}, \tag{B.1}$$

where z is the argument of the interpolating function at the desired point, z_i are the points the original function is sampled at, and a_i are the coefficients of the interpolating polynomial.

$$C_N(z_i) = u_i, \quad i = 1, ...N. \tag{B.2}$$

the coefficients a_i can be generated from the recursion relations:

$$a_i = g_i(z_i), \quad g_i(z_i) = u_i, \quad i = 1, ..., N. \tag{B.3}$$

$$g_p(z) = \frac{g_{p-1}(z_{p-1}) - g_{p-1}(z)}{(z - z_{p-1})g_{p-1}(z)}, \quad p \geq 2. \tag{B.4}$$

The value of the function can then be generated at the point z using the relations:

$$C_N(z) = \frac{A_N(z)}{B_N(z)}, \tag{B.5}$$

where:

$$\begin{aligned} A_0 = 0, \quad A_1 = a_1, \quad B_0 = B_1 = 1, \\ A_{n+1}(z) = A_n(z) + (z - z_n)a_{n+1}A_{n-1}(z), \\ B_{n+1}(z) = B_n(z) + (z - z_n)a_{n+1}B_{n-1}(z). \end{aligned} \tag{B.6}$$

C Algorithms

In this appendix we provide the algorithms of the various linear system techniques discussed in this thesis. In all cases we will be interested in solving systems of the basic form $\mathbf{Ax} = \mathbf{b}$.

A preconditioning matrix $\mathbf{M}$ is one such that: $\mathbf{M}^{-1}\mathbf{A} \approx \mathbf{I}$ where $\mathbf{I}$ is the identity matrix.

1 cBiCG

Initialize $\mathbf{x}(:) = 0$, the vectors $\mathbf{g}$ are the the residuals $\mathbf{g} = \mathbf{b} - \mathbf{A}\mathbf{x}_n$, i.e. the difference between the solution vector $\mathbf{x}$ after n iterations and the right hand side of the linear system.

for $i = 1$, max_iterations **do**
  if $i = 1$ **then**
    $\mathbf{g}_i = \mathbf{b}, \quad \tilde{\mathbf{g}}_i = \mathbf{g}_i^*, \quad \mathbf{h}_i = \mathbf{M}^{-1}\mathbf{g}_i, \quad \tilde{\mathbf{h}}_i = \mathbf{h}_i^*$
  end if
  $\rho = \sqrt{|\langle \mathbf{g}_i | \mathbf{g}_i \rangle|}$
  if $\rho <$ threshold **then**
    Convergence achieved.
    Exit.
  end if
  $\mathbf{h}_{\text{old}} = \mathbf{h}_i$
  $\tilde{\mathbf{h}}_{\text{old}} = \tilde{\mathbf{h}}_i$ ▷ Apply Hamiltonian to search directions
  $\mathbf{t}_i = \mathbf{A}\mathbf{h}_{\text{old}}$
  $\tilde{\mathbf{t}}_i = (\mathbf{A}^H)\tilde{\mathbf{h}}_{\text{old}}$
  $\alpha = \langle \tilde{\mathbf{g}}_i | \mathbf{M}^{-1}\mathbf{g}_i \rangle / \langle \tilde{\mathbf{h}}_i | \mathbf{t}_i \rangle$
  ▷ Update solution vector
  $\mathbf{x}_{i+1} = \mathbf{x}_i + \alpha \mathbf{h}_i$
  ▷ update residuals
  $\mathbf{g}_{i+1} = \mathbf{g}_i - \alpha \mathbf{t}_i$
  $\tilde{\mathbf{g}}_{i+1} = \tilde{\mathbf{g}}_i - \alpha^* \tilde{\mathbf{t}}_i$
  ▷ Update search directions
  $\beta = -\langle \tilde{\mathbf{t}} | \mathbf{M}^{-1}\mathbf{g}_{i+1} \rangle / \langle \tilde{\mathbf{h}} | \mathbf{t}_i \rangle$
  $\mathbf{h}_{\text{old}} = \mathbf{h}_i$
  $\tilde{\mathbf{h}}_{\text{old}} = \tilde{\mathbf{h}}_i$
  $\mathbf{h}_{i+1} = \mathbf{M}^{-1}\mathbf{g}_{i+1} + \beta \mathbf{h}_{\text{old}}$
  $\tilde{\mathbf{h}}_{i+1} = \mathbf{M}^{-1}\tilde{\mathbf{g}}_{i+1} + \beta^* \tilde{\mathbf{h}}_{\text{old}}$
end for

2 cBiCG Multishift

The multishift algorithm allows us to obtain solutions to the linear system $(\mathbf{A} + \sigma\mathbf{I})\mathbf{x}_\sigma = \mathbf{b}$ These solutions are obtained from the residuals generated in the solution of the seed system where $\sigma = 0$. In practice we split this procedure into

two stages. During the first stage we solve the seed system storing the residual vectors, and the coefficients α and β. These vectors and coefficients are required in the second stage of the algorithm where the recursion relations are used to generate the solution vectors for the shifted systems.

2.1 Solution of seed system

for $i = 1$, max_iterations **do**
  if $i = 1$ **then**
    $\mathcal{K}_i = \mathbf{b}$
    $\mathbf{g}_i = \mathbf{b}$, $\tilde{\mathbf{g}}_i = \mathbf{g}_i^*$, $\mathbf{h}_i = \mathbf{g}_i$, $\tilde{\mathbf{h}}_i = \mathbf{h}_i^*$
  end if
  $\rho = \sqrt{|\langle \mathbf{g}_i | \mathbf{g}_i \rangle|}$
  if $\rho <$ threshold **then**
    Convergence achieved.
    Exit.
  end if
  $\mathbf{t}_i = \mathbf{A}\mathbf{h}_i$
  $\tilde{\mathbf{t}}_i = \mathbf{A}^H \tilde{\mathbf{h}}_i$
  $\alpha = \langle \tilde{\mathbf{g}}_i | \mathbf{g}_i \rangle / \langle \tilde{\mathbf{h}}_i | \mathbf{t}_i \rangle$
  $\mathbf{x}_{i+1} = \mathbf{x}_i + \alpha \mathbf{h}_i$ ▷ Update solution vector
  $\mathbf{g}_{i+1} = \mathbf{g}_i - \alpha \mathbf{t}_i$ ▷ Update residuals
  $\tilde{\mathbf{g}}_{i+1} = \tilde{\mathbf{g}}_i - \alpha^* \tilde{\mathbf{t}}_i$
  $\mathbf{gp} = \mathbf{g}_{i+1}$
  $\tilde{\mathbf{g}}\mathbf{p} = \tilde{\mathbf{g}}_{i+1}$
  $\mathcal{K}_{i+1} = \mathbf{g}_{i+1}$
  $\beta_i = -\langle \tilde{\mathbf{t}}_i | \mathbf{g}_{i+1} \rangle / \langle \tilde{\mathbf{h}} | \mathbf{t}_i \rangle$
  Write (α_i, β_i) to disk. ▷ Update search directions
  $\mathbf{h}_{i+1} = \mathbf{g}_{i+1} + \beta \mathbf{h}_i$
  $\tilde{\mathbf{h}}_{i+1} = \tilde{\mathbf{g}}_{i+1} + \beta^* \tilde{\mathbf{h}}_i$
end for

2.2 Shifted systems

In the second stage we use the recursion relations to generate the solution vectors $\mathbf{x}^\sigma$ for all linear systems of the form $(\mathbf{A} + \sigma\mathbf{I})\mathbf{x}^\sigma = \mathbf{b}$.

for $i = 1$, niters-1 **do**
  Read(α_i, β_i)
  $\alpha = \alpha_i$
  if $i = 1$ **then**
    $\mathbf{u}^\sigma = \mathcal{K}_i$
    $\mathbf{r}^\sigma = \mathcal{K}_i$
    $\alpha_{\text{old}} = \beta_{\text{old}} = \pi^\sigma_{\text{old}} = \pi^\sigma = 1.0$
  end if
  $\pi^\sigma_{\text{new}} = 1.0 - \alpha^\sigma \sigma \pi^\sigma - (\alpha \beta_{\text{old}} / \alpha_{\text{old}})(\pi^\sigma_{\text{old}} - \pi^\sigma)$
  $\alpha^\sigma = (\pi^\sigma / \pi^\sigma_{\text{new}})\alpha$

$\mathbf{x}^\sigma = \mathbf{x}^\sigma + \alpha^\sigma \mathbf{u}^\sigma$
$\mathbf{r} = \mathcal{K}_{i+1}$ ▷ Update the residual and solution vector at each frequency
$\beta^\sigma = (\pi^\sigma / \pi^\sigma_{\text{new}})^2 \beta_i$
$\mathbf{u}^\sigma = (1.0/\pi^\sigma_{\text{new}})\mathbf{r} + \beta^\sigma \mathbf{u}^\sigma$
$\alpha_{\text{old}} = \alpha_i$
$\beta_{\text{old}} = \beta_i$
$\pi^\sigma_{\text{old}} = \pi^\sigma$
$\pi^\sigma = \pi^\sigma_{\text{new}}$
end for

Bibliography

[1] Messiah, A. (1965) *Quantum mechanics*. No. v. 1 in Quantum Mechanics, North-Holland.

[2] Martin, R. M. (2004) *Electronic Structure: Basic Theory and Practical Methods (Vol 1)*. Cambridge University Press.

[3] Damascelli, A. (2004) *Physica Scripta*, **2004**, 61.

[4] Hohenberg, P. and Kohn, W. (1964) *Phys. Rev.*, **136**, B864–B871.

[5] Kohn, W. and Sham, L. J. (1965) *Phys. Rev.*, **140**, A1133–A1138.

[6] Hedin, L. (1965) *Phys. Rev.*, **139**, A796–A823.

[7] Levy, M. (1979) *Proc. Natl. Acad. Sci. U.S.*, **76**, 6062–6065.

[8] Levy, M. (1982) *Phys. Rev. A*, **26**, 1200–1208.

[9] Lieb, E. H. (1983) *International Journal of Quantum Chemistry*, **24**, 243–277.

[10] Ceperley, D. M. and Alder, B. J. (1980) *Phys. Rev. Lett.*, **45**, 566–569.

[11] Vosko, S. H., Wilk, L., and Nusair, M. (1980) *Canadian Journal of Physics*, **58**, 1200–1211.

[12] Perdew, J. P. and Zunger, A. (1981) *Phys. Rev. B*, **23**, 5048–5079.

[13] Perdew, J. P. and Wang, Y. (1992) *Phys. Rev. B*, **45**, 13244–13249.

[14] Becke, A. D. (1988) *Phys. Rev. A*, **38**, 3098–3100.

[15] Perdew, J. P., Burke, K., and Ernzerhof, M. (1996) *Phys. Rev. Lett.*, **77**, 3865–3868.

[16] Becke, A. D. (1993) *The Journal of Chemical Physics*, **98**, 1372–1377.

[17] Becke, A. D. (1993) *The Journal of Chemical Physics*, **98**, 5648–5652.

[18] Sham, L. J. and Kohn, W. (1966) *Phys. Rev.*, **145**, 561–567.

[19] Schwinger, J. (1951) *Proc. Natl. Acad. Sci. U.S.*, **37**, 452.

[20] Sham, L. J. and Schlüter, M. (1983) *Phys. Rev. Lett.*, **51**, 1888–1891.

[21] Perdew, J. P. and Levy, M. (1983) *Phys. Rev. Lett.*, **51**, 1884–1887.

[22] Sham, L. J. and Schlüter, M. (1983) *Phys. Rev. Lett.*, **51**, 1888–1891.

[23] Godby, R. W., Schlüter, M., and Sham, L. J. (1986) *Phys. Rev. Lett.*, **56**, 2415–2418.

[24] Rinke, P., Qteish, A., Neugebauer, J., Freysoldt, C., and Scheffler, M. (2005) *New Journal of Physics*, **7**, 126.

[25] Friedrich, C., Betzinger, M., Schlipf, M., Blgel, S., and Schindlmayr, A. (2012) *Journal of Physics: Condensed Matter*, **24**, 293201.

[26] Gunnarsson, O. and Lundqvist, B. I. (1976) *Phys. Rev. B*, **13**, 4274–4298.

[27] Jones, R. O. and Gunnarsson, O. (1989) *Rev. Mod. Phys.*, **61**, 689–746.

[28] Inkson, J. C. (1986) *Many-body Theory Of Solids, An Introduction*. Plenum Press.

[29] Pratt, G. W. (1963) *Rev. Mod. Phys.*, **35**, 502–505.

[30] Aulbur, W. G., Städele, M., and Görling, A. (2000) *Phys. Rev. B*, **62**, 7121–7132.

[31] Aryasetiawan, F. and Gunnarsson, O. (1998) *Rep. Prog. Phys.*, **61**, 237.

[32] Onida, G., Reining, L., and Rubio, A. (2002) *Rev. Mod. Phys.*, **74**, 601–659.

[33] Strinati, G. (1988) *Rivista Del Nuovo Cimento*, **11**, 1.

[34] Strinati, G., Mattausch, H. J., and Hanke, W. (1982) *Phys. Rev. B*, **25**, 2867–2888.

[35] Hybertsen, M. S. and Louie, S. G. (1985) *Phys. Rev. Lett.*, **55**, 1418–1421.

[36] Hybertsen, M. S. and Louie, S. G. (1986) *Phys. Rev. B*, **34**, 5390–5413.

[37] Falk, D. S. (1960) *Phys. Rev.*, **118**, 105–109.

[38] Adler, S. L. (1962) *Phys. Rev.*, **126**, 413–420.

[39] Wiser, N. (1963) *Phys. Rev.*, **129**, 62–69.

[40] Stankovski, M., Antonius, G., Waroquiers, D., Miglio, A., Dixit, H., Sankaran, K., Giantomassi, M., Gonze, X., Côté, M., and Rignanese, G.-M. (2011) *Phys. Rev. B*, **84**, 241201.

[41] Shih, B.-C., Xue, Y., Zhang, P., Cohen, M. L., and Louie, S. G. (2010) *Phys. Rev. Lett.*, **105**, 146401.

[42] Friedrich, C., Müller, M. C., and Blügel, S. (2011) *Phys. Rev. B*, **83**, 081101.

[43] Patrick, C. E. and Giustino, F. (2012) *J. Phys.: Condens. Mat.*, **24**, 202201.

[44] Tiago, M. L., Ismail-Beigi, S., and Louie, S. G. (2004) *Phys. Rev. B*, **69**, 125212.

[45] Filip, M. R., Patrick, C. E., and Giustino, F. (2013) *Phys. Rev. B*, **87**, 205125.

[46] Godby, R. W. and Needs, R. J. (1989) *Phys. Rev. Lett.*, **62**, 1169–1172.

[47] Bohm, D. and Pines, D. (1953) *Phys. Rev.*, **92**, 609–625.

[48] Overhauser, A. W. (1971) *Phys. Rev. B*, **3**, 1888–1898.

[49] Daling, R., van Haeringen, W., and Farid, B. (1991) *Phys. Rev. B*, **44**, 2952–2960.

[50] Engel, G. E., Farid, B., Nex, C. M. M., and March, N. H. (1991) *Phys. Rev. B*,

44, 13356–13373.

[51] Rojas, H. N., Godby, R. W., and Needs, R. J. (1995) *Phys. Rev. Lett.*, **74**, 1827–1830.

[52] Jin, Y.-G. and Chang, K. J. (1999) *Phys. Rev. B*, **59**, 14841–14844.

[53] Lebègue, S., Arnaud, B., Alouani, M., and Bloechl, P. E. (2003) *Phys. Rev. B*, **67**, 155208.

[54] Giustino, F., Cohen, M. L., and Louie, S. G. (2010) *Phys. Rev. B*, **81**, 115105.

[55] Hamann, D. R., Schlüter, M., and Chiang, C. (1979) *Phys. Rev. Lett.*, **43**, 1494–1497.

[56] Vanderbilt, D. (1990) *Phys. Rev. B*, **41**, 7892–7895.

[57] Blöchl, P. E. (1994) *Phys. Rev. B*, **50**, 17953–17979.

[58] Hamann, D. R., Schlüter, M., and Chiang, C. (1979) *Phys. Rev. Lett.*, **43**, 1494.

[59] Kleinman, L. and Bylander, D. M. (1982) *Phys. Rev. Lett.*, **48**, 1425–1428.

[60] Hedin, L. and Lundqvist, S. (1969) *Solid State Phys.*, **23**, 1–181.

[61] Phillips, J. C. (1961) *Phys. Rev.*, **123**, 420–424.

[62] Shirley, E. L. and Martin, R. M. (1993) *Phys. Rev. B*, **47**, 15404–15412.

[63] Shirley, E. L. and Martin, R. M. (1993) *Phys. Rev. B*, **47**, 15413–15427.

[64] Kotani, T. and van Schilfgaarde, M. (2002) *Solid State Commun.*, **121**, 461 – 465.

[65] Faleev, S. V., van Schilfgaarde, M., and Kotani, T. (2004) *Phys. Rev. Lett.*, **93**, 126406.

[66] Gómez-Abal, R., Li, X., Scheffler, M., and Ambrosch-Draxl, C. (2008) *Phys. Rev. Lett.*, **101**, 106404.

[67] Ismail-Beigi, S. (2006) *Phys. Rev. B*, **73**, 233103.

[68] Spencer, J. and Alavi, A. (2008) *Phys. Rev. B*, **77**, 193110.

[69] Freysoldt, C., Eggert, P., Rinke, P., Schindlmayr, A., Godby, R., and Scheffler, M. (2007) *Computer Physics Communications*, **176**, 1 – 13.

[70] Freysoldt, C., Eggert, P., Rinke, P., Schindlmayr, A., and Scheffler, M. (2008) *Phys. Rev. B*, **77**, 235428.

[71] Bardyszewski, W. and Hedin, L. (1985) *Phys. Scripta*, **32**, 439.

[72] Goldberger, M. L. and Watson, K. M. (2004) *Collision Theory*. Dover Publications.

[73] Almbladh, C. O. and Hedin, L. (1983) *Handbook on Synchrotron Radiation, (ed. E. E. Koch)*, vol. 1b. North-Holland.

[74] Giantomassi, M., Stankovski, M., Shaltaf, R., Grüning, M., Bruneval, F., Rinke, P., and Rignanese, G.-M. (2010) *Phys. Status Solidi B*, **1**, 1.

[75] Shaltaf, R., Rignanese, G.-M., Gonze, X., Giustino, F., and Pasquarello, A. (2008) *Phys. Rev. Lett.*, **100**, 186401.

[76] Park, C.-H., Giustino, F., Spataru, C. D., Cohen, M. L., and Louie, S. G. (2009) *Nano Letters*, **9**, 4234–4239.

[77] Rinke, P., Janotti, A., Scheffler, M., and Van de Walle, C. G. (2009) *Phys. Rev. Lett.*, **102**, 026402.

[78] Rostgaard, C., Jacobsen, K. W., and Thygesen, K. S. (2010) *Phys. Rev. B*, **81**, 085103.

[79] Umari, P., Stenuit, G., and Baroni, S. (2009) *Phys. Rev. B*, **79**, 201104.

[80] Umari, P., Stenuit, G., and Baroni, S. (2010) *Phys. Rev. B*, **81**, 115104.

[81] Gygi, F., Fattebert, J.-L., and Schwegler, E. (2003) *Computer Physics Communications*, **155**, 1 – 6.

[82] Bai, Z., Demmel, J., and Vorst, H. v. d. (1987) *Templates for the Solution of Algebraic Eigenvalue Problems: A Practical Guide*. Society for Industrial and Applied Mathematics, 1 edition edn.

[83] Rocca, D., Gebauer, R., Saad, Y., and Baroni, S. (2008) *The Journal of Chemical Physics*, **128**, –.

[84] Pham, T. A., Nguyen, H.-V., Rocca, D., and Galli, G. (2013) *Phys. Rev. B*, **87**, 155148.

[85] Lu, D., Gygi, F. m. c., and Galli, G. (2008) *Phys. Rev. Lett.*, **100**, 147601.

[86] Wilson, H., Gygi, F., and Galli, G. (2008) *Phys. Rev. B*, **78**, 113303.

[87] Wilson, H. F., Lu, D., Gygi, F., and Galli, G. (2009) *Phys. Rev. B*, **79**, 245106.

[88] Nguyen, H.-V., Pham, T. A., Rocca, D., and Galli, G. (2012) *Phys. Rev. B*, **85**, 081101.

[89] Van Loan, C. F. and Golub, G. H. (1983) *Matrix Computations*. John Hopkins University Press.

[90] Sternheimer, R. M. (1954) *Phys. Rev.*, **96**, 951–968.

[91] Baroni, S., de Gironcoli, S., Dal Corso, A., and Giannozzi, P. (2001) *Rev. Mod. Phys.*, **73**, 515–562.

[92] Bruneval, F. and Gonze, X. (2008) *Phys. Rev. B*, **78**, 085125.

[93] Berger, J. A., Reining, L., and Sottile, F. (2010) *Phys. Rev. B*, **82**, 041103.

[94] Berger, J. A., Reining, L., and Sottile, F. (2012) *Phys. Rev. B*, **85**, 085126.

[95] Berger, J., Reining, L., and Sottile, F. (2012) *The European Physical Journal B*, **85**, 1–10.

[96] Deslippe, J., Samsonidze, G., Jain, M., Cohen, M. L., and Louie, S. G. (2013) *Phys. Rev. B*, **87**, 165124.

[97] Anisimov, V. I., Zaanen, J., and Andersen, O. K. (1991) *Phys. Rev. B*, **44**, 943–954.

[98] Anisimov, V. I., Aryasetiawan, F., and Lichtenstein, A. I. (1997) *Journal of Physics: Condensed Matter*, **9**, 767.

[99] Jiang, H., Gomez-Abal, R. I., Rinke, P., and Scheffler, M. (2010) *Phys. Rev. B*, **82**, 045108.

[100] Stan, A., Dahlen, N. E., and Leeuwen, R. v. (2009) *The Journal of Chemical Physics*, **130**, 114105.

[101] van Schilfgaarde, M., Kotani, T., and Faleev, S. (2006) *Phys. Rev. Lett.*, **96**, 226402.

[102] Svane, A., Christensen, N. E., Gorczyca, I., van Schilfgaarde, M., Chantis, A. N., and Kotani, T. (2010) *Phys. Rev. B*, **82**, 115102.

[103] Faleev, S. V., Mryasov, O. N., and van Schilfgaarde, M. (2012) *Phys. Rev. B*, **85**, 174433.

[104] Tomczak, J. M., van Schilfgaarde, M., and Kotliar, G. (2012) *Phys. Rev. Lett.*, **109**, 237010.

[105] Schöne, W.-D. and Eguiluz, A. G. (1998) *Phys. Rev. Lett.*, **81**, 1662–1665.

[106] Friedrich, C., Schindlmayr, A., Blügel, S., and Kotani, T. (2006) *Phys. Rev. B*, **74**, 045104.

[107] Caruso, F., Rinke, P., Ren, X., Scheffler, M., and Rubio, A. (2012) *Phys. Rev. B*, **86**, 081102.

[108] Caruso, F., Rinke, P., Ren, X., Rubio, A., and Scheffler, M. (2013) *Phys. Rev. B*, **88**, 075105.

[109] Cohen, M. L. and Bergstresser, T. K. (1966) *Phys. Rev.*, **141**, 789–796.

[110] Giannozzi, P., et al. (2009) *Journal of Physics: Condensed Matter*, **21**, 395502.

[111] Baroni, S., Giannozzi, P., and Testa, A. (1987) *Phys. Rev. Lett.*, **58**, 1861–1864.

[112] Pickard, C. J. and Mauri, F. (2001) *Phys. Rev. B*, **63**, 245101.

[113] Joyce, S. A., Yates, J. R., Pickard, C. J., and Mauri, F. (2007) *The Journal of Chemical Physics*, **127**, 204107.

[114] Reining, L., Onida, G., and Godby, R. W. (1997) *Phys. Rev. B*, **56**, R4301–R4304.

[115] Kunc, K. and Tosatti, E. (1984) *Phys. Rev. B*, **29**, 7045–7047.

[116] Hybertsen, M. S. and Louie, S. G. (1987) *Phys. Rev. B*, **35**, 5585–5601.

[117] Pick, R. M., Cohen, M. H., and Martin, R. M. (1970) *Phys. Rev. B*, **1**, 910–920.

[118] Martin-Samos, L. and Bussi, G. (2009) *Comput. Phys. Commun.*, **180**, 1416 – 1425.

[119] Del Sole, R., Reining, L., and Godby, R. W. (1994) *Phys. Rev. B*, **49**, 8024–8028.

[120] Johnson, D. D. (1988) *Phys. Rev. B*, **38**, 12807–12813.

[121] Ho, K.-M., Ihm, J., and Joannopoulos, J. D. (1982) *Phys. Rev. B*, **25**, 4260–4262.

[122] Hübener, H., Pérez-Osorio, M. A., Ordejón, P., and Giustino, F. (2012) *Phys. Rev. B*, **85**, 245125.

[123] Hübener, H., Pérez-Osorio, M., Ordejón, P., and Giustino, F. (2012) *Eur. Phys. J. B*, **85**, 1–10.

[124] Frommer, A. (2003) *Computing*, **70**, 87–109.

[125] Arnaud, B. and Alouani, M. (2000) *Phys. Rev. B*, **62**, 4464–4476.

[126] Maradudin, A. A. and Vosko, S. H. (1968) *Rev. Mod. Phys.*, **40**, 1–37.

[127] Jacobs, D. A. H. (1986) *IMA J. Numer. Anal.*, **6**, 447–452.

[128] van der Vorst, H. (1992) *SIAM J. Sci. Stat. Comp.*, **13**, 631–644.

[129] Jegerlehner, B. (1996) *arXiv preprint hep-lat/9612014*.

[130] Ahmad, M. I., Szyld, D. B., and van Gijzen, M. B. (2012) Preconditioned multishift bicg for $\langle_2$-optimal model reduction. Tech. Rep. 12-06-15, Department of Mathematics, Temple University, revised March 2013.

[131] Sleijpen, G. L. G. and Fokkema, D. R. (1993) *Electron. Trans. Numer. Anal.*, **1**, 11–32.

[132] Teter, M. P., Payne, M. C., and Allan, D. C. (1989) *Phys. Rev. B*, **40**, 12255–12263.

[133] Vidberg, H. J. and Serene, J. W. (1977) *J. Low Temp. Phys.*, **29**, 179–192.

[134] Hübener, H. and Giustino, F. (2014) *Phys. Rev. B*, **89**, 085129.

[135] Lambert, H. and Giustino, F. (2013) *Phys. Rev. B*, **88**, 075117.

[136] Mahan, G. D. (1980) *Phys. Rev. A*, **22**, 1780–1785.

[137] Troullier, N. and Martins, J. L. (1991) *Phys. Rev. B*, **43**, 1993–2006.

[138] Andrade, X., Botti, S., Marques, M. A. L., and Rubio, A. (2007) *The Journal of Chemical Physics*, **126**, 184106.

[139] Dixon, D. A. and Matsuzawa, N. (1994) *The Journal of Physical Chemistry*, **98**, 3967–3977.

[140] van Gisbergen, S. J. A., Kootstra, F., Schipper, P. R. T., Gritsenko, O. V., Snijders, J. G., and Baerends, E. J. (1998) *Phys. Rev. A*, **57**, 2556–2571.

[141] Monkhorst, H. J. and Pack, J. D. (1976) *Phys. Rev. B*, **13**, 5188–5192.

[142] Hybertsen, M. S. and Louie, S. G. (1986) *Phys. Rev. B*, **34**, 5390–5413.

[143] Aroyo, M., Perez-Mato, J., Orobengoa, D., Tasci, E., De La Flor, G., and Kirov, A. (2011) *Bulgarian Chemical Communications*, **43**, 183–197.

[144] Hellwege, K. H. and Madelung, O. (eds.) (1982) *Numerical Data and Functional Relationships in Science and Technology, Landolt-Börnstein, New Series, Group III*, vol. Vol. 17, pt. A and Vol. 22, pt. A. Springer, Berlin.

[145] Ortega, J. E. and Himpsel, F. J. (1993) *Phys. Rev. B*, **47**, 2130–2137.

[146] Wachs, A. L., Miller, T., Hsieh, T. C., Shapiro, A. P., and Chiang, T.-C. (1985) *Phys. Rev. B*, **32**, 2326–2333.

[147] Shishkin, M. and Kresse, G. (2006) *Phys. Rev. B*, **74**, 035101.

[148] Himpsel, F. J., van der Veen, J. F., and Eastman, D. E. (1980) *Phys. Rev. B*, **22**, 1967–1971.

[149] Lambrecht, W. R. L., Segall, B., Yoganathan, M., Suttrop, W., Devaty, R. P., Choyke, W. J., Edmond, J. A., Powell, J. A., and Alouani, M. (1994) *Phys. Rev. B*, **50**, 10722–10726.

[150] Baldini, G. and Bosacchi, B. (1970) *Phys. Status Solidi B*, **38**, 325–334.

[151] Arnaud, B., Lebègue, S., and Alouani, M. (2005) *Phys. Rev. B*, **71**, 035308.

[152] Yokoya, T., et al. (2006) *Sci. Tech. Adv. Mater.*, **7**, Supplement 1, S12.

[153] Lundqvist, B. (1967) *Phys. Kond. Mater.*, **6**, 193–205.

[154] Langreth, D. C. (1970) *Phys. Rev. B*, **1**, 471–477.

[155] Blomberg, C. and Bergersen, B. (1972) *Canadian Journal of Physics*, **50**, 2286–2293.

[156] Guzzo, M., Lani, G., Sottile, F., Romaniello, P., Gatti, M., Kas, J. J., Rehr, J. J., Silly, M. G., Sirotti, F., and Reining, L. (2011) *Phys. Rev. Lett.*, **107**, 166401.

[157] Lischner, J., Vigil-Fowler, D., and Louie, S. G. (2013) *Phys. Rev. Lett.*, **110**, 146801.

[158] Godby, R. W., Schlüter, M., and Sham, L. J. (1987) *Phys. Rev. B*, **36**, 6497–6500.

[159] Lischner, J., Bazhirov, T., MacDonald, A. H., Cohen, M. L., and Louie, S. G. (2014) *Phys. Rev. B*, **89**, 081108.

[160] Novoselov, K. S., Jiang, D., Schedin, F., Booth, T. J., Khotkevich, V. V., Morozov, S. V., and Geim, A. K. (2005) *PNAS*, **102**, 10451–10453.

[161] Geim, A. K. and Novoselov, K. S. (2007) *Nat Mater*, **6**, 183–191.

[162] Coleman, J. M., Rebecca, J. N., and Nicolosi, V. (2011) *Science*, **331**, 568–571.

[163] Geim, A. K. and Grigorieva, I. V. (2013) *Nature*, **499**, 419–425.

[164] Radisavljevic, B., Radenovic, A., Brivio, J., Giacometti, V., and Kis, A. (2011) *Nature Nanotechnology*, **6**, 147–150.

[165] Eda, G., Fujita, T., Yamaguchi, H., Voiry, D., Chen, M., and Chhowalla, M. (2012) *ACS Nano*, **6**, 7311–7317.

[166] Chhowalla, M., Suk Shin, H., Eda, G., Lain-Jong, L. L., Ping Loh, L., and Zhang, H. (2013) *Nat Chem*, **5**, 263–275.

[167] Lee, C., Yan, H., Brus, L. E., Heinz, T. F., Hone, J., and Ryu, S. (2010) *ACS Nano*, **4**, 2695–2700.

[168] Splendiani, A., Sun, L., Zhang, Y., Li, T., Kim, J., Chim, C.-Y., Galli, G., and Wang, F. (2010) *Nano Letters*, **10**, 1271–1275.

[169] Wang, Q. H., Kalantar-Zadeh, K., Kis, A., Coleman, J. N., and Strano, M. S. (2012) *Nature Nanotechnology*, **7**, 699–712.

[170] Crowne, F. J., Amani, M., Birdwell, A. G., Chin, M. L., O'Regan, T. P., Najmaei, S., Liu, Z., Ajayan, P. M., Lou, J., and Dubey, M. (2013) *Phys. Rev. B*, **88**, 235302.

[171] Jin, W., et al. (2013) *Phys. Rev. Lett.*, **111**, 106801.

[172] Alidoust, N., et al. (2013) *arXiv:1312.7631 [cond-mat]*.

[173] Li, T. and Galli, G. (2007) *The Journal of Physical Chemistry C*, **111**, 16192–16196.

[174] Lebègue, S. and Eriksson, O. (2009) *Phys. Rev. B*, **79**, 115409.

[175] Cheiwchanchamnangij, T. and Lambrecht, W. R. L. (2012) *Phys. Rev. B*, **85**, 205302.

[176] Feng, J., Qian, X., Huang, C.-W., and Li, J. (2012) *Nature Photonics*, **6**, 866–872.

[177] Qiu, D. Y., da Jornada, F. H., and Louie, S. G. (2013) *Phys. Rev. Lett.*, **111**, 216805.

[178] Molina-Sánchez, A., Sangalli, D., Hummer, K., Marini, A., and Wirtz, L. (2013) *Phys. Rev. B*, **88**, 045412.

[179] Hüser, F., Olsen, T., and Thygesen, K. S. (2013) *Phys. Rev. B*, **88**, 245309.

[180] Dickinson, R. G. and Pauling, L. (1923) *Journal of the American Chemical Society*, **45**, 1466–1471.

[181] Molina-Sánchez, A. and Wirtz, L. (2011) *Phys. Rev. B*, **84**, 155413.

[182] Liang, W. Y. and Cundy, S. L. (1969) *Philosophical Magazine*, **19**, 1031–1043.

[183] Zeppenfeld, K. (1970) *Optics Communications*, **1**, 377 – 378.

[184] Johari, P. and Shenoy, V. B. (2011) *ACS Nano*, **5**, 5903–5908.

[185] Ramasubramaniam, A. (2012) *Phys. Rev. B*, **86**, 115409.

[186] Lee, K.-H., Chang, K. J., and Cohen, M. L. (1995) *Phys. Rev. B*, **52**, 1425–1428.

[187] Margine, E. R. and Giustino, F. (2013) *Phys. Rev. B*, **87**, 024505.

[188] Birk, S. and Frommer, A. (2013) *Numerical Algorithms*, pp. 1–23.

Acknowledgements

My first thanks go to my supervisor Feliciano Giustino for initiating the project, providing valuable guidance along the way, and demonstrating a remarkable level of patience with my erratic progress.

A thank you also to my colleagues in the MML for having provided a stimulating working environment. In particular I would like to thank my contemporaries here: Chris, Harry, Keian, Marina, Miguel, and Tim. I have enjoyed the conversations about electronic structure, the games of "Only Connect", and the occasional ill-advised foray into algorithmic gambling. I'd also like to thank our friendly post-doc Hannes in the neighbouring bell tower, who managed to find some time from his own busy schedule of research and pasta-making to provide me with holistic guidance.

I'd like to thank the members of the Wolfson College Bike Workshop and its extended family for a number of diverting Tuesday evenings, trips to Wales and Cornwall, balloon watching, crosswords, and the odd pint of Guinness.

A large thank you to Michele, who has been there right from the start when I went crazy in the park, and who took the long boat ride to England with me.

Studying and living here in Oxford has been an enormous privilege, and for this opportunity my final thanks go to my Mum, Dad, and Sister, who have supported me through everything I have ever done.

Papers and Presentations

Publications

[1] H. Lambert, F. Giustino, *Ab initio Sternheimer-GW method for quasiparticle calculations using plane waves*, Phys. Rev. B **81**, 075117 (2013).

[2] H. Lambert, F. Giustino, *Quasiparticle Excitations in MoS_2*, Manuscript in preparation.

Conference Presentations

[1] *Ab initio Sternheimer-GW method for quasiparticle calculations*, American Physical Society (APS) March Meeting, March 2014, Denver, CO.

[2] *Ab initio Sternheimer-GW with planewaves*, Trends in GW-approaches for Nano-Sciences in Europe, July 2013, Karlsruhe, Germany.

[3] *Poster: using the Sternheimer-GW method for quasiparticle calculations*, 16th International Workshop on Computational Physics and Material Science: Total Energy and Force Methods, January 2013, Trieste, Italy.